

Energy Efficiency and Flexibility Analysis for Building-Integrated Photovoltaics-Heat Pump
Combinations in a House

Erin Gaucher-Loksts

A Thesis
In the Department
of
Building, Civil and Environmental Engineering

Presented in Partial Fulfillment of the Requirements
For the Degree of Master of Applied Science (Building Engineering) at Concordia University
Montreal, Quebec, Canada

February 2022

©Erin Gaucher-Loksts, 2022

CONCORDIA UNIVERSITY
School of Graduate Studies

This is to certify that the thesis prepared

By: Erin Gaucher-Loksts

Entitled: Energy Efficiency and Flexibility Analysis for Building-Integrated Photovoltaics-Heat Pump Combinations in a House

and submitted in partial fulfillment of the requirements for the degree of

Master of Applied Science (Building Engineering)

complies with the regulations of the University and meets the accepted standards with respect to originality and quality.

Signed by the final Examining Committee:

_____	Chair
<i>Dr. Hua Ge</i>	
_____	Examiner
<i>Dr. Hua Ge</i>	
_____	Examiner
<i>Dr. Bruno Lee</i>	
_____	Co-Supervisor
<i>Dr. Andreas Athienitis</i>	
_____	Co-Supervisor
<i>Dr. Mohamed Ouf</i>	

Approved by:

Dr. Mazdak Nik-Bakht, Graduate Program Director
Department of Building, Civil and Environmental Engineering

March 15, 2022

Dr. Mourad Debbabi, Dean
Gina Cody School of Engineering and Computer Science

Energy Efficiency and Flexibility Analysis for Building-Integrated Photovoltaics- Heat Pump Combinations in a House

Erin Gaucher-Loksts

Abstract

This thesis considers three design configurations of air source heat pumps and building-integrated photovoltaic (BIPV) systems in a solar house concerning energy efficiency and energy flexibility in interacting with a smart grid. BIPV/Thermal (BIPV/T) provides electricity generation and reduces the electricity consumption when pre-heating air for a heating, ventilation, and air conditioning (HVAC) system such as a heat pump. A heat pump's coefficient of performance (COP) and capacity decrease at colder temperatures. Therefore, increasing the inlet temperature can significantly increase the capacity or enable a heat pump to operate when the outdoor air is below the cut-off temperature. A higher COP enables an efficient heat transfer and storage when heat is available; this provides flexibility to the system. Energy flexibility is an important factor to consider as providing flexibility to the grid helps alleviate its demand and stress during critical periods. In addition to the grid's need, the utility often provides incentives for consumers to reduce electricity consumption during critical periods. Adopting advanced controls that can provide flexibility is beneficial to help reduce overall electricity consumption and energy cost.

A comprehensive literature review of various BIPV systems and their applications demonstrated a gap in the current research to investigate the possibility of utilizing solar gain (from inside a solarium or greenhouse) to pre-heating air for a heat pump. Furthermore, the use of semi-transparent photovoltaic (STPV) windows with a heat pump have not been explored. Thus, a new configuration is proposed utilizing the solar heated air in an attached solarium as a source for the air side of an air-source heat pump water heater (HPWH) with integrated water thermal storage and a 5kW semi-transparent photovoltaic façade. This configuration is compared with two other

cases: a reference case consists of a 5kW BIPV system on the roof with a separate HPWH and a more novel option of a 5kW BIPV/T roof system. The heated air from the BIPV/T system is ducted to the air source of the HPWH, which also contains integrated thermal storage (the hot water). The three cases are modelled with an explicit finite difference thermal network model, and energy performance is determined and compared over a typical heating season in Montreal.

Another important gap in the research found from the literature review is maximizing the flexibility of BIPV/T and heat pump systems. Thus, the energy flexibility of the BIPV/T configurations listed previously is compared for different scenarios, such as heating the thermal water storage during the daytime (e.g., using the solar heat in the novel options) and using it for space heating during the time that the grid is under stress (and may have price incentives).

A full-scale experimental set-up modelling the passive solar case was completed to demonstrate this novel system configuration and to partially verify the developed model using the Future Buildings Laboratory at Concordia University. The real-time data collected from the experiment is analyzed and utilized to verify each component within the system. Results show that the proposed case utilizing the solarium air as the inlet of the heat pump had over 80% reduction in annual electricity consumption relative to the reference. In comparison, the BIPV/T configuration had around a 5% reduction compared to the reference case. The proposed configuration improves system performance significantly compared to the reference and ducted BIPV/T systems. The tank volume and solarium size had the highest impact on the system's energy flexibility. Optimal thermal storage size was between 300 – 600 L for a house with a floor area of 116 m². The experimental results confirmed the increased energy savings from the passive solar configuration operation. The temperature in the test rooms reached over 20 °C on a cold sunny day from passive solar gains. The simulation models had a similar performance to the experimental data which also demonstrated the significant energy flexibility potential of the configuration tested.

Acknowledgement

I would like to first thank my family and friends for their support throughout this journey. Their support helped me to continue through this journey for all challenges and successes throughout the years.

I would like to thank both of my supervisors, Dr. Andreas Athienitis and Dr. Mohamed Ouf for their encouragement and guidance along the way.

I would like to acknowledge the technical and financial support from the NSERC/Hydro Quebec Research Chair and the Faculty of Engineering and Computer Science of Concordia University.

During these past years, I have met with amazing people in CZEBS and on campus that I admire and look up to. I would like to thank Jiwu Rao, Anna-Maria Sigounis, David Sun, Sam Yip, Stratos Rounis, Ali Saberi, Vasken Dermardiros, Harry Vallianos, Fatima Amar, Emil Jalilov, Lyne Dee, Matin Abtahi, and Navid Morovat for having contributed one way or another to this amazing life experience.

Thank you to Dr. Hua Ge and Jiwu Rao for their help and support with the experimental setup and construction in the Future Buildings Laboratory.

Finally, I would like to thank the amazing people at CanmetENERGY – Varennes for their continued encouragement and support. A special thank you to Véronique Delisle, Benjamin Roy, Justin Tamasauskas, and Costa Kapsis.

Contents

List of Figures	viii
List of Tables	xi
Nomenclature	xii
Chapter 1. Introduction.....	1
1.1 Objectives.....	2
1.2 Thesis Overview.....	4
Chapter 2. Literature Review.....	5
2.1 Introduction	5
2.2 BIPV/T Systems.....	5
2.2.1 Air-Based BIPV/T Systems	9
2.2.2 BIPV/T Design Parameters.....	10
2.2.3 BIPV/T Applications	12
2.3 STPV Systems.....	17
2.3.1 STPV Design Considerations	18
2.3.2 STPV Applications	22
2.4 Smart Heat Pump Systems and Grid Flexibility	27
2.4.1 Smart Grid and Energy flexibility.....	27
2.4.2 Demand Response.....	28
2.4.3 Smart Heat Pumps.....	30
2.4.4 Storage Sizing	31
2.5 Research Gaps	33
Chapter 3. System Modelling and Experimental Setup.....	35
3.1 Simulation Methodology.....	35
3.1.1 Model Description	37
3.1.2 Analysis Approach.....	45
3.2 Results	51
3.2.1 Heating Season Electricity Consumption	51

3.2.2	Flexibility Characterization	54
Chapter 4.	Demonstration and Experimental Verification	59
4.1	Objectives.....	59
4.2	Experimental Setup	60
4.2.1	Equipment.....	61
4.2.2	Test Rooms	62
4.2.3	Measurement Instruments.....	62
4.2.4	Sensor Positioning	63
4.3	Results and Comparison.....	66
4.3.1	Experimental Results	66
4.3.2	Verification	69
4.4	Conclusions	71
Chapter 5.	Summary and Conclusions	73
5.1	Contributions.....	74
5.2	Future Work	75
Chapter 6.	References.....	76
Appendix A:	Programming Code.....	86
Appendix B:	Example Parametric Analysis Output.....	126
Appendix C:	Additional Calculations Used and Verification.....	131
Appendix D:	Additional Experimental Results.....	147

List of Figures

Figure 1.1: Typical demand Quebec demand profile outlining critical peak events for Hydro-Quebec	2
Figure 1.2: Schematic illustrating the main configuration studied (STPV-HPWH)	4
Figure 2.1: Categorization of flat plate BIPV/T systems (Yang T. , 2015).....	6
Figure 2.2: Open-loop (left) and closed loop (right) configurations (Candanedo, Athienits, Candanedo, O'Brien, & Chen, 2010)	7
Figure 2.3: Schematic of a solar domestic hot water system (Ghorab, Entchev, & Yang, 2017) ..	8
Figure 2.4: Schematic of a PVT integrated heat pump (Tyagi, Kaushik, & Tyagi, 2012).....	9
Figure 2.5: Different configurations of PVT modules (Zhang, Zhao, Smith, Xu, & Yu, 2012) ..	10
Figure 2.6: Variation of thermal and electrical efficiency with respect to the duct depth (Adeli, Sobhnamayan, Farahat, Alavi, & Sarhaddi, 2012)	11
Figure 2.7: Schematic of BIPV/T applications studied (i) Pre-heating fresh air (ii) DHW heating with an air-to-water heat exchanger (iii) Air-to-water heat pump for DHW and space heating (iv) DHW with a heat pump water heater (Delisle & Kummert, 2016)	14
Figure 2.8: Schematic of (i) Wall integrated BIPV/T linked to ASHP (ii) Roof integrated BIPV/T linked to ASHP and storage (Kamel, Ekrami, Dash, Fung, & Hailu, 2015)	15
Figure 2.9: Case studies of (i) Varennes Library (ii) JMBS building.....	15
Figure 2.10: Schematic of JMBS BIPV/T system (Bambara, 2012)	16
Figure 2.11: The schematic of (i) Conventional thermal wheel (ii) BIPV/T system in winter mode (iii) Proposed BIPV/T-TW system in winter mode (Shahsavari & Khanmohammadi, 2019)	17
Figure 2.12: Matrix-based semi-transparent PV (left), Process induced thin-film PV (centre) and Intrinsic-based fully transparent PV cell technology (right) (Kapsis, 2016)	18
Figure 2.13: Cross-sectional view of (a) STPV/T façade (b) STPV/T roof (c) opaque BIPV/T façade (d) opaque BIPV/T roof with an air duct (Vats & Tiwari, 2012).....	19
Figure 2.14: The three prototypes implemented for double skin façade integration with PV. Left to right: Prototype A, B, and C. (Gaillard, Ménézo, Giroux, Pabiou, & Le-Berre, 2014).....	25
Figure 2.15: The (i) Block diagram (ii) Basic sketch representation of the analyzed system (Martin-Escudero, Salazar-Herran, Campos-Celador, Diarce-Belloso, & Gomez-Arriaran, 2019)	25
Figure 2.16: Drawing of PVB-DSF system (Luo, et al., 2018)	26

Figure 2.17: Reducing peak load demand through the use of flexible energy demand (Lizana, Friedrich, Renaldi, & Chacartegui, 2018).....	29
Figure 2.18: Classification of demand-side management and demand response (Shariatzadeh, Mandal, & Srivastava, 2015)	31
Figure 2.19: (i) Day-ahead demand-side bidding for day-ahead pricing and storage charging (ii) Building cooling load shifting using DBS and DFR strategies (Yan, Xue, Wang, & Cui, 2015)	32
Figure 2.20: Average length of the time periods with a stopped heat pump calculated for a residential heating system (left) Dependence of flexibility on the heat pump power (P_{HP}) and the capacity of the tank (right) (Schuetz, et al., 2017).....	33
Figure 3.1: Schematic of i) reference (BIPV-HPWH) ii) ducted BIPV/T-HPWH system, iii) a passive solar design.....	36
Figure 3.2: Building thermal network	38
Figure 3.3: Heat pump refrigerant diagram	40
Figure 3.4: Modelled thermal storage.....	42
Figure 3.5: Energy balance per tank node	42
Figure 3.6: BIPVT thermal resistance network	44
Figure 3.7: Control strategies i) Reference, ii) Daytime charging, iii) Critical Peak Pricing, and iv) Time-of-Use.....	47
Figure 3.8: Parametric STPV packing factor bounds i) Upper bound at 0.9, ii) Lower bound at 0.1, and iii) Reference at 0.5	48
Figure 3.9: Parametric relative solarium size bounds i) Upper bound at 2.5, ii) Lower bound at 0.5, and iii) Reference at 1	49
Figure 3.10: Mechanical system electricity consumption during the heating season.....	52
Figure 3.11: Mechanical system net energy used during the heating season	52
Figure 3.12: Power consumption on a typical cold sunny day on February 10 th with a daily average temperature of -13 °C	53
Figure 3.13: Parameter influence on the BEFI for the reference configuration	55
Figure 3.14: Parameter influence on the BEFI for the ducted configuration	55
Figure 3.15: Parameter influence on the BEFI for the passive solar configuration	56
Figure 4.1: Future Buildings Laboratory at Concordia University.....	59
Figure 4.2: Future Building Laboratories (FBL) floor plan schematic.....	60

Figure 4.3: Experimental setup	61
Figure 4.4: Fan coil and heat pump water heater temperature setpoints	63
Figure 4.5: Installed Rheem Heat Pump Water Heater with ducting	64
Figure 4.6: Installed iVector fan coil	65
Figure 4.7: Thermocouple placement. Red Dots: Room temperature. Blue Dots: Inlet/outlet duct temperatures	67
Figure 4.8: Room temperatures in test cell 3 on December 11 th (cloudy) and 12 th (sunny), 2021	68
Figure 4.9: Room temperatures in test cell 4 on December 11 th (cloudy) and 12 th (sunny), 2021	69
Figure 4.10: Heat pump water temperature out of the tank, air temperature out, and electricity consumption on December 11 th (cloudy) and 12 th (sunny), 2021	70
Figure 4.11: Test cell 3 room temperature simulation and experimental results comparison on December 11 th and 12 th , 2021	71
Figure 4.12: Heat pump water temperature simulation and experimental results comparison on December 11 th and 12 th , 2021	72

List of Tables

Table 3.1: Key building parameters.....	39
Table 3.2: Key heat pump specifications.....	40
Table 3.3: BIPVT specifications.....	44
Table 3.4: Parametric analysis specifications.....	50
Table 3.5: Optimal parametric values.....	58
Table 4.1: Key experimental equipment used.....	62
Table 4.2: Experimental instrument accuracy and implementation.....	65
Table 4.3: List of sensors installed and positions.....	66
Table 4.4: Average deviation and RMSE comparing the simulation and experimental results ...	72

Nomenclature

A	Area (m ²)
C	Capacitance (J/K)
c_p	Specific heat capacity of water (kJ/(kg·K))
L	Height of tank nodes (m)
k_w	Thermal conductance of water (W/(m·K))
m	Mass flow rate (kg/h)
P_{flex}	Power consumed while utilizing a demand response strategy (kW)
P_{ref}	Power consumed during the reference case (kW)
Δt	Duration of flexibility event (s)
t	Start time of the flexibility event (s)
T	Temperature (°C)
UA	Overall heat transfer coefficient (W/K)

Subscripts

$1 \rightarrow 8$	Tank nodes 1 to 8, from the top to bottom of the tank, respectively
$1,2$	Solarium and house floor, respectively
<i>baseboard</i>	Heat gained from baseboard heaters
<i>coil</i>	Tank heat exchanger coil
<i>f</i>	Floor
<i>FC</i>	Fan coil
<i>g</i>	Ground
<i>gains</i>	Internal gains into the zone, including occupancy, lighting, and any additional heat gained
<i>i</i>	Tank nodes
<i>in</i>	Input to the tank heat exchanger coil
<i>inf</i>	Infiltration into the zone
<i>loss</i>	Loss to the environment

<i>mix</i>	Inversion mixing
<i>o</i>	Outdoor
<i>out</i>	Output of the tank heat exchanger coil
<i>r</i>	House
<i>s</i>	Solarium
<i>sol</i>	Solar radiation gain
<i>sur</i>	Environment
<i>w</i>	Wall

Acronyms

<i>BEFI</i>	Building energy flexibility index
<i>BIPV/T</i>	Building-integrated photovoltaics with thermal recovery
<i>COP</i>	Coefficient of performance
<i>DR</i>	Demand response
<i>FBL</i>	Future Building's Laboratory
<i>HVAC</i>	Heating, ventilation, and air-conditioning
<i>HPWH</i>	Heat pump water heater
<i>RC</i>	Resistance-capacitance
<i>STPV</i>	Semi-transparent photovoltaics
<i>TOU</i>	Time-of-use
<i>WWR</i>	Window to wall ratio

Chapter 1. Introduction

In Canada, 17% (18% in Quebec) of the total energy used is for residential buildings, and 82% (79% in Quebec) of that is used solely for space heating and domestic hot water (Office of Energy Efficiency, 2014). Heat pumps, renewables, and storage systems are often utilized to reduce the overall energy used by increasing the overall system's coefficient of performance (COP) and storing additional heat. Strategies involving various demand response (DR) techniques are also used to introduce a more flexible design based on the grid's needs. This includes alleviating the grid's stress during peak events or reducing the overall energy used and cost (Patteeuw, Henze, & Helsen, 2016). In particular, the electricity demand in Quebec, Canada, is significantly elevated in the morning and evening during extremely cold days in the winter. As such, the utility provides incentives to reduce consumption during these peak periods, alleviate the grid's stress and provide flexibility to the grid. Energy flexibility is broadly defined as the system's ability to adjust its operation based on the required needs of the user or the grid (Arteconi, Mugnini, & Polonara, 2019). This includes the ability to adapt the operation of high consuming systems such as space heating/cooling units to reduce/shift peak power consumption, alleviate stress on the grid, or energy cost reduction by shifting the operation of systems to off-peak pricing periods (real-time pricing, tiered, etc.).

The flexibility of a building utilizing DR strategies can be quantified through a building energy flexibility index. A typical dynamic building energy flexibility index (BEFI) for energy analysis is defined as the building's capability to either reduce or increase its demand during critical events or when needed for the grid (Athienitis, Dumont, Morovat, Lavigne, & Date, 2020). The average BEFI is defined as the average power shifted during critical periods throughout the simulation length. Flexibility activation requires using an appropriately sized storage system as there is often a temporal mismatch between electricity consumption and generation (Guarino, Cassara, Longo, Cellura, & Ferro, 2015). Therefore, increasing the consumption-generation match or storing generated heat/electricity will help reduce the grid's stress, especially during peak demand periods. This research focuses on maximizing thermal energy stored from photovoltaics by utilizing solar

heat and electricity produced to operate the heat pump, storing the available heat and electricity in a water tank. The stored thermal energy can add flexibility to the system for a demand response incentive or store energy for later use.

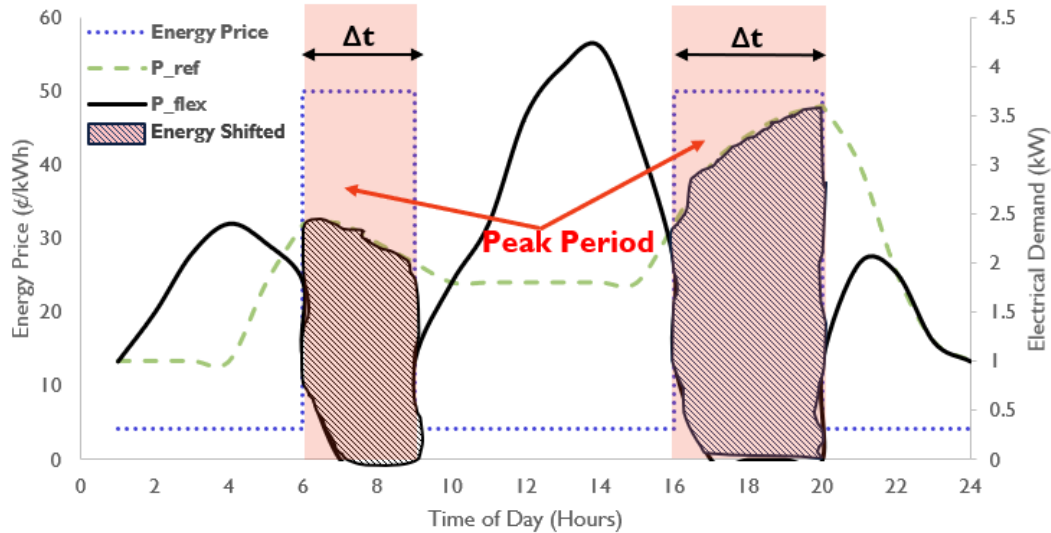


Figure 1.1: Typical demand Quebec demand profile outlining critical peak events for Hydro-Quebec

In addition to maximizing energy produced and stored by photovoltaics, a key consideration is the application of the energy produced. Particularly for building integrated photovoltaics with heat generation (BIPV/T) where the heat generated can be utilized as 1) Pre-heated air for ventilation, 2) Pre-heated air supplied to the source side of an air-to-water heat pump, 3) Pre-heated water for domestic hot water. Utilizing the heat generated by the BIPV systems has a dual purpose: to reduce the PV temperature (increasing electricity generated and reducing the risk of cell degradation) and space heating electricity consumption when pre-heating air or water for various applications. This study focuses on utilizing the pre-heated air for a heat pump water heater (HPWH). This configuration is used to increase the COP of the heat pump during the winter season when the COP and the capacity of these systems decrease with colder outdoor air temperatures.

1.1 Objectives

The goal of this thesis is to model and evaluate the performance of a new configuration where the heat pump is placed within a solar-heated zone (e.g. solarium) and maximize the energy flexibility

(for grid support) of different building-integrated photovoltaics (BIPV) options with heat pumps by identifying optimal ranges for key design variable. The main objectives include:

1. Develop simulation models for different configurations of BIPV, BIPV/T, and semi-transparent photovoltaics (STPV) with an HPWH (Figure 1.2; see Chapter 3 for more detail on all configurations studied).
2. Analyze and compare a new system configuration (heat pump placed within a solarium) – named “passive solar configuration” with more standard configurations with BIPV/T as the heat source for the heat pump and BIPV (outdoor air as heat pump heat source) configurations.
3. Determine optimal ranges for key design parameters to maximize the energy flexibility of the systems with different control strategies implemented.
4. Test and evaluate the new passive solar configuration and compare the simulation model using real-time data to partially verify the model and in Concordia University’s Future Buildings Laboratory (FBL).

This study analyzes the possibility of combining demand response techniques with the various configurations of BIPV-HPWH to maximize the system's flexibility by determining the optimal size of thermal storage, building size, and heat pump size for a single-family house in Montreal. This is done to identify the optimal values of the parameters to properly size the different components and determine what parameters have the highest impact on each configuration. Additionally, the electricity consumption performance of the new passive solar configuration (using solar-heated air from the solarium as heat pump source) is compared with the typical applications of BIPV/T. Maximizing flexibility during peak events is essential to relieve stress on the grid from buildings’ high-energy demand during those peak periods (between 6:00 – 9:00 am and 4:00 – 8:00 pm). By utilizing a heat pump in a solar heated solarium to pre-heat a water tank during the daytime, the stored energy can help reduce or eliminate the demand over the two periods, while the STPV generates part of the electricity consumed by the heat pump. Finally, the experimental proof-of-concept will partially verify the simulation results and provide validation of the new passive solar design and concept.

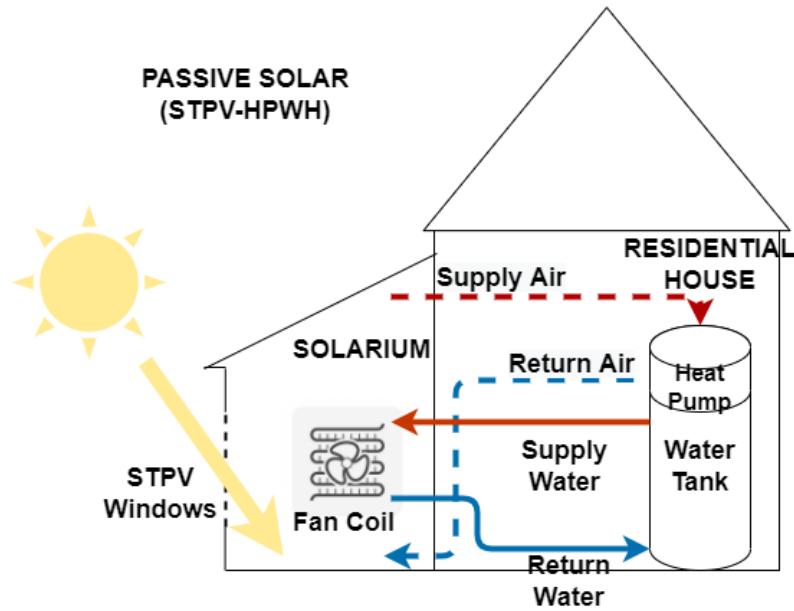


Figure 1.2: Schematic illustrating the main configuration studied (STPV-HPWH)

1.2 Thesis Overview

This thesis is presented as follows: **Chapter 1** introduces the objectives and topics discussed in this thesis. **Chapter 2** reviews the literature and current state of the knowledge regarding BIPV/T, STPV and their applications, as well as energy flexibility and smart heat pumps. **Chapter 3** describes the simulation analysis, including a detailed description of the model and results. **Chapter 4** outlines the experimental setup and compares the experimental results with the simulation results. Finally, **Chapter 5** highlights the key conclusions of this work, the scientific contribution and the work that still needs to be completed.

Chapter 2. Literature Review

2.1 Introduction

This review covers the literature on 1) building-integrated photovoltaics with thermal recovery (BIPV/T), 2) semi-transparent photovoltaic (STPV), and 3) smart heat pumps and grid flexibility. The section on BIPV/T and STPV will focus on their thermal performance and design considerations. The section on cold climate heat pumps will briefly describe heat pumps in general and summarize the air-to-water heat pumps available in the market. The section on smart heat pumps will focus on demand response, storage sizing, and grid flexibility with respect to heat pumps.

2.2 BIPV/T Systems

One essential aspect of a BIPV system is that the photovoltaic panels and supporting structures act as an exterior building material, replacing materials such as shingles on a roof or cladding on façades while producing electricity (Yang T. , 2015). The integration into the building improves the aesthetic appeal of the building while eliminating the need for additional land to implement a PV farm (Chen, Athienitis, & Galal, 2010). However, overheating can be a major issue leading to the simultaneous decrease in lifespan and electricity production. A solution to this issue is the use of BIPV/T. A BIPV/T system can cool down the PV panels through either natural (also called passive BIPV/T systems) or mechanically ventilating (also called active BIPV/T systems) the BIPV system.

BIPV/T systems can be integrated into various surfaces such as roofs, façades, skylights, and windows (Yang T. , 2015). A BIPV/T system converts a portion of the incoming solar radiation into either electricity (the amount is dependent on the type of BIPV cell) or useful heat gain; the rest is reflected. In this way, the electrical performance is improved, and useful heat is gained when heat is recovered through the channel's air flow (Yang T. , 2015), since PV panels generate more electricity at lower the cell temperature. Currently, there are three types of coolants to recover heat from a flat plate BIPV/T (i) air, (ii) water, and (iii) refrigerant, as seen in Figure 2.1.

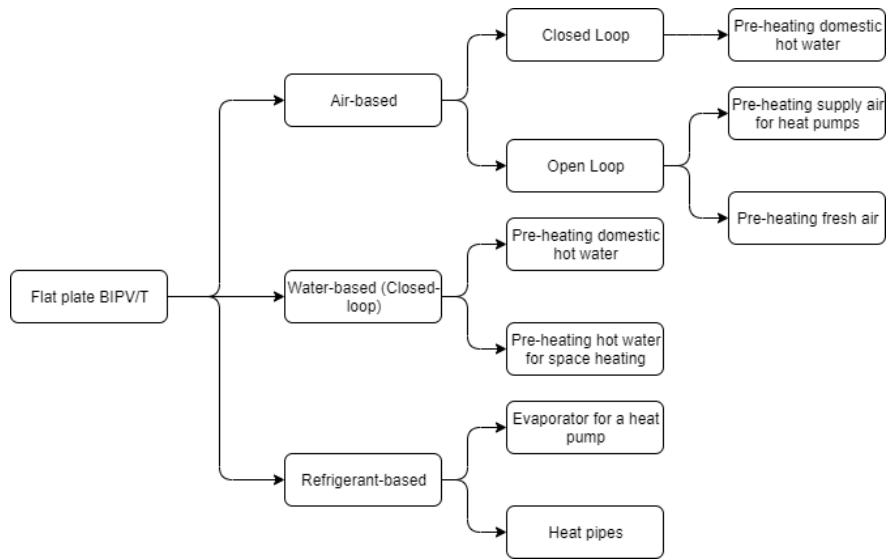


Figure 2.1: Categorization of flat plate BIPV/T systems (Yang T. , 2015)

The air-source solution is the cheapest in terms of panels and installation fees as they are the easiest to install and need very little maintenance. This is the major reason the air systems have become more adopted in cold climates. The advantages and disadvantages of utilizing an air-based system are outlined as follows (Kamel, Fung, & Dash, 2015):

Advantages of air-based BIPV/T systems:

- Less complex and easy to install.
- Inexpensive panels and installation.
- Easier and less expensive maintenance.
- No concern with damage due to leakage or corrosion
- Avoids issues of freezing or boiling the coolant.
- No high-pressure protection is needed.

Disadvantages of air-based BIPV/T systems:

- Low heat transfer rate due to the low heat capacity of air.
- A higher flow rate is necessary.

Additionally, air source BIPV/T can be open-loop and used to pre-heat fresh air for space heating (Yang T. , 2015; Delisle, 2015; Bambara, 2012) or used as a source for a heat pump to increase

its coefficient of performance (COP) (Kamel, Ekrami, Dash, Fung, & Hailu, 2015; Kamel & Fung, 2014) during cold weather. An open-loop system configuration allows outdoor air to cool the BIPV/T modules by convection (Candanedo, Athienits, Candanedo, O'Brien, & Chen, 2010), as shown in Figure 2.2 with heat transferred through an air-to-water heat exchanger. An open-loop configuration is typically used for air-based BIPV/T systems as PV modules tend to overheat in closed-loop systems (Candanedo, Athienits, Candanedo, O'Brien, & Chen, 2010). A closed-loop configuration recirculates the air through the BIPV/T system allowing for a higher outlet temperature than an open-loop system, as seen in Figure 2.2. Closed looped configurations are commonly used in water-based systems. However, an air-based closed-loop system can heat domestic hot water (Zondag & Helden, 2003).

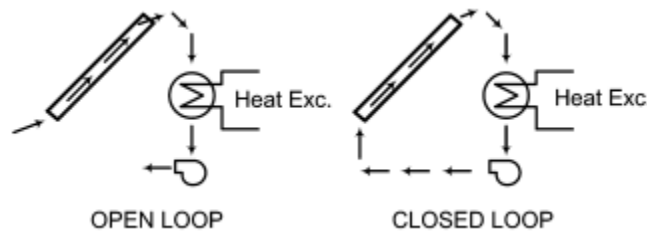


Figure 2.2: Open-loop (left) and closed loop (right) configurations (Candanedo, Athienits, Candanedo, O'Brien, & Chen, 2010)

This review will solely focus on air-based systems. Air systems have the advantage that they need no maintenance, and air leaks affect their performance. In addition, there are no active elements (fans, pumps, etc.) located in the building envelope which remains a durable passive subsystem.

Water-based systems use a closed-loop system and can be used to pre-heat water for domestic hot water use or space heating. Water systems are more effective than air as a coolant as water has a higher heat absorption rate (Chow, et al., 2009; Debbarma, Sudhakar, & Baredar, 2017). The advantages and disadvantages of a water-based system are defined as follows (Kamel, Fung, & Dash, 2015):

Advantages of water-based BIPV/T systems:

- High heating capacity, thus a higher heat transfer rate can be achieved.

Disadvantages of water-based BIPV/T systems:

- Complex system, thus, harder to install and maintain.
- Expensive panels and installation.

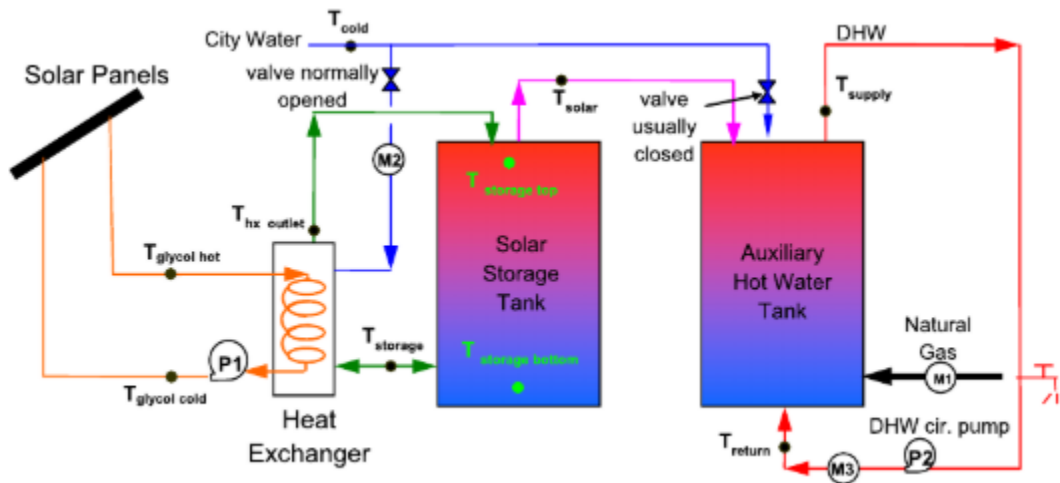


Figure 2.3: Schematic of a solar domestic hot water system (Ghorab, Entchev, & Yang, 2017)

A refrigerant-based BIPV/T uses the BIPV/T panel as an evaporator with refrigerant flowing along the length of the BIPV/T modules, as shown in Figure 2.4 below (Tyagi, Kaushik, & Tyagi, 2012; Tsai, Hsu, & Yang, 2013; Tsai H.-L. , 2015). The advantages and disadvantages of a refrigerant-based system are defined as follows (Al-Waeli, Kazem, Chaichan, & Sopian, 2019):

Advantages of refrigerant-based BIPV/T systems:

- A higher heat transfer rate can be achieved with high heating capacity and thermal conductivity.
- Increased capacity if used with a heat pump.
- Combining PV and the evaporator in one system leads to savings in terms of capital and operating costs.

Disadvantages of refrigerant-based BIPV/T systems:

- Complex system, thus, harder to install and maintain.

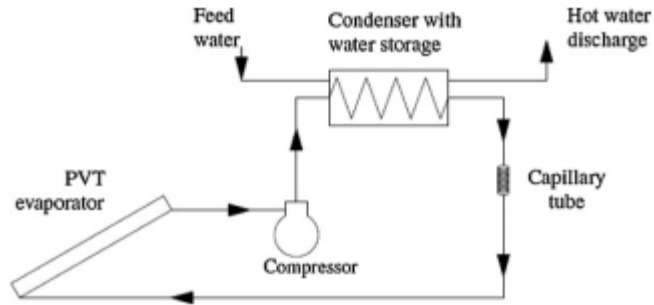


Figure 2.4: Schematic of a PVT integrated heat pump (Tyagi, Kaushik, & Tyagi, 2012)

2.2.1 Air-Based BIPV/T Systems

This section will cover air-based BIPV/T systems. This includes identifying the common channel configurations and key design parameters associated with air-based BIPV/T systems.

The thermal recovery of air-based BIPV/T systems generally uses mechanical ventilation to make use of the heat generated by the BIPV/T to pre-heat air or water going into the building, heat exchanger, or heat pump. There are different variations of BIPV/T systems, including varying air channel configurations and glazing. These configurations are listed as follows:

- **Unglazed.** An unglazed PV module consists of the PV module and insulated back sheet, as shown in Figure 2.5 (Zhang, Zhao, Smith, Xu, & Yu, 2012). This configuration eliminates solar radiation losses due to a possible cover and reduces any excessive overheating due to a cover.
- **Glazed.** A glazed unit has an additional pane of glass on top of the PV module separated by an air gap through which the air flows, as shown in Figure 2.5 for a single- and double-glazed module (Zhang, Zhao, Smith, Xu, & Yu, 2012). This configuration reduces the solar radiation transmitted the electricity generated and can increase the temperature of the PV cells, increasing the thermal performance of the BIPV/T (Khaki, Shahsavar, Khanmohammadi, & Salmanzadeh, 2017).
- **Double pass.** A double pass BIPV/T unit allows air to flow between the glass pane and the PV module as well as below the PV module (Zhang, Zhao, Smith, Xu, & Yu, 2012). This configuration can be seen in Figure 2.5. The advantage of this configuration is that the extra temperature increase from the glazing is reduced with the dual ventilation.

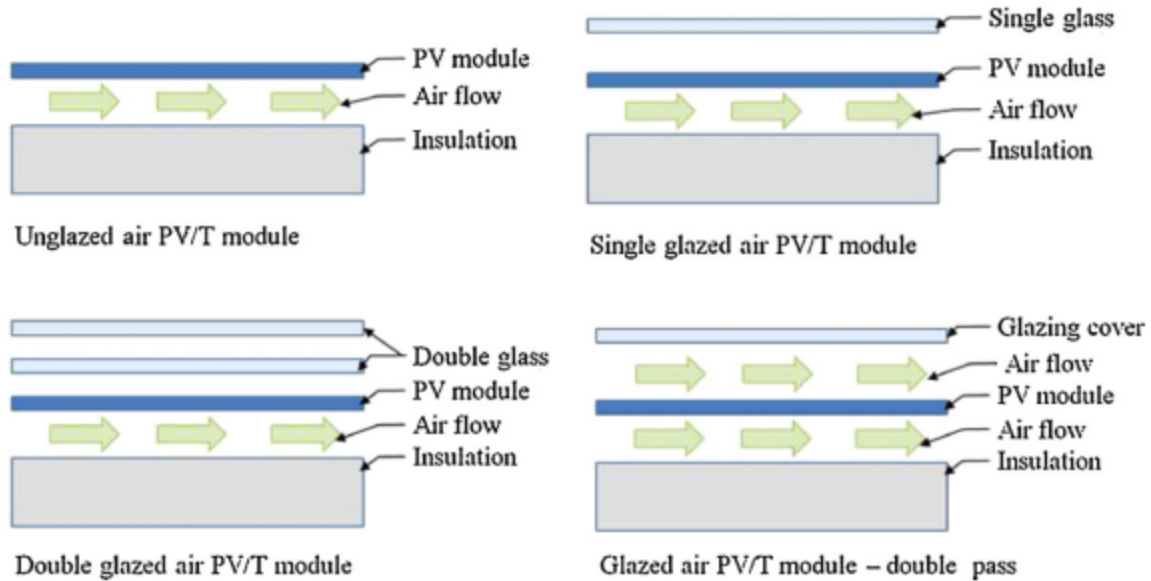


Figure 2.5: Different configurations of PVT modules (Zhang, Zhao, Smith, Xu, & Yu, 2012)

Additionally, baffles or fins can be added into a channel to increase the heat transfer rate and potentially decrease the PV cell temperature (Yang T. , 2015).

2.2.2 BIPV/T Design Parameters

BIPV/T systems have been thoroughly investigated for various aspects of the BIPV/T design. The flow rates from ASHRAE 2019, which states the recommended range for air channel flow rates as between $20 \text{ kg}/(\text{h}\cdot\text{m}^2)$ and $120 \text{ kg}/(\text{h}\cdot\text{m}^2)$ as with the increase of the flow rate, the temperature rise through the channel is reduced (ASHRAE, 2019). Additionally, parameters such as the channel depth, tilt, length and general PV configurations, climate effects, and material of the cells have all been analyzed throughout the years. This section will summarize the key findings from previous studies and provide reasonable design parameters for BIPV/T collectors.

2.2.2.1 BIPV/T dimensional parameters

The channel depth significantly impacts the thermal efficiency, allowable channel velocity, and air volume to pass through the channel. Reducing the channel depth increases the flow velocity and the heat gained from the PV surface (Rounis, 2018). Adeli et al. (2012) found that the thermal efficiency increases logarithmically with respect to the channel depth, reaching an asymptote at around 0.1 m and thermal efficiency of around 48%, as shown in Figure 2.6. In contrast, Farshchimonfared et al. (2015) concluded that the optimal channel depth is directly related to the

L/W ratio for areas between 10 and 30 m². This study showed that for the specified areas and a constant temperature of 10°C, the optimal channel depth is typically between 0.026 and 0.09 m. Gan (2009) similarly associated the air gap depth to be directly related to the length of the PV roof system. This study showed that to prevent overheating the PV modules, the air cavity depth should be between 0.14 – 0.16 m, depending on the length of the PV system. Kasaeian et al. (2017) performed an experimental analysis. They determined that at larger depths, the mass flow rate is required to similarly be higher to obtain the same thermal and electrical efficiency as smaller channel depths. Based on these studies, the ideal channel depth was around 0.08 – 0.16 m.

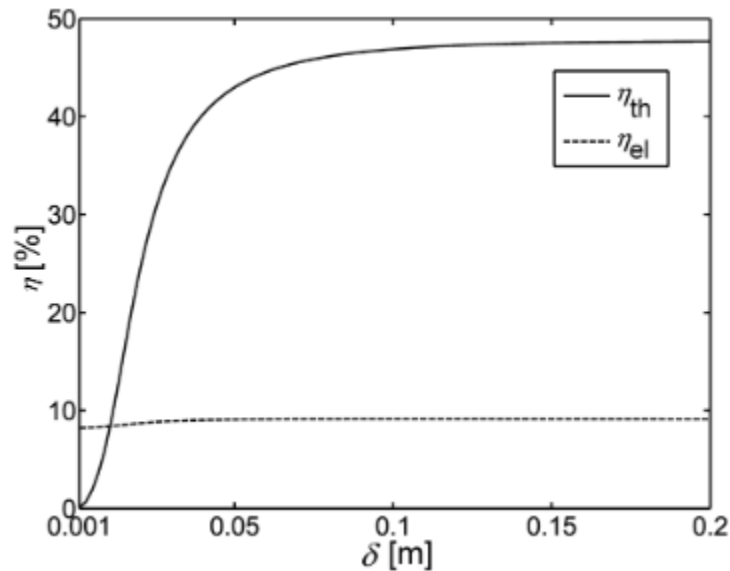


Figure 2.6: Variation of thermal and electrical efficiency with respect to the duct depth (Adeli, Sobhnamayan, Farahat, Alavi, & Sarhaddi, 2012)

The channel length of the collector influences the absorption rate of the air. As the channel length increases, the air temperature will eventually reach a steady-state temperature along with the PV cell temperature (Rounis, 2018). This effect reduces the convective heat exchange while increasing the thermal efficiency and decreasing the electrical efficiency (Rounis, 2018). It has been found that the suggested maximum length for the BIPV/T system is around 8 m as, at lengths greater than 8 m, the thermal and electrical efficiencies converge, and there is no added thermal or electrical benefit from the additional length. (Rounis, 2018; Tonui & Tripanagnostopoulos, 2007; Tiwari & Sodha, 2007) .

The collector tilt influences the irradiation striking the surface of the BIPV/T collector. The ideal tilt angle to maximize the annual irradiation equals the latitude of the collector (Rounis, 2018). At this “ideal” tilt angle, the collector's maximum electrical and thermal efficiencies can be reached. Gan (2009) studied the effect of the roof tilt on the maximum and mean PV cell temperatures achieved by the BIPV/T collectors utilizing a CFD analysis. The study showed that the maximum and average PV cell temperature decreased with the increase of the tilt angle, reaching an asymptote for tilt angles higher than 60°.

2.2.2.2 Climate Effects

The electrical performance is directly related to solar irradiation. However, as the irradiation increases, the electrical efficiency decreases while the thermal efficiency increases (Rounis, 2018). This effect is caused by the increase in the solar cell temperature as the outlet air temperature from the BIPV/T is similarly increased.

The wind affects the temperature of the solar cells, as with a higher wind velocity, the cell temperature decreases. As the wind speed increases, the thermal efficiency, the temperature rise from the BIPV/T, and the PV cell temperature decrease (ASHRAE, 2019; Gautam & Andresen, 2017; Chen, Athienitis, & Galal, 2010; Yang & Athienitis, 2014). This is due to the cooling effect on the PV cell temperature, which reduces the temperature and, therefore, the heat transfer rate between the PV cell and the air within the channel (Rounis, 2018).

2.2.3 BIPV/T Applications

Typical applications of BIPV/T include preheating air for either a heat pump or providing heating for a building.

2.2.3.1 BIPV/T integrated with heat pumps

This section provides a detailed description of previous studies for various methods of integrating BIPV/T and heat pump systems. The boost of pre-heated air from the BIPV/T may help increase the heat pump's operating range in a cold climate. As the temperature decreases, the heat pump's capacity and coefficient of performance (COP) decreases significantly (Kamel, Fung, & Dash, 2015). Therefore, the pre-heated air from BIPV/T will improve the overall performance of the heat pump by increasing the inlet temperature to the heat pump by up to 10 – 40°C (Bigaila & Athienitis, 2017; Dumoulin, 2019) and therefore increases the evaporating temperature in the heat

pump (Kamel, Fung, & Dash, 2015). Additionally, the pre-heated air can decrease the amount of time the heat pump will be in defrost. However, it is important to match the flow rate of the BIPV/T with the required air flow rate from the heat pump manufacturer (Hailu, Dash, & Fung, 2015). If the flow rate from the BIPV/T does not match the heat pump's required flow, the heat pump will require mixing the BIPV/T air with ambient air to get a sufficient flow rate. This will, in turn, reduce the temperature rise and lower the energy savings.

In general, there are two different methods of combining the BIPV/T and ASHP (Rounis, 2018):

- **BIPV/T pre-heating air for the heat pump.** The outlet air from the BIPV/T is directly fed to the air source heat pump (ASHP) instead of ambient air. In the case of insufficient air from the BIPV/T, the air supplied to the ASHP is mixed with ambient air, and this creates a diluted mixture with a higher temperature than the ambient air but lower than the outlet air from the BIPV/T. During the summer (cooling mode), the fans will be turned off, or the air will be bypassed.
- **Independent operation.** The systems work independently to reach the setpoint. Each unit provides heat to the building (BIPV/T system by providing pre-heated air to the space and the heat pump simultaneously providing additional heat). If the setpoint is reached, the heat pump is shut off.

This section will focus on the application of pre-heating air for heat pumps. Delisle et al. (2016) compared the use of outlet air from BIPVT for pre-heating air (system 1) and the pre-heating DHW with a heat exchanger (system 2) as well as two different heat pump applications (systems 3 and 4) with more standard BIPV and PVT systems. The configurations for these applications can be seen in Figure 2.7 below. Different housing archetypes for different sizes or bungalows and 2-storey houses and locations across Canada are also studied.

This study shows that system 2 (DHW heating with heat exchanger) had the highest useful electrical energy for all simulated archetypes, followed by the PVT system and the air-to-water heat pump. In contrast, system 1 (pre-heating fresh air) had the lowest electricity produced. However, the break-even cost for system 2 was the highest of all the configurations, while system 1 had the lowest. Delisle concluded that any of the systems examined could be selected if the incremental cost of the configuration was less than or equal to the break-even cost.

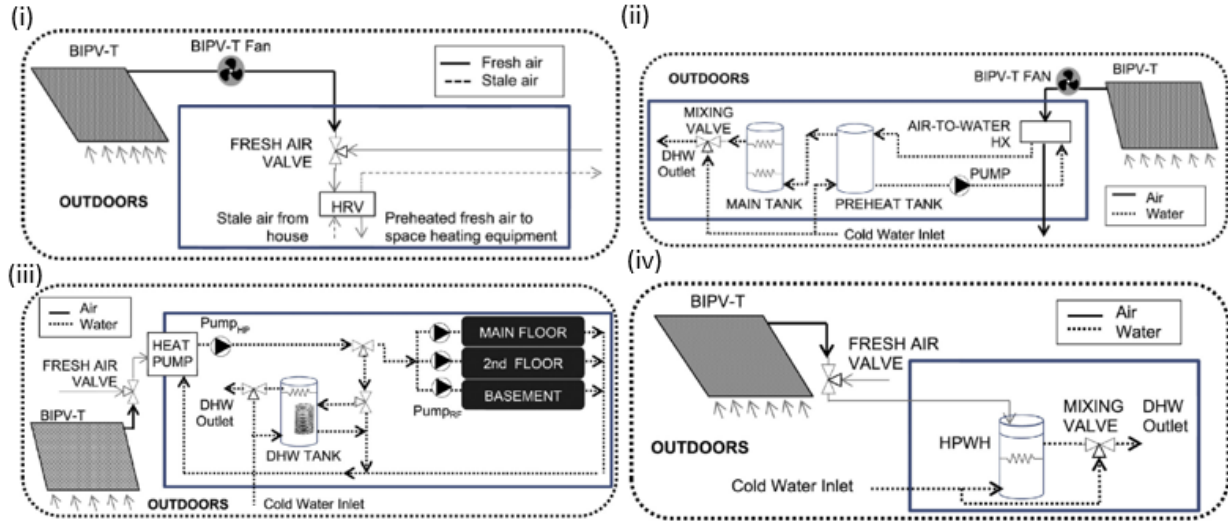


Figure 2.7: Schematic of BIPV/T applications studied (i) Pre-heating fresh air (ii) DHW heating with an air-to-water heat exchanger (iii) Air-to-water heat pump for DHW and space heating (iv) DHW with a heat pump water heater (Delisle & Kummert, 2016)

Hailu et al. (2015) conducted a simulation analysis for a house in Alaska to compare the use of ambient air and pre-heated air fed to the heat pump. The pre-heated air configuration can be seen in Figure 2.8 (i). The results showed that between -3°C and 10°C , the heat pump's COP had a significant improvement. However, this was not the case for temperatures lower than -10°C , where limited improvements could be seen. A similar study was conducted by Kamel et al. (2015) for BIPV/T pre-heated air fed to a heat pump with thermal storage. PVT pre-heated air reduced the heat pump's electricity consumption by 20% and increased the heat pump's peak COP from 2.74 to 3.45 without thermal storage.

2.2.3.2 BIPV/T pre-heated fresh air

Pre-heating air for buildings is one of the simpler and cost-effective methods for utilizing the thermal recovery of the BIPV/T. There is always a need for a fresh supply of air into a building to create a higher heating load during the heating season (Rounis, 2018). The BIPV/T system can provide pre-heated fresh air directly to the space or with a mixture of pre-heated air and cooler ambient air, depending on the building setpoint (Rounis, 2018). The Varennes Library in Quebec, Canada, has a unique integration of BIPV and BIPV/T. This entire system is used to power the building, successfully becoming an NZEB. The section of roof that houses the BIPV/T is used to

pre-heat the air to the building during the heating season and generate up to about 220 kWh of heat for a roof area of 173 m² on a sunny day (Rounis, 2018).

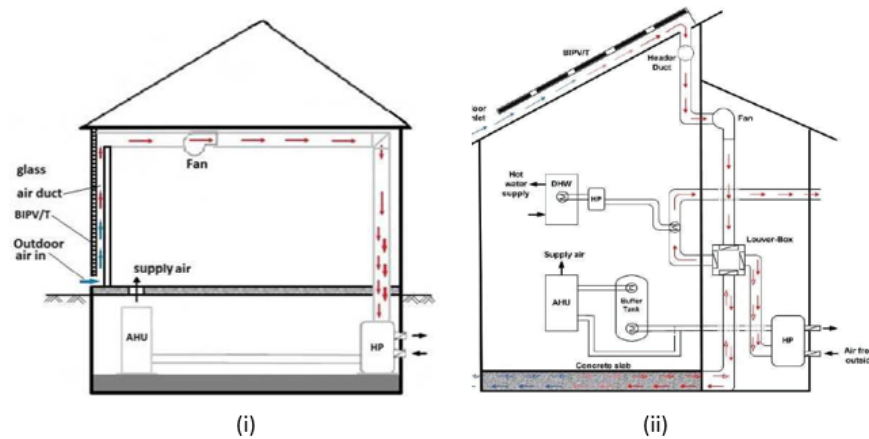


Figure 2.8: Schematic of (i) Wall integrated BIPV/T linked to ASHP (ii) Roof integrated BIPV/T linked to ASHP and storage (Kamel, Ekrami, Dash, Fung, & Hailu, 2015)



Figure 2.9: Case studies of (i) Varennes Library (ii) JMSB building

Another case study in Canada is Concordia University's John Molson School of Business building. This system pre-heats the air during the winter and discards the air in the summer (Rounis, 2018). This system can pre-heat the air by up to 20°C even at exterior temperatures below -15°C. The JMSB building can produce an annual useful heat gain of 55 MWh for a BIPV/T area of 288 m² (Bambara, 2012). The wind speed significantly impacted the thermal efficiency by up to 15%, with a reduction in heat gain of over 30%. Thus, it was suggested that the wind speed be considered in predicting BIPV/T energy production (Bambara, 2012).

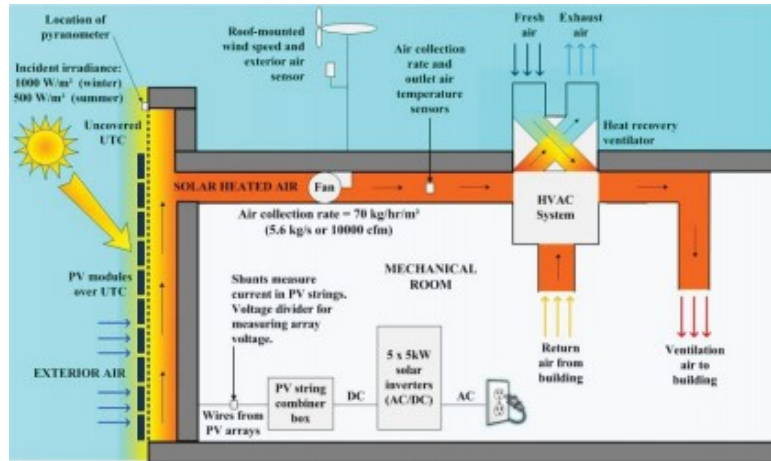


Figure 2.10: Schematic of JMBS BIPV/T system (Bambara, 2012)

A unique application analyzed by Shahsavari et al. (2019) combined the use of a heat recovery wheel and a BIPV/T system (BIPV/T-TW), as can be seen in Figure 2.11 ii below. This proposed solution was compared to both a conventional heat recovery wheel system (Figure 2.11 i) and a BIPV/T system (Figure 2.11 iii). Utilizing these systems, an analysis was conducted for the useful energy gained in the climate of Kermanshah, Iran. The BIPV/T-TW system obtained an annual useful energy gain higher than 400% compared with the BIPV/T system. Additionally, the BIPV/T-TW gained 24% more useful energy than the TW system annually. An additional analysis was conducted to determine the optimized performance of the highest performing system (BIPV/T-TW) when applying multi-objective optimization using Pareto's theory. The optimizing criteria were based on the useful energy and exergy gained, while the decision parameters included the dimensions of the BIPV/T and the thermal wheel. The optimized electrical performance increased on average by over 750 kW compared to the un-optimized system, while the thermal energy gained increased by around 563.8%. As for the optimal design criteria, the length and width of the PV panels and the diameter of the wheel tended to have higher values, while the depth of the channel and the rotational speed of the wheel was on the lower end.

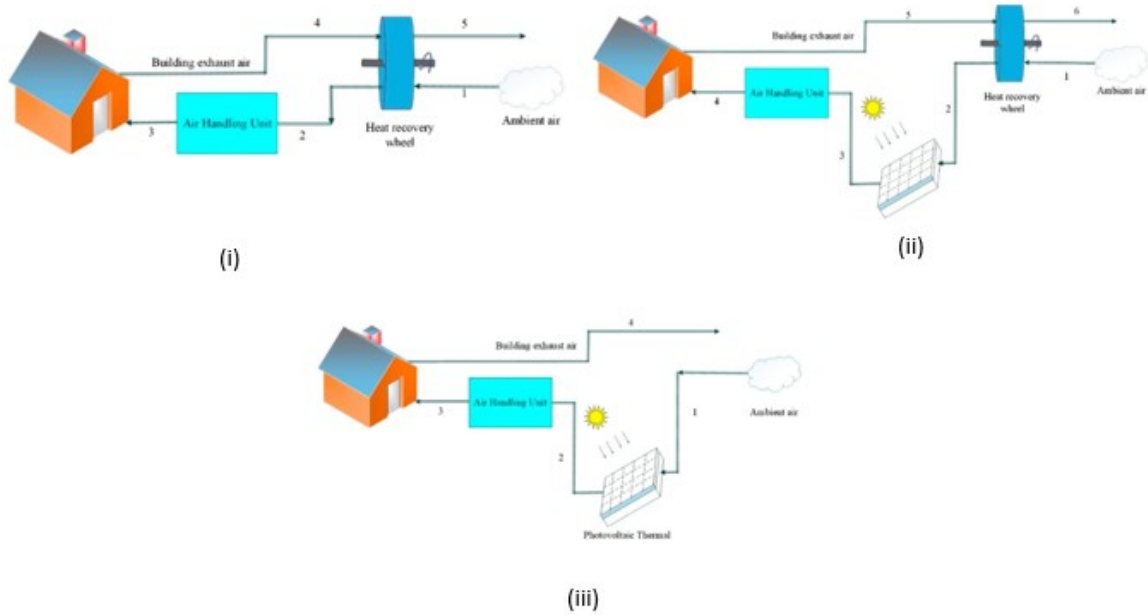


Figure 2.11: The schematic of (i) Conventional thermal wheel (ii) BIPV/T system in winter mode (iii) Proposed BIPV/T-TW system in winter mode (Shahsavari & Khanmohammadi, 2019)

2.3 STPV Systems

STPV windows are a subcategory of BIPV systems. The defining characteristic of STPV is the transparency of the material encasing the cells (i.e. the front and back sheet) and, in some cases, the cells themselves. STPV systems can be categorized based on three different manufacturing processes, as seen in Figure 2.12 below (Kapsis, 2016):

1. **Matrix-based.** The PV cells are spaced such that light can pass between the cells and the back sheet is transparent to allow daylight transmission and partial visibility. Varying the visibility requires varying the packing factor of the cells. This type typically uses opaque crystalline silicon cells; however, other technologies exist, such as micro-spherical Si-based cells (Biancardo, et al., 2006). This type of STPV can have a cell efficiency of up to 27% (National Renewable Energy Laboratory, 2020).
2. **Process-induced.** Voids are created to allow daylight through the PV by partially removing the semiconductor substrate using laser-etching techniques. This process utilizes amorphous silicon or micro crystalline silicon thin-film PV cell. This technology can have

a cell efficiency of up to 14% for amorphous silicon and 23% for copper indium gallium selenide solar cells (CIGS) (National Renewable Energy Laboratory, 2020).

3. **Intrinsic based.** Thin-film technologies are utilized to achieve a fully transparent PV cell. This process is typically utilized for coloured STPV cells and is developed based on polymers, perovskite, amorphous silicon or nano crystalline silicon thin films. Perovskite cells can have up to 25% cell efficiency, while organic PV has up to 17% (National Renewable Energy Laboratory, 2020).



Figure 2.12: Matrix-based semi-transparent PV (left), Process induced thin-film PV (centre) and Intrinsic-based fully transparent PV cell technology (right) (Kapsis, 2016)

2.3.1 STPV Design Considerations

Typical studies for STPV analyze one or more of the following attributes: (i) the window-to-wall ratio (WWR) (Ng, Mithraratne, & Kua, 2013; Lioa & Xu, 2015), (ii) the STPV design (Lynn & Mohanty, 2012; Chae, Kim, Park, & Shin, 2014; Ghosh, Sundaram, & Mallick, 2019), (iii) the orientation of the STPV window (Lu & Law, 2013; McLaughlin, Kapsis, Athienitis, Siassi, & Nichilo, 2014), and (iv) the daylight transmitted into the building (Kapsis, 2016; Wong, Shimoda, Nonaka, Inoue, & Mizuno, 2008; Liu, Sun, Wilson, & Wu, 2020) for the thermal and electrical properties of the STPV module or the effect on the building performance. The thermal recovery of STPV systems (STPV/T) has been analyzed in various applications from the integration into a building with an air duct, but not used as a window as seen in Figure 2.13 (Han, Lu, Peng, & Yang, 2013; Han, Lu, & Yang, 2010; Sun, Ji, Luo, & He, 2011) and the use in double skin façades (Gaillard, Giroux-Julien, Ménézo, & Pabiou, 2014; Peng, et al., 2016).

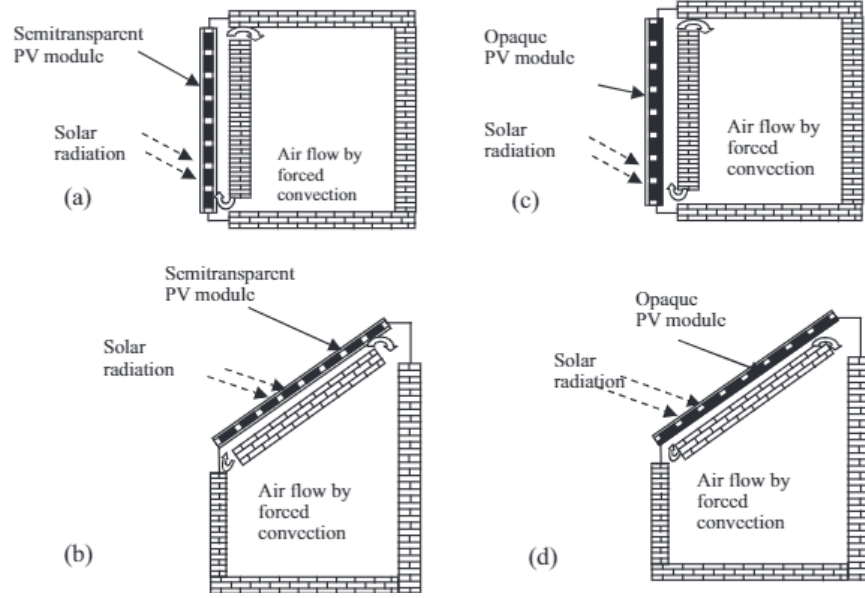


Figure 2.13: Cross-sectional view of (a) STPV/T façade (b) STPV/T roof (c) opaque BIPV/T façade (d) opaque BIPV/T roof with an air duct (Vats & Tiwari, 2012)

2.3.1.1 Window-to-Wall Ratio

The window-to-wall ratio (WWR) influences the electrical performance of the STPV as the lower the WWR, the less surface area for the STPV to produce electricity. STPV and WWR can affect the performance of the building in terms of electricity consumption and heating loads. The study from Ng et al. (2013) shows that for WWR of 70% to 100%, all types of STPV studied outperformed conventional glazing systems when considering the net electricity benefit with a windowless wall STPV electricity production for a warm climate. This claim is reaffirmed from the study by Miyazaki et al. (2005). The study demonstrated that for a WWR of 30% with the optimal solar transmittance and lighting control, the STPV studied had a similar building electricity consumption to the conventional glazed systems. In comparison, at a WWR of 40% and 50%, the STPV performed increasingly better in terms of net electricity use than a standard glazed window. This indicates that at lower WWR, single- or double-glazed windows will have the same effect on the building electrical consumption as using an STPV window without considering the PV generation. Liao et al. (2015) found that a-Si STPV windows in Central China had the lowest cooling loads when installed in a room with a shallow depth and either a large window area or a high room height.

2.3.1.2 Visible Transmittance and Window Properties

Varying the degree of visibility through the STPV can affect the overall performance of both the STPV panel and the building. Vats et al. (2012) found that for different matrix-based STPV modules, a lower packing factor increases the electrical and thermal production as the cell temperature is decreased. Contrarily, the study from Miyazaki et al. (2005) found that the higher the visible transmittance, the lower the overall electricity production. This study also found the optimal solar transmittance for various WWR considering lighting control. The overall near-optimal combination of transmittance of 40% and a WWR of 50% achieved the minimum electricity consumption for the office studied and achieved a reduction of 54% compared to a single glazed window with a WWR of 30%. These studies show that an optimal point can be reached between visible transmittance and electricity production.

In addition to the visible transmittance and solar gain, the type of glass supporting the PV cells can impact the results (Park, Kang, Kim, Yu, & Kim, 2010). Park et al. (2010) concluded that the type of glass had no impact on the overall electrical performance of the STPV, but it may influence the temperature of the matrix-based STPV module. In particular, the solar heat gain and the module temperature can be affected.

2.3.1.3 STPV Window Orientation

The orientation of the STPV window greatly impacts the performance of the electricity produced, as demonstrated by McLaughlin et al. (2014) and Robinson et al. (2009). They found that for the respective buildings studied, as expected, the south-facing STPV windows had the greatest electricity production compared to orientations such as southeast and southwest-facing windows.

2.3.1.4 Daylighting

As a potential replacement for windows, conducting a daylighting analysis is an essential part of the overall analysis of adding STPV since it influences the amount of daylight transmitted into the building and the artificial lighting used. Lu et al. (2013) and Miyazaki et al. (2005) consider daylighting primarily to analyze artificial lighting and the required illumination. Kapsis (2016), Robinson et al. (2009), and Li et al. (2009) have an in-depth analysis on the effect of STPV on daylighting, and consequently, on electricity use and building loads.

Kapsis (2016) demonstrated that different daylighting and shading control strategies had negligible differences when comparing the visible transmittance of STPV. Utilizing a control strategy for

“active” users interacting with the artificial lighting and roller blinds, increasing visible transmittance simultaneously decreases the heating and lighting load. However, the strategy increases the cooling load while decreasing the electricity production from the STPV. Kapsis (2016) found the lowest end-use electricity consumption was with a visible transmittance of 10%. However, using STPV with 10% transmittance does not provide sufficient daylight for the room. Only a minimum visible transmittance of 30% optimizes daylight transmission for an office and the end-use electricity consumption throughout the year.

Wong et al. (2008) found that using an STPV skylight had a negligible contribution to lighting energy savings for a residential building, as the lighting demand is low during the day. The study also analyzed optimization measures to minimize the heat loss during the winter and gain in the summer by including a layer of insulation to the STPV windows. It was found that without these optimization measures, the STPV helps reduce the annual heating loads; however, it will increase the cooling loads during the summer. Nonetheless, optimization measures reduced the heating and cooling loads by about 5%.

Karthick et al. (2018) analyzed the effect of daylighting and the packing factor on the STPV electricity generation and the building cooling loads. The study demonstrated that a higher packing factor has the most electricity generated and the lowest savings for the annual artificial lighting electricity consumption. However, a lower packing factor will increase the annual cooling loads. Therefore, an optimal point is required to balance the daylight gain electricity produced and minimize the cooling loads. This study found this optimal point among the BIPV modules analyzed with a packing factor of 72%.

2.3.1.5 Thermal Recovery

Few studies analyze the thermal recovery aspect of STPV. However, studies can be found that compare the usage of STPV/T and opaque BIPV/T. Vats and Tiwari (2012) compared semi-transparent and opaque BIPV/T for both a façade and roof application with and without an air duct. In each case studied, the STPV/T had the highest temperature output. The temperature difference between the STPV/T and the opaque BIPV/T is significantly higher without an air duct, with a difference of 10°C between the two for both the façade and roof configurations. However, with an air duct, there was significantly less difference between the STPV and BIPV/T for each configuration (up to 2°C difference). The application of a duct decreased the temperature

difference. This signifies the potential for STPV to increase further the temperature for pre-heating applications instead of more standard opaque BIPV/T for the building studied. However, this study does not investigate the impact of different transparencies for the STPV. According to Wong et al. (2008), cell temperatures reduce with the solar cell density of poly-crystalline cells.

2.3.2 STPV Applications

Common applications for STPV windows (aside from simple application in a window or skylight) include the integration in greenhouses/solariums, double-skin façades, novel applications such as venetian blinds.

2.3.2.1 STPV in Greenhouses

Greenhouses are a practical application of STPV as it will simultaneously produce electricity while providing the plants with the daylight needed, reducing the requirement for supplemental lighting. Emmott et al. (2015) analyzed plant growth in a greenhouse with a c-Si STPV façade, a special glass to direct the light, and a thin film façade. The study showed that the thin film STPV tended to absorb more light within the spectrum required for plant growth than the opaque c-Si STPV; however, the opaque STPV had an improved performance in terms of both crop growth and electricity generation compared to the thin-film technology. The use of thin-film was deemed a viable application based on the economic analysis conducted. On the other hand, a more recent study from Bambara and Athienitis (2019) investigated the current and future potential of utilizing STPV cladding to replace supplemental lighting in a greenhouse. The study concluded that the current investment of STPV is not economically viable as the STPV increases the need for supplemental lighting due to the increase of internal shading and generates 40% of the consumed electricity, but the future projection generated over 105% of the consumed electricity and showed a life cycle cost reduction of over 20%. This analysis was conducted based on future predictions of PV cell electrical efficiency as well as artificial light electrical and photon efficiency. A combination of these factors contributed to the increase in electricity generation and life cycle cost reduction for the future predicted values. This study showed the potential reduction in life cycle cost for an application with a high lighting demand, such as greenhouses. The life cycle cost could potentially be reduced in other applications with a lower lighting demand.

Studies have published results highlighting the use of surplus energy from buildings such as greenhouses (Yang & Rhee, 2013) or suggesting placing a heat pump within the heated greenhouse (Benli, 2011). Yang and Rhee (2013) utilized the surplus energy gathered by fan coil units within a 100-m² greenhouse to heat either a lower or high-temperature tank, depending on the mode of operation. The energy gathered was used to heat the greenhouse at night. Their results showed that the energy recovered provided up to 76% for the thermal energy required to heat the greenhouse, especially in March.

A solarium has been proven to maintain a minimum temperature of 10 °C with minimal heating requirements while providing up to 134 kWh/m² of excess heat with proper interior and exterior shading controls (Bastien & Athienits, 2012). Setting the heat pump within this zone will have the dual purpose of increasing the inlet air temperature and providing air conditioning to the solarium. However, previous studies of greenhouses or solariums do not include using a heat pump within the space, focusing on optimizing the heating/cooling systems to regulate the temperature or improve the overall energy efficiency utilizing different renewable technologies (Yang & Rhee, 2013; Benli, 2011; Ozgener & Hepbasli, 2005; Zhang, et al., 2020). Renewable heating technologies studied include solar-, geothermal-, and biomass-powered technologies often coupled with various thermal energy storage technologies such as sensible, latent, or thermochemical storage (Gorjian, Ebadi, Najafi, Chandel, & Yildizhan, 2021).

Examples of such systems include works from Ozgener and Hepbasli (2005) and Benli (2011). They experimentally examined the performance of ground-source heat pumps used to regulate the greenhouse temperatures demonstrating the increased heat pump performance compared to standard systems. Ozgener and Hepbasli (2005) found an increase of 33% in heat pump efficiency on sunny days compared to cloudy days. Lim et al. (2020) demonstrated the positive impact on energy savings utilizing an air-to-water heat pump coupled with pre-heated underground air in a South Korean 330 m² greenhouse. They concluded that an air-to-water heat pump provided a more stable room temperature and a 25% energy savings compared to a conventional air-heater. Hassanien et al. (2018) experimentally investigated using an evacuator tube solar collector-assisted heat pump in a small 26 m² greenhouse. It was found that the addition of an evacuator tube solar collector provided 35% of the annual heating demand for the greenhouse. The monthly average coverage was up to 78% in warmer months such as April and down to 25% in February. A large-

scale solar collector with seasonal thermal storage provided 65% of the greenhouse's annual heating demand (Semple, Carriveau, & Ting, 2017).

Zhang et al. (2020) compiled and compared the use of various control strategies and simulation techniques to optimize a greenhouse's energy efficiency. It is noted that the control strategies within the compiled review did not include any demand response strategies to improve flexibility or consider grid-interaction, nor has this author found studies for improving the heating system's flexibility in greenhouses/solariums.

While heating systems and controls are essential in improving a greenhouse's energy efficiency, Gorjian et al. (2021) found that implementing sensible thermal energy storage improved the energy savings by 28 kWh/m² compared to a greenhouse without storage. Naghibi et al. (2020) compared thermal energy storage with PCM in the tank. The inclusion of PCM proved to increase the energy performance by 10 – 14% with increasing amounts of PCM. The overall system efficiency improved by 28% from a higher solar collector efficiency and thermal ratio. However, system electricity consumption and estimated payback period increased by 1000 – 2000 kWh/year and 7 – 14 years, respectively, based on the percentage of PCM utilized compared to a traditional water storage system.

2.3.2.2 Double skin façade

A few studies integrate the use of STPV with double-skin façades. Through an experimental study, Gaillard et al. (2014) compared a simple façade/roof arrangement with an air gap thickness of 0.7 m (prototype B), 4 m (prototype A) and a façade with air gap thicknesses between 0.6 m and 0.8 m (prototype C), as can be seen in Figure 2.14. The study demonstrated that the façade configuration (prototype C) had the highest temperature rise, followed by prototype A then B. This signifies for the application and location studied that a double skin façade with a lower air gap thickness has more potential for thermal recovery.

Wang et al. (2017) conducted a comparative analysis to determine a suitable application of STPV. The study compared an insulating glass unit of STPV within a double-skin façade (DSF) system. The study found that the DSF configuration in this application had a higher reduction in the solar heat gain; however, the glass unit had better insulation properties. The study further concluded that the operational strategy has a large impact on the performance of the DSF integrated with STPV, as without the optimal strategy, the insulating glass had higher heat load reduction. A similar

comparison was conducted by Ioannidis et al. (2017) for identical modules of STPV, where one unit was integrated with a double-skin façade. This study was conducted experimentally, and the results showed an improvement in the electrical performance with the addition of DSF.



Figure 2.14: The three prototypes implemented for double skin façade integration with PV. Left to right: Prototype A, B, and C. (Gaillard, Ménézo, Giroux, Pabiou, & Le-Berre, 2014)

The study from Martin-Escudero et al. (2019) analyzed an opaque a-Si BIPV/T system integrated with a double skin façade that pre-heated air to a heat pump. This configuration can be seen in Figure 2.15.

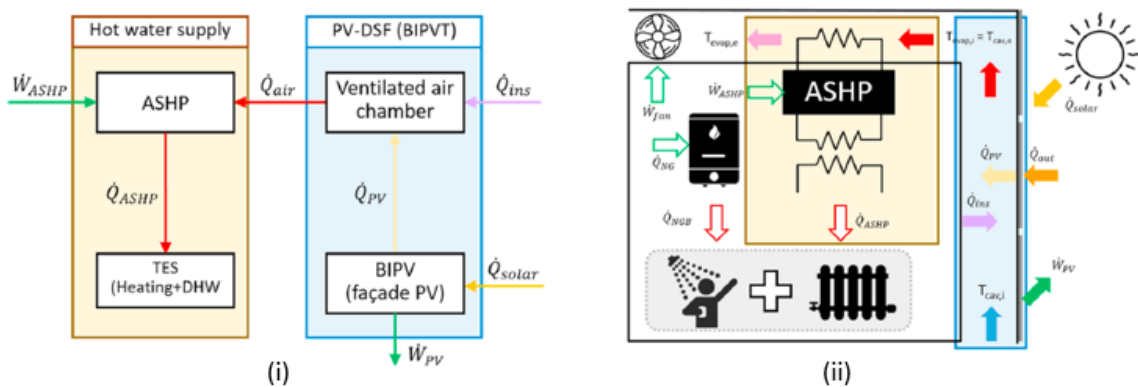


Figure 2.15: The (i) Block diagram (ii) Basic sketch representation of the analyzed system (Martin-Escudero, Salazar-Herran, Campos-Celador, Diarce-Belloso, & Gomez-Arriaran, 2019)

Martin-Escudero et al. (2019) showed the monthly electrical production of the BIPV system, a BIPV/T-DSF façade, and BIPV roof application compared to the electrical demand of the system. The DSF configuration continuously produced less than the demand (~70% of the demand), while the BIPV roof application generated more than the demand for most of the year. The heat pump, utilizing pre-heating air, showed an improvement in efficiency and the time in which the auxiliary system was activated was reduced. The power consumption of the heat pump was reduced by 10%, while the seasonal performance factor was improved by 15%.

2.3.2.3 Novel Applications: Venetian Blinds

An interesting application of STPV-DSF is PV-integrated venetian blinds in DSF (PVB-DSF). The structure for the PVB-DSF can be seen in Figure 2.16. Luo et al. (2018) studied this use of PV blinds, including comparing conventional STPV-DSF and traditional façades. The ventilated PVB-DSF system had a lower heat gain than a standard brick wall. However, the non-ventilated PVB-DSF system significantly increased heat gain of over 1100 W/m^2 compared to the brick wall. In contrast to a conventional STPV-DSF system, the PVB-DSF system had reduced electrical performance. The electrical efficiency for the naturally ventilated and the non-ventilated mode was 6.6% for STPV-DSF, while PVB-DSF had an efficiency around 2.4% - 2.5%. Additionally, the heat transfer coefficient was similarly reduced, while the solar heat gain coefficient (SHGC) increased with PV blinds.

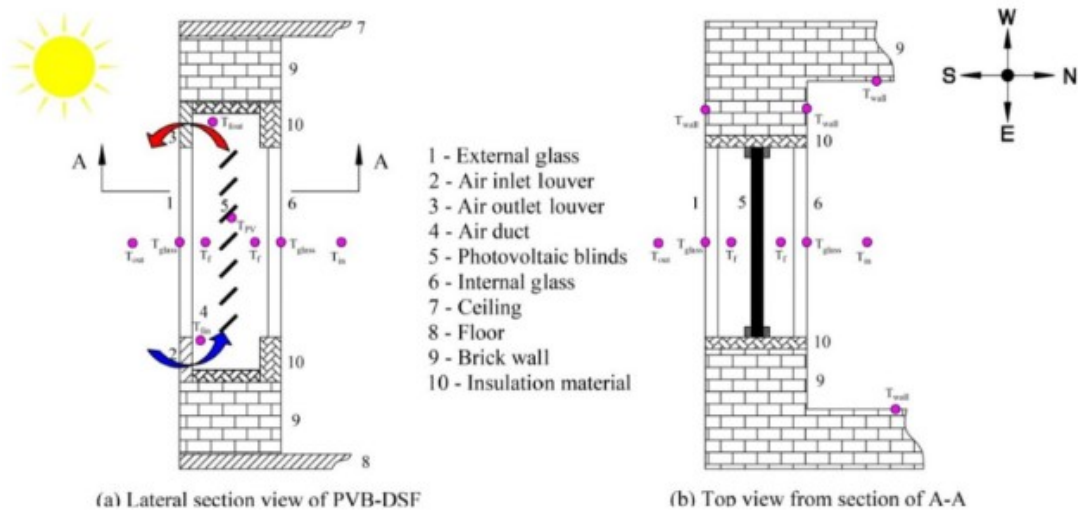


Figure 2.16: Drawing of PVB-DSF system (Luo, et al., 2018)

2.4 Smart Heat Pump Systems and Grid Flexibility

Heat pumps use a basic vapour compression cycle comprising of two heat exchangers, labelled as the evaporator and condenser, a compressor, and an expansion valve. The condenser is used as the heat sink where the heat pump discharges the high temperature gained from the compressor. The condenser is used to heat air or water for space heating or service hot water purposes in the heating cycle. The condenser replaces the evaporator in the cooling cycle, where heat is gained while cooling the water or air for conditioning the building. The evaporator has the reversed purpose of the condenser. In heating mode, the evaporator acts as the heat source. It gains heat from the low-temperature environment (either outdoors or supplied air from a solar collector/BIPV/T system or underground). In cooling mode, the evaporator acts as the condenser in the refrigerant cycle and releases the unnecessary heat gained into the outdoors, lake or sea water, or underground. The compressor takes in the low-temperature refrigerant from the evaporator (in heating mode) and compresses it into a higher temperature used in the condenser. The expansion valve then decompresses the refrigerant, lowering the temperature for the evaporator.

There are typically three commonly used heat pumps in buildings: air, water, and ground source. This study will focus on the use of air-source heat pumps. In conventional air source heat pumps, there is often insufficient heating provided to a building at low ambient temperatures (Sager, Mackintosh, St-Onge, McDonald, & Kegel, 2018). A cold climate air source heat pump can meet the required heating loads even at low ambient temperatures. Additionally, these heat pumps are typically variable capacity systems allowing the system to vary and increase the capacity outputted by the heat pump. An air-source heat pump generally has two types of distributors for the load side of the heat pump: air and water (air-to-air heat pump and air-to-water heat pump). The load side of the heat pump transfers energy to or from the source (either air or water in this case) for space heating/cooling or domestic hot water. This review will solely focus on the use of air-to-water heat pumps.

2.4.1 Smart Grid and Energy flexibility

A challenge for electric grids is the imbalance between the supply side and the demand side, especially with intermittent renewable energy sources (Yan, Xue, Wang, & Cui, 2015). A solution to this challenge is the implementation of a smart grid. A smart grid is defined as a self-healing, self-detecting, reliable, versatile, secure, and, most importantly, flexible two-way generation and

consumption (Sioshansi, 2011). Implementing a smart grid can help reduce the imbalance by controlling the power generation on the supply side and the power consumption on the demand side. The management of power systems for the demand side is classified as demand-side management (DSM). This strategy aims at reducing electricity consumption (energy efficiency) and peak loads (demand response) for an energy-efficient grid (Jabir, Teh, Ishak, & Abunima, 2018; Jordehi, 2019).

2.4.2 Demand Response

A subset of DSM is known as demand response (DR) which is defined as the changes in the demand side electricity usage in response to certain signals implemented by the end-user (either directly or indirectly) that differs from their normal consumption patterns (Yan, Xue, Wang, & Cui, 2015; Arteconi, Mugnini, & Polonara, 2019). Demand response is comprised of short-term strategies aimed to reduce the peak load by shifting the heating/cooling load to off-peak hours (load shifting and valley filling) or minimizing electricity demand by shutting off or reducing the capacity of high electricity consumers during peak periods (peak clipping) (Yan, Xue, Wang, & Cui, 2015). However, the reduction in peak loads and energy costs can increase electricity consumption and, in some cases, the loss of comfort. This can be seen from Lizana et al. (2018), who had successfully shifted the demand load to off-peak hours. This managed to reduce the overall cost but increased the electricity consumption. Additionally, Zhang et al. (2019) found that the use of upward and downward flexibility for an electrical heating system provided flexibility in the system at the cost of reduced energy payback and comfort loss for the application studied.

Demand response can be categorized as either incentive- or time-based strategies. The key incentive-based demand response includes the following approaches:

- **Demand Side Bidding (DSB) / Buyback (BB).** Consumers can offer to reduce the electricity consumption for periods of time for an incentive or identify the amount of load they are willing to reduce (Federal Energy Regulatory Commission, 2006).
- **Direct Load Control (DLC).** This strategy reduces the peak load by switching off or limiting the power used by appliances (e.g. heating systems) for periods of time (e.g. 15 minutes off during an hour) (Federal Energy Regulatory Commission, 2006).

- **Interruptible / Curtailable Load (I/C).** I/C program incentivizes the reduction in the consumer's load demand during peak periods when notified by the utility (Marwan & Kamel, 2011). The loads are diminished to pre-defined values (Shariatzadeh, Mandal, & Srivastava, 2015).

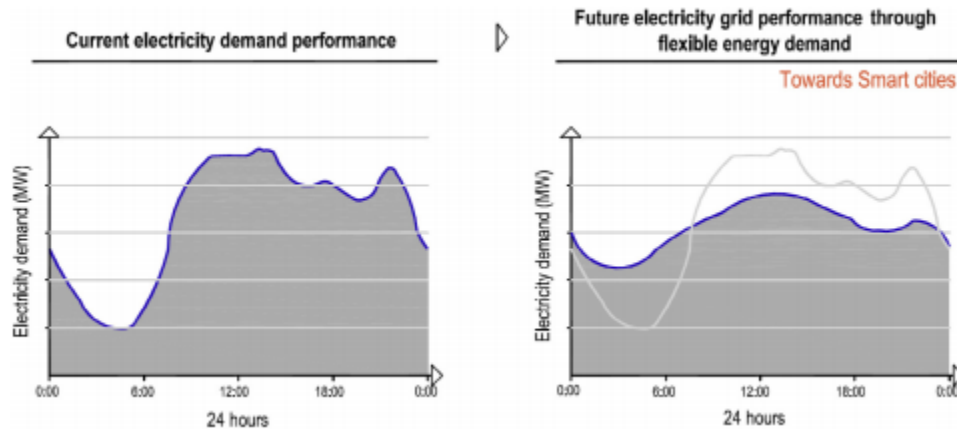


Figure 2.17: Reducing peak load demand through the use of flexible energy demand (Lizana, Friedrich, Renaldi, & Chacartegui, 2018)

The key time-based demand response includes the following approaches:

- **Time-of-Use (TOU).** This strategy is dictated by the daily energy and demand rates throughout the day for different periods of time (Federal Energy Regulatory Commission, 2006). Time-of-Use pricing commonly has two or three price rates, generally known as on-peak, off-peak, and an intermediate mid-peak (only in three-tiered TOU).
- **Real-Time Pricing (RTP).** This strategy reacts to changes in either real-time or day-ahead cost of power based on hourly changes in the market value price of power (Federal Energy Regulatory Commission, 2006; Marwan & Kamel, 2011).
- **Critical Peak Pricing (CPP).** CPP uses real-time prices (within either TOU or flat pricing) during periods of extreme pricing peaks. CPP occurs a few hours per year and has a higher than normal price peak. The timing of the critical periods is unknown ahead of time (Federal Energy Regulatory Commission, 2006).

The hierarchical structure of the demand side-management and demand response strategies can be seen in Figure 2.18.

2.4.3 Smart Heat Pumps

Within a smart grid, the heat pump is part of the demand side that can be controlled (Fischer & Madani, 2017). A smart heat pump can provide utility control for demand-side management (Fischer & Madani, 2017; Arteconi, Mugnini, & Polonara, 2019). Hot water storage is a method to achieve this as it effectively acts as a thermal battery for electricity generated (Facci, Krastev, Falcucci, & Ubertini, 2018; Thür, Calabrese, & Streicher, 2018). A study from Yan et al. (2015) implements demand-side bidding and demand as a controlled reserve to operate an air conditioning system with a storage tank. The day ahead demand-side bidding (DSB) is a type of load shifting that estimates the amount of energy to be delivered for the upcoming day, as shown in Figure 2.19. The frequency-controlled reserve (DFR) utilizes a similar approach as DSB but on an hourly basis. The hour-ahead methodology allows the air conditioning unit to change the power demand flexibly. The results showed that the DSB method increases the power load factor by 30%, while the DFR strategy could flexibly change by an increase of 20% or a decrease of 40% for this application. Combining these strategies reduced the energy cost by 30%; however, the electricity consumption increased by 2.6%.

Aside from the controls and communication between the heat pump, building, and power system, the essential considerations that influence the flexibility of the heat pump system are the following (Fischer & Madani, 2017):

- **Thermal demand.** The thermal demand determines how much energy can be shifted and the recovery time for the storage (time to fully charged storage or the discharge rate). This aspect will change depending on the location, building type, occupancy, and demand.
- **Heat pump capacity.** The capacity limits the possibility of shifting the heating/cooling load. If the heat pump capacity is equal to or smaller than the current heating demand, the most that can be achieved in terms of flexibility is reducing heat production. If the capacity exceeds the current demand, the heat pump capacity can be increased to charge the thermal storage. However, when the heat pump's heating capacity is reduced at lower temperatures, the flexibility possibility similarly decreases as heating demands increase.
- **Storage design.** The design of the thermal storage tank will determine the amount and duration of energy that can be stored. The capacity of the tank can determine the amount of

energy that can be shifted as the displacement of energy is determined by the tank’s charge and discharge rate.

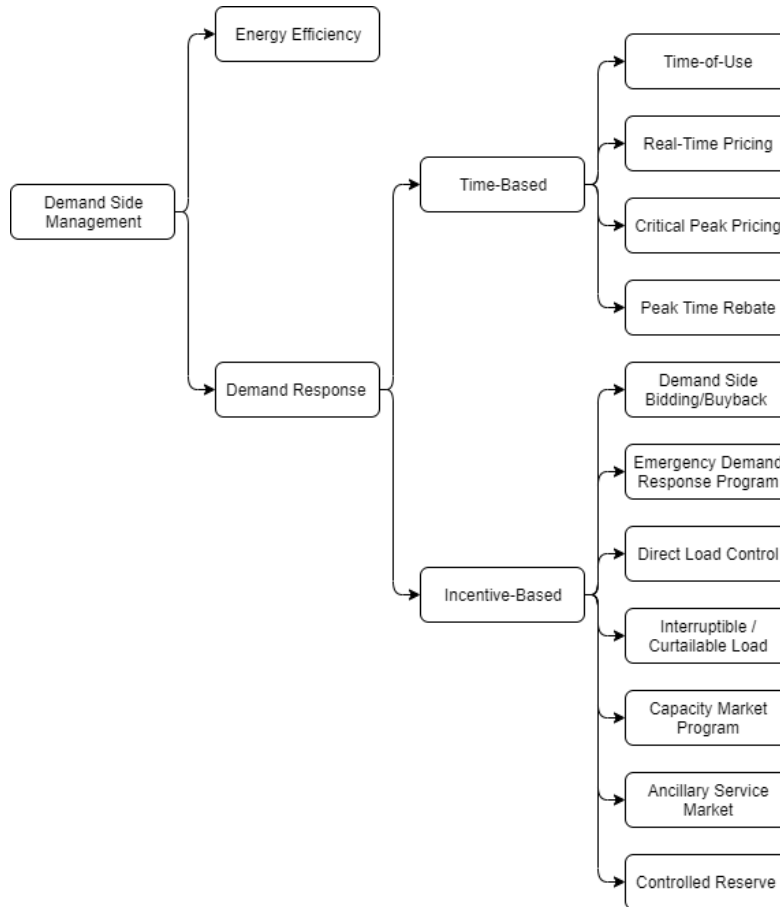


Figure 2.18: Classification of demand-side management and demand response (Shariatzadeh, Mandal, & Srivastava, 2015)

2.4.4 Storage Sizing

Energy storage systems can typically be classified as either electrical or thermal storage. Electrical storage is generally batteries (Jian, He, Jia, & Xie, 2013), while thermal storage commonly uses water tanks and radiant floors (Li, Joe, Hu, & Karava, 2015) or phase-change material (Bigaila & Athienitis, 2017). This study will focus solely on the impact of thermal storage for water tanks.

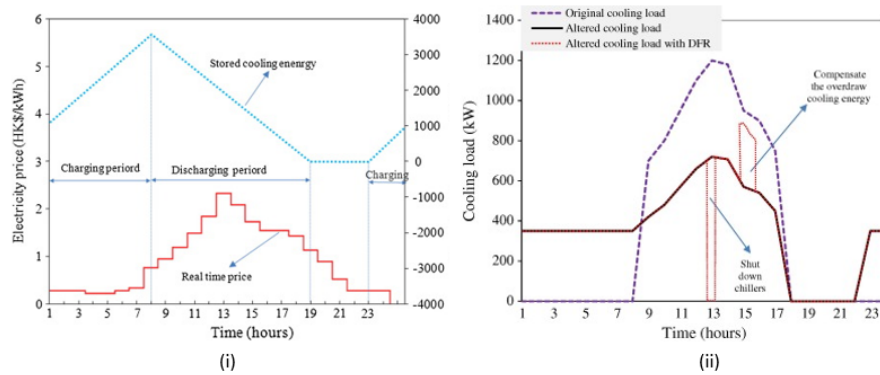


Figure 2.19: (i) Day-ahead demand-side bidding for day-ahead pricing and storage charging (ii) Building cooling load shifting using DBS and DFR strategies (Yan, Xue, Wang, & Cui, 2015)

The flexibility of a system, when considering thermal storage, depends on the amount of heat that can be stored in a water tank as well as the heat produced by the heating system (e.g. heat pumps), as seen in Figure 2.20 (Schuetz, et al., 2017). The increase in storage size and heat pump capacity substantially improve flexibility (Schuetz, et al., 2017). Schuetz et al. (2017) found that a larger heat pump size improves the system's flexibility while the size of the tank had little impact. Given that an increase in the tank and heat pump size will increase the system's flexibility, they recommended using a storage capacity of around 2 – 3 times the heat system's thermal output produced in one hour (Vandewalle, Keyaerts, & D'haeseleer, 2012). Nevertheless, the results and recommendations will differ depending on the region and demand response strategy used. Renaldi et al. (2017) conducted an analysis based on a time-of-use (TOU) pricing schedule. As expected, they found that the tank size depended on the pricing strategy used. Additionally, Allison et al. (2018) conducted a study to determine the storage size required to support daily peak shifting and heat storage utilizing four different residential buildings: detached (136 m²), semi-detached (87 m²), terraced (57 m²), and an apartment (56 m²). It was determined that utilizing water storage required a tank size between 0.3 – 1.9 m³ depending on the building type, occupancy level, and building insulation.

As noted, many studies have analyzed the use of demand response strategies in combination with heat pumps and thermal storage systems to shift or reduce the peak consumption of a heat pump and minimize the energy cost (Patteeuw, Henze, & Helsen, 2016; Zhang, Good, & Mancarella, 2019; Coninck, et al., 2010). Patteeuw et al. (2016) compared various demand response strategies,

including pricing-based time-of-use, load shifting, and load shaping, to control residential heat pumps in a large-scale community of buildings. It was found that the cost savings were between 1 – 5 % based on the number of buildings considered and the amount of renewable energy sources shared. Coninck et al. (2010) investigated the total energy efficiency and grid impact when utilizing demand response strategies in a typical Belgium residential building with an air-to-water heat pump and thermal storage system. They demonstrated that daytime charging and peak power reduction strategies substantially reduced the peak power consumption but had minimal energy savings (~4%).

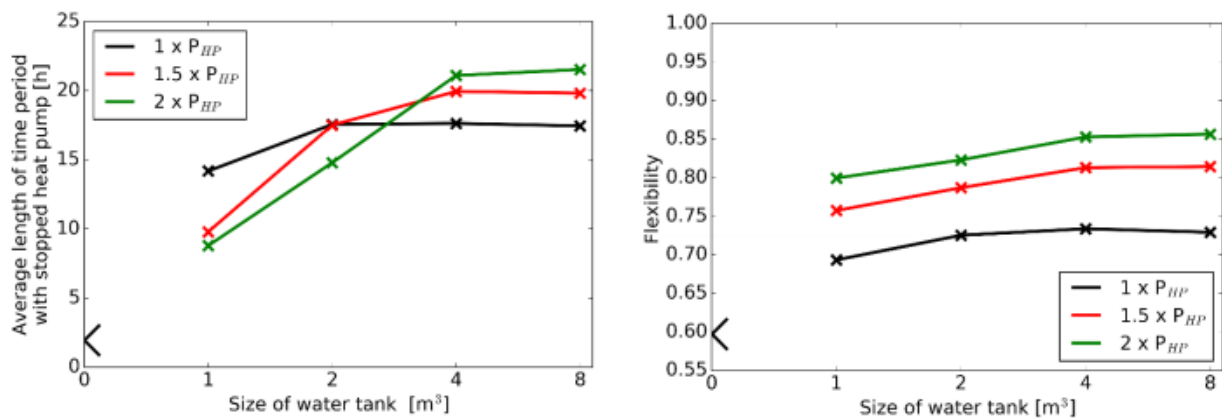


Figure 2.20: Average length of the time periods with a stopped heat pump calculated for a residential heating system (left) Dependence of flexibility on the heat pump power (P_{HP}) and the capacity of the tank (right) (Schuetz, et al., 2017)

2.5 Research Gaps

Based on the literature review conducted, the main findings and gaps identified are summarized as follows:

- To the authors' knowledge, no known studies consider the possibility of placing a heat pump within a zone that receives high amounts of solar radiation, such as a greenhouse or solarium. This includes a thorough assessment of the energy performance and the application of control strategies and demand response techniques to optimize the operation.
- Few studies indicate a typical component size based on the configuration and demand response technique, particularly with other systems, such as a heat pump with thermal

storage. This work would include determining the optimal value of key components within a system, such as tank volume, BIPV size, heat pump capacity, flow rate, etc., for different control methods.

- Further research needs to be completed to analyze BIPV and BIPV/T systems and compare different applications for the technology. Few studies utilize BIPV, BIPV/T, and STPV in combination with an air-source heat pump, and even fewer studies implement control strategies to assess the flexibility of these systems.

Chapter 3. System Modelling and Experimental Setup

3.1 Simulation Methodology

Three different configurations were analyzed: 1) BIPV and HPWH (reference), 2) Ducted BIPV/T-HPWH, and 3) Passive solar (STPV-HPWH). The schematics of each studied configuration are shown in Figure 3.1. It should be noted that each configuration transfers heat from different sources (outside air directly, BIPV/T outlet, or solarium) to heat the solarium when needed; however, the heat can be utilized in other the main house instead.

Configuration 1 uses an independent operation of BIPV and HPWH, meaning there is no direct interaction between the two systems and no solar heat. This system serves as a reference to compare alternate configurations as this is one of the most common PV installations. The heat pump will not receive an increased supply temperature and will serve as the system's baseline performance. However, the advantage of this system is the simple design, and it does not produce noise that may disturb the occupants.

The ducted BIPV/T-HPWH system (configuration 2) directly supplies solar-heated air from the outlet of the BIPV/T to the inlet of the HPWH (Figure 3.1 ii). This configuration has proven to increase the inlet temperature of the heat pump and increase the COP and improve the BIPV energy generation from ventilation (Dumoulin, 2019). This is a typical application of the thermal recovery from BIPV combined with heat pumps and will compare configurations that utilize heated air to improve heat pump performance.

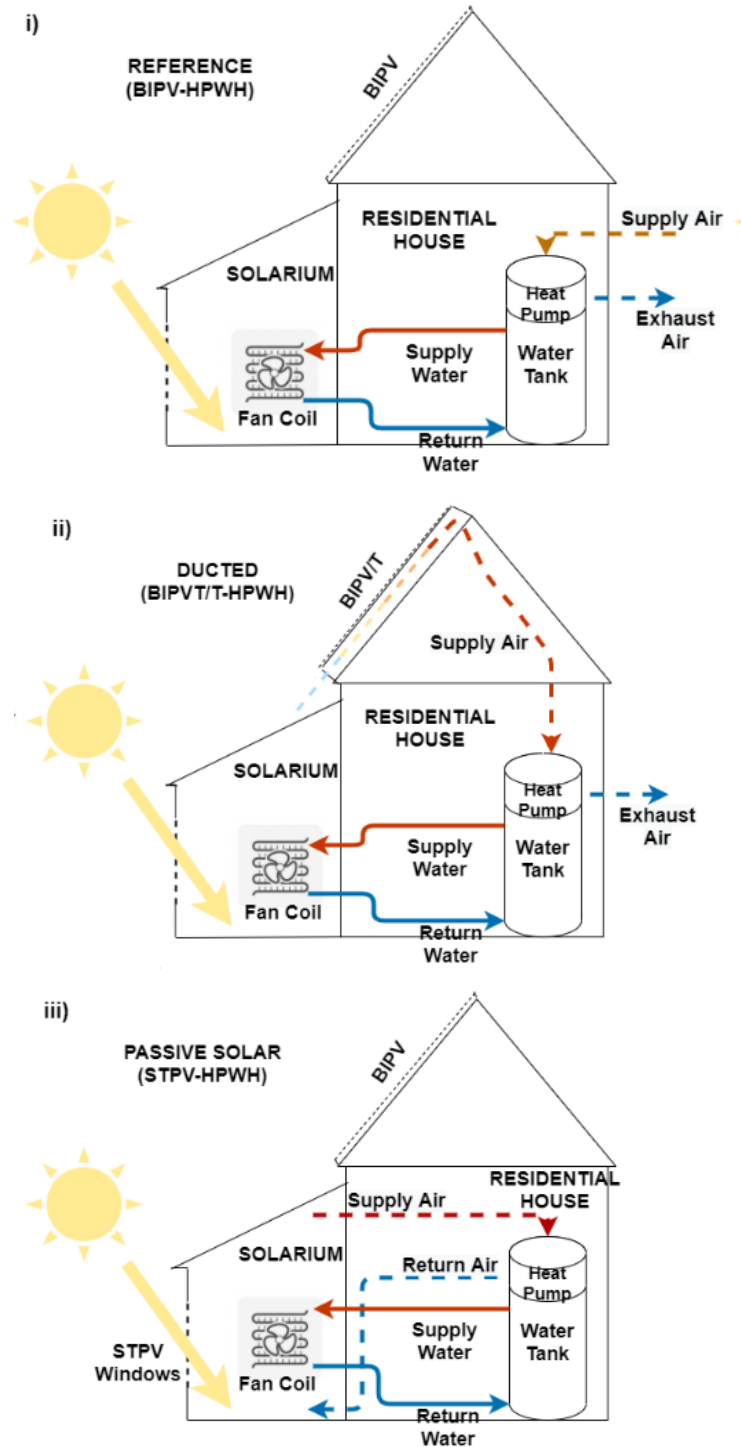


Figure 3.1: Schematic of i) reference (BIPV-HPWH) ii) ducted BIPV/T-HPWH system, iii) a passive solar design

The passive solar system (configuration 3) utilizes an attached solarium with STPV windows, typically used as a greenhouse or sunroom, to house the heat pump, providing a warm environment

for the unit (Figure 3.1 iii). This configuration is ideal for an existing solarium within the home or retrofit options to use the opportunity to enclose the heat pump as well. The system uses semi-transparent photovoltaics (STPV) on the façade of the solarium instead of an opaque BIPV/T system on the house roof. The ideal operation of this configuration is to utilize and transfer the solar-heated air from the solarium on a sunny day to heat a room at night using a water tank to transfer the heat. This configuration has a simpler design than the ducted solution while improving the heat pump's performance during the winter for either space-heating or domestic hot water applications. If this system is utilized year-round, it benefits from cooling the zone during the summer while producing hot water for domestic hot water applications.

The following sub-sections detail the mathematical models of each key component developed in MATLAB 2020a, Simulink, and Python 3.8. The sub-sections also define the analysis approach used for two analyses: energy performance comparison of alternate BIPV-HPWH configurations and sizing key components within the system based on power reduction and the building energy flexibility index.

3.1.1 Model Description

This section describes the mathematical model developed for each key component in the simulation, including the building, heat pump, thermal storage, and BIPV models — additional calculations for the key components are provided in Appendix C.

3.1.1.1 Weather model

Weather data was extracted from a typical meteorological source for Canada used by software such as Energy Plus and TRNSYS. Specifically, CWEC was used for the Montreal Jean Breneuf weather station. However, this weather data provides the horizontal radiation; thus, the Perez Weather model described by Duffie and Beckman (2003) was used.

3.1.1.2 Building model

This thesis analyzes a typical single-family home with a total floor area of 116 m², split into 22.5 m² for the south-facing solarium and 93.5 m² for the main building in Montreal. The thermal network used to model the building is shown in Figure 3.2. The building envelope was assumed to follow NBC standards for Montreal's climate (National Research Council of Canada, 2015). This includes heating setpoints, occupancy, and internal gain schedules. The building model was

created in Simulink using a 4th order resistance-capacitance (RC) network modelling the main house and a separate zone for the solarium calculated based on a state-space representation formulation.

The house utilizes a baseboard heater to maintain the building temperature. The south-facing solarium is heated from incoming solar irradiation during the day, and heat is transferred from a charged HPWH through a fan coil unit to maintain a temperature between 5 °C and 25 °C to ensure some basic thermal conditions for the occupant should they occupy the space or if plants are being grown. A baseboard heater is added to the solarium to ensure the room is kept at a minimum temperature. Motorized shades are used to limit solar gains should the temperature of the space reach 25 °C. The calculation of motorized shades is included in the overall heat transfer coefficient between the solarium, the outdoors, and the solar irradiation transmitted into the room (Yang & Rhee, 2013).

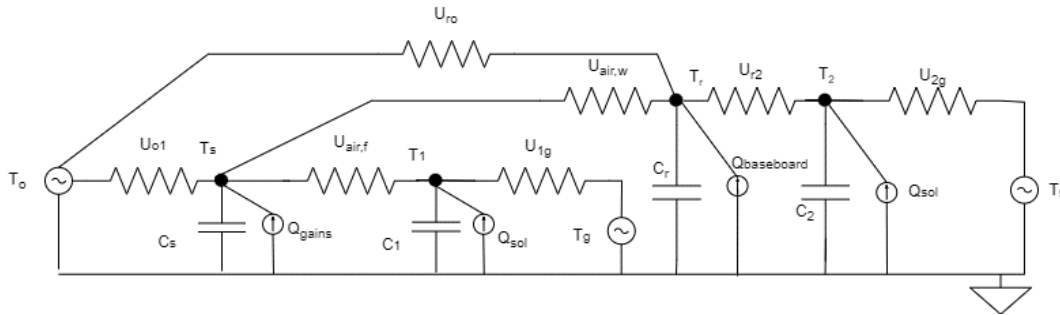


Figure 3.2: Building thermal network

Solarium:

$$C_s \frac{dT_s}{\Delta t} = (U_{o1}A_{o1} + U_{inf,s}A_{inf,s})(T_o - T_s) + U_{air,f}A_{air,f}(T_1 - T_s) + U_{air,w}A_{air,w}(T_r - T_s) + Q_{gains} \quad (3.1)$$

$$C_1 \frac{dT_1}{\Delta t} = U_{1g}A_{1g}(T_g - T_1) + U_{air,f}A_{air,f}(T_s - T_1) + Q_{sol} \quad (3.2)$$

House:

$$C_r \frac{dT_r}{\Delta t} = (U_{ro}A_{ro} + U_{inf,r}A_{inf,r})(T_o - T_r) + U_{r2}A_{r2}(T_2 - T_r) + U_{air,w}A_{air,w}(T_s - T_r) + Q_{baseboard} + Q_{gains} \quad (3.3)$$

$$C_2 \frac{dT_2}{\Delta t} = U_{2g}A_{2g}(T_g - T_2) + U_{r2}A_{r2}(T_r - T_2) + Q_{sol} \quad (3.4)$$

Where C_s and C_r are the air capacitances of the solarium and house, respectively, in J/K. C_1 and C_2 are the capacitances of the floors in the solarium and house, respectively, in J/K. $U_{o1}A_{o1}$, $U_{air,f}A_{air,f}$, and $U_{air,w}A_{air,w}$ are the overall heat transfer coefficients between the solarium and the outdoors, solarium floor, and house, respectively, in W/K. $U_{ro}A_{o1}$, and $U_{r2}A_{w2}$ are the overall heat transfer coefficients between the house and the outdoors as well as the house floor, respectively, in W/K. $U_{1g}A_{1g}$ and $U_{2g}A_{2g}$ are the overall heat transfer coefficients between the ground and the solarium floor and the house floor, respectively, in W/K. $U_{inf}A_{inf}$ is the infiltration into either the solarium or the house in W/K. T_o , T_s , T_1 , T_r , T_2 , and T_g are the outdoor, solarium air, solarium floor, house air, house floor, and ground temperatures, respectively, in °C. $Q_{baseboard}$ is the heat gained into the house from the baseboard heaters in W. Q_{sol} is the solar radiation absorbed by the floor in W and Q_{gains} is the internal gains added to the space from occupants, lighting, fan coil (in the solarium), and the heat gained/lost from the heat pump for configuration 3 in W.

Table 3.1: Key building parameters

Parameter	Value
Solarium volume (m ³)	68.5
Solarium floor area (m ²)	22.5
House floor area (m ²)	93.5
South facing window area – Solarium (m ²)	10
East window-to-wall ratio (-)	0.2
North window-to-wall ratio (-)	0.1
West window-to-wall ratio (-)	0.2

3.1.1.3 Heat pump model

The heat pump water heater used within this analysis was modelled in Python based on a steady-state first principles model of the Rheem's Professional Prestige Proterra Hybrid Electric Heat Pump Water Heater (CPROPH50 T2 RH375-30). The Rheem unit is a compact heat pump ideal for use combined with a ducted BIPV/T system due to a low required source airflow rate of around 100 CFM (Larson, Logston, & Baylon, 2011). In addition, it has a moderate sound level of 49 DB. The Rheem unit provides the option to be easily installed as a ducted or un-ducted system, fitting for any practical application.

The Rheem Hybrid Electrical Heat Pump Water Heater has five modes of operation, including heat pump only, electric only, energy saver, high demand, and vacation modes. This analysis solely utilizes the heat pump only mode and operates the electric elements only if necessary. The heat pump uses R134a as the refrigerant and has a rated COP of 3.75. The heat pump has a cut-off temperature of 2.5 °C. The water heater will be in electrical mode only below the cut-off temperature in configurations that use outdoor air (reference configuration and ducted BIPV/T). Key parameters for the heat pump are listed in Table 3.2.

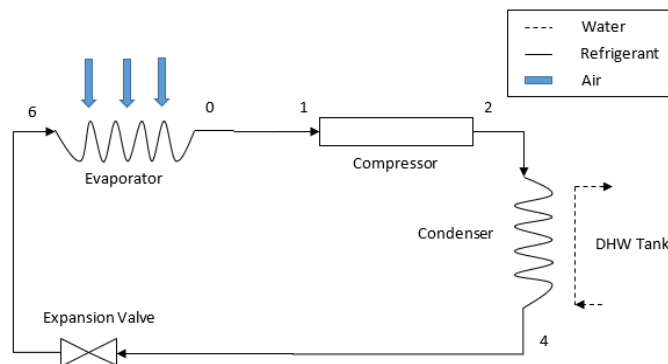


Figure 3.3: Heat pump refrigerant diagram

Table 3.2: Key heat pump specifications

Parameter	Value
Refrigerant	R134a
COP (-)	3.75
Flow rate (CFM)	100

Cut-off temperature (°C)	2.5
Electrical element wattage (kW)	4
Tank volume (L)	170
Maximum water temperature (°C)	65

3.1.1.4 Thermal storage model.

The thermal storage is modelled using a simplified RC network. The equations utilized for the storage tank were derived from an energy balance of the given system similar to studies from Rahman et al. (2015), Abdelsalam et al. (2019), Saloux and Candanedo (2018), Nash et al. (2017), Cruickshank (2009), and TRNSYS (2017) and validated using Type 534 from the TESS library within TRNSYS. The storage tank has a volume of 170 L and is split into eight sections. This component is modelled using state-space representation.

The tank has one inlet and outlet with a wrap-around heat exchanger coil transferring energy from the heat pump to the tank. The inlets are utilized for the heat pump and fan coil. The heat exchanger supplies heat to the building through a fan coil unit. The following assumptions were made to create the model:

- The fluids were considered incompressible
- Uniform temperature within each node
- Thermal properties of water are constant
- Fluid streams are fully mixed within each node before flowing into the next node
- 1-dimensional model
- Buoyancy is modelled using inversion mixing

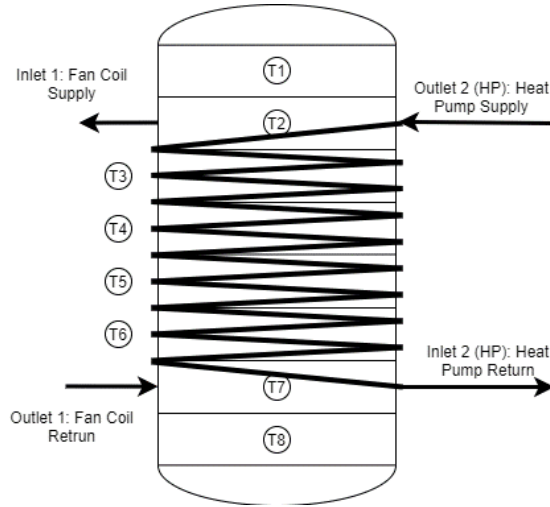


Figure 3.4: Modelled thermal storage

The thermal storage tank considers three tank sections: the top, middle, and bottom, as seen in Figure 3.5.

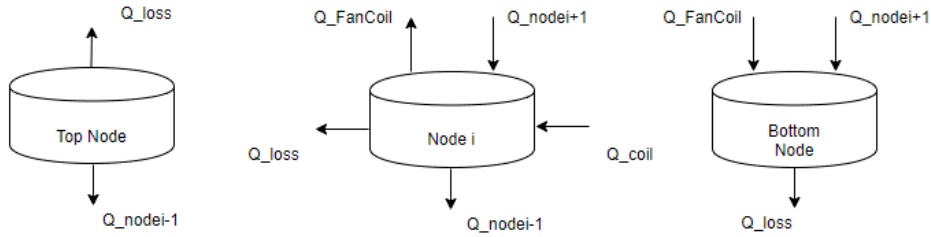


Figure 3.5: Energy balance per tank node

Additionally, inversion mixing is enabled for this component. Inversion mixing is calculated within the heat transfer equation when a lower node has a higher temperature than an above node and mixes the two affected nodes until they are the same temperature. This is done to model buoyancy effects within the tank. An energy balance was taken for these eight zones and the immersed heat exchanger coils. They are as follows:

Bottom Node:

$$\begin{aligned}
 C_8 \frac{dT_8}{\Delta t} = & \frac{k_w A_8}{L_8} (T_7 - T_8) + m_{FC} c_p (T_7 - T_8) + m_{FC} c_p (T_{FC} - T_1) \\
 & + U_{loss} A_{loss} (T_{sur} - T_8) + m_{mix} c_p (T_7 - T_8)
 \end{aligned} \tag{3.5}$$

Middle Nodes:

$$\begin{aligned} C_i \frac{dT_i}{\Delta t} = & \frac{k_w A_i}{L_i} (T_{i-1} - T_i) + \frac{k_w A_i}{L_i} (T_{i+1} - T_i) + m_{FC} c_p (T_{i-1} - T_i) \\ & + U_{loss} A_{loss} (T_{sur} - T_i) + U_{coil} A_{coil} (T_{coil,in} - T_i) \\ & + m_{FC} c_p (T_{i+1} - T_i) + m_{mix} c_p (T_{i+1} - T_i) + m_{mix} c_p (T_{i-1} - T_i) \end{aligned} \quad (3.6)$$

Top Node:

$$C_1 \frac{dT_1}{\Delta t} = \frac{k_w A_1}{L_1} (T_2 - T_1) + U_{loss} A_{loss} (T_{sur} - T_1) + m_{mix} c_p (T_2 - T_1) \quad (3.7)$$

Heat Exchanger Coils:

$$C_{coil} \frac{dT_{coil,o}}{\Delta t} = m_{coil} c (T_{coil,out} - T_{coil,in}) + U_{coil} A_{coil} (T_i - T_{coil,out}) \quad (3.8)$$

Where C_1 , C_i , C_8 are the tank capacitances in J/K, C_{coil} is the coil capacitance in J/K. k_w is the thermal conductance of the water in W/(m·K), A_i is the area of nodes in m², L_i is the heights of nodes in m. m_{FC} and m_{mix} are the mass flow rates from the fan coil and inversion mixing between nodes in kg/h. c_p is the specific heat capacity of the water in kJ/(kg·K), $U_{loss} A_{loss}$ is the overall heat transfer coefficient lost to the environment in W/K, and $U_{coil} A_{coil}$ is the overall heat transfer coefficient of the coil in W/K. T_1 , T_i , and T_8 are the average node temperatures in °C. T_{sur} is the environment temperature, T_{FC} is the water temperature returned from the fan coil all n °C. Finally, $T_{coil,out}$ and $T_{coil,in}$ are the output and input temperatures from the coil in °C.

3.1.1.5 BIPV/T and STPV models

The BIPV/T model is utilized solely for the ducted configuration, while the STPV is used with the passive solar design as STPV windows on the façade. Each configuration has a 5 kW PV system to achieve a similar energy generation. Configuration 1 has opaque BIPV on the roof of the building, while configuration 3 has STPV windows on the façade with additional opaque BIPV on the roof to generate 5 kW in total. STPV and BIPV array size depends on the STPV panels' transparency within the parametric analysis.

The BIPV/T model was developed in MATLAB for an unglazed BIPV/T air system. As defined for this analysis, an unglazed system refers to a BIPV/T collector with a single layer of glass covering the PV cells (University of Wisconsin, 2017). The BIPV/T model developed was based on the thermal resistance network for opaque BIPV/T seen in Figure 3.6 and used a similar thermal network and methodology as Delisle (2015) and Rounis (2018). The specifications of the system are given in Table 3.3.

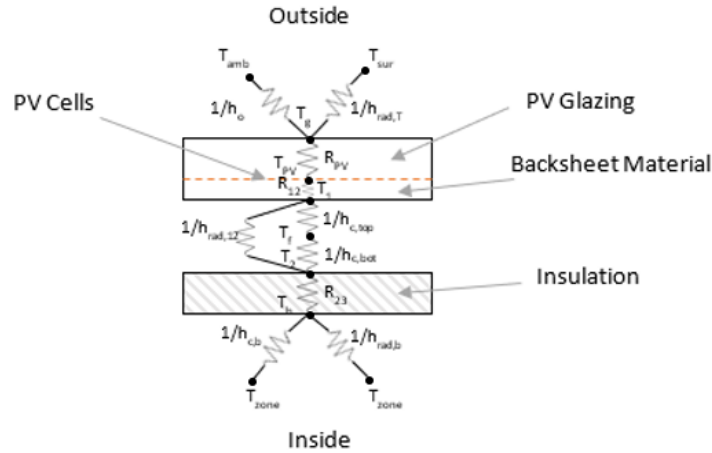


Figure 3.6: BIPVT thermal resistance network

Table 3.3: BIPVT specifications

Parameter	Value
BIPV/T area (m ²)	35
Channel depth (m)	0.04
Flow rate (CFM)	100
Packing factor (-)	0.9
Slope (°)	45
Efficiency (%)	15

The energy balance performed on the different BIPV/T layers gives the following relations:

PV glazing layer:

$$0 = h_o(T_g - T_{amb}) + h_{rad,t}(T_g - T_{sur}) + \frac{T_g - T_{PV}}{R_{PV}} \quad (3.9)$$

PV Cells:

$$\frac{S_{PV}}{WL_{CV}} + \frac{T_g - T_{PV}}{R_{PV}} = \frac{T_{PV} - T_1}{R_{12}} \quad (3.10)$$

Air channel top surface:

$$\frac{T_{PV} - T_1}{R_{12}} + \frac{S_{ins}}{WL_{CV}} = h_{c,top}(T_1 - T_f) + h_{rad,12}(T_1 - T_2) \quad (3.11)$$

Air channel:

$$Q_{th} = h_{c,top}(T_1 - T_f)WL_{CV} - h_{c,bot}(T_f - T_2)WL_{CV} \quad (3.12)$$

Air channel bottom surface:

$$h_{c,bot}(T_f - T_2) + h_{rad,12}(T_1 - T_2) = \frac{T_2 - T_b}{R_{23}} + \frac{T_g - T_{PV}}{R_{PV}} + \frac{T_{PV} - T_1}{R_{12}} \quad (3.13)$$

Insulation:

$$\frac{T_2 - T_b}{R_{23}} - h_{c,b}(T_b - T_{zone}) - h_{rad,b}(T_b - T_{zone}) = 0 \quad (3.14)$$

As no thermal recovery is considered for the STPV model, the solarium window transparency and the electricity generation are the sole aspects calculated for this model. The electricity is calculated using a simple formula that relates the incoming solar irradiation to the STPV efficiency and packing factor. Simultaneously, the remaining irradiation (not absorbed or reflected by the STPV cells) is transmitted to the room. The reference transparency of the system is 50 %.

3.1.2 Analysis Approach

This study conducted two analyses based on the energy use and the flexibility performance of the different configurations described in section 3.1.1. The energy use is evaluated for the heating season with no optimization or demand response technique to define the reference case. The flexibility performance is analyzed for the following demand response strategies 1) Daytime Charging, 2) Critical Event Pricing (with a 4-hour charging period), and 3) Time-of-Use pricing. A parametric analysis is performed to evaluate the flexibility performance to determine the

parametric influence and optimal parametric values for each demand response strategy and configuration.

3.1.2.1 Energy analysis

This analysis studies the electricity consumption throughout the heating season for the heat pump, auxiliary heating system in the tank, baseboard heating in the solarium, as well as BIPV and STPV production. The energy analysis was conducted using a daytime charging strategy to maximize the system's benefits. The water tank is charged during a sunny day when the irradiation incident on the solarium is above 300 W/m^2 . The stored energy is released at night to heat the solarium and maintain the room temperature, but it could be used for other parts of the house. The tank is charged to $65 \text{ }^\circ\text{C}$ during the day (when solar irradiance is available) and discharged at night with a minimum setpoint temperature of $45 \text{ }^\circ\text{C}$.

3.1.2.2 Demand response strategies

Daytime charging (Figure 3.7ii) is a strategy used particularly with storage systems and renewables, as it requires storing thermal or electrical energy when produced by a renewable source. In the case of this analysis, the water tank will store thermal energy by increasing the water temperature setpoint only when the solar irradiation is above a threshold of 300 W/m^2 when the solarium temperature begins to rise due to solar heat gains. On a typical cold winter day, the solarium reaches $10 - 15 \text{ }^\circ\text{C}$ before reaching the solar radiation threshold.

Critical event pricing (Figure 3.7iii) is a real-time pricing strategy that significantly increases the price per kWh during critical events. It occurs for a few hours per year, and the peak periods' timing is unknown ahead of time (Federal Energy Regulatory Commission, 2006). The critical event periods are scheduled at fixed intervals to simplify the simulation of the unknown peak periods during the winter season. These events occur from 6:00 am to 9:00 am and 4:00 pm to 8:00 pm, as Quebec's utility provider, Hydro Quebec, specifies. The tank is charged 4 hours before the events based on the assumption that the system will receive a 4-hour notice before any critical period.

A time-of-use pricing structure (Figure 3.7iv) is typically a 3-tiered tariff. This analysis uses the pricing structure effective November 2019 from Hydro Ontario (2020). All other strategies use the Rate D (daytime charging) and Flex Rate D (critical event pricing) utility structures from Hydro Quebec (2019).

However, within all configurations, the tank will be charged to 65 °C during non-critical periods (i.e. during the day for daytime charging and 4 hours before an event for critical event pricing) and set back to 45 °C during critical events. The reference control strategy (Figure 3.7i) does not utilize any demand response strategy for controls to compare the effect of different control strategies on flexibility, and the water setpoint remains constant at 55 °C.

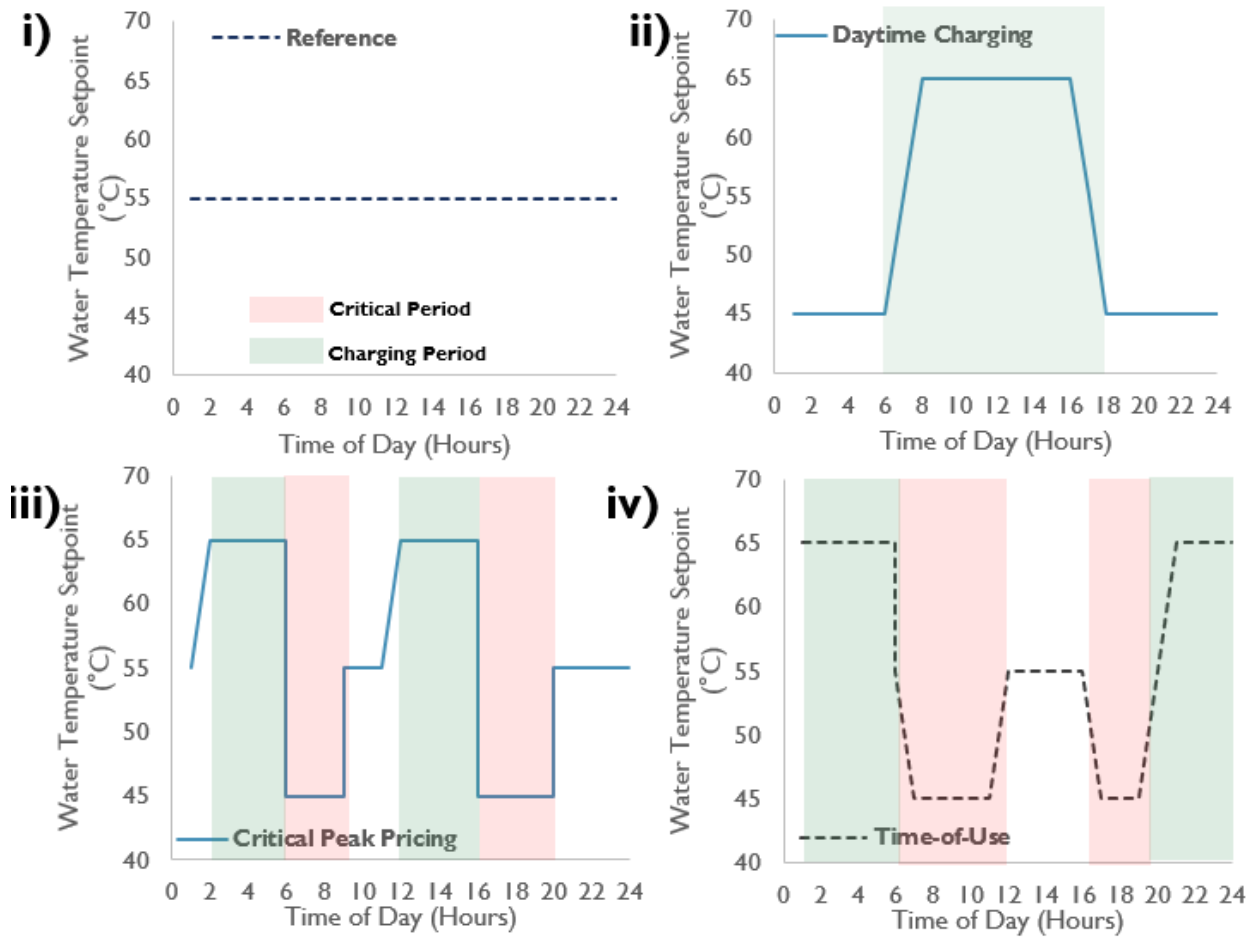


Figure 3.7: Control strategies i) Reference, ii) Daytime charging, iii) Critical Peak Pricing, and iv) Time-of-Use

3.1.2.3 Parametric analysis

A parametric analysis was conducted using Simulink's Sensitivity Analyzer Application. The parameters selected are: 1) Tank volume, 2) Relative heat pump size, 3) STPV packing factor (Figure 3.8), and 4) Relative solarium building size (Figure 3.9). Considerations for sizing each system include:

- A single tank is used for this system regardless of the size, while the tank height is calculated using a constant diameter.
- The relative solarium size is only used to scale the solarium's dimensions.
- The heat pump size scales the power consumption, capacity, and mass flow rate of the system, and the temperature output remains unchanged.
- The packing factor is only assessed for configuration 3 (passive solar).
- The STPV window electrical output does not change with the solarium size.
- The STPV window size varies with the packing factor to maintain a constant 5 kW array.

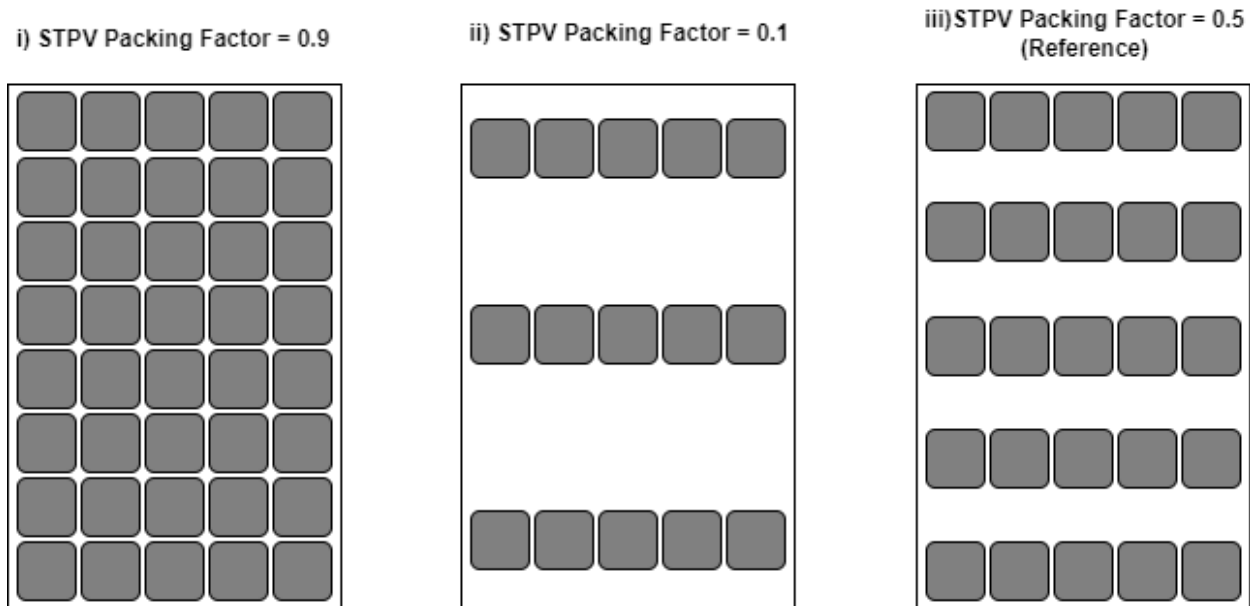


Figure 3.8: Parametric STPV packing factor bounds i) Upper bound at 0.9, ii) Lower bound at 0.1, and iii) Reference at 0.5

With a sample size of 30 data points, the analysis randomly generates values for each parameter selected (tank volume, heat pump size, solarium size, and packing factor) within a set range of upper and lower bound values (Table 3.4). i.e. for the tank volume, 30 values were chosen between 100 L (lower bound) and 1500 L (upper bound), inclusively, as the parameters used for the analysis. For each of these runs, the output is the average BEFI for all peak periods within the simulation runtime (ex., for daytime charging, the BEFI is only calculated at night). The control

strategies used are defined in section 3.1.2.2. They are fixed schedules that vary the water setpoint temperature and are not changed for each run.

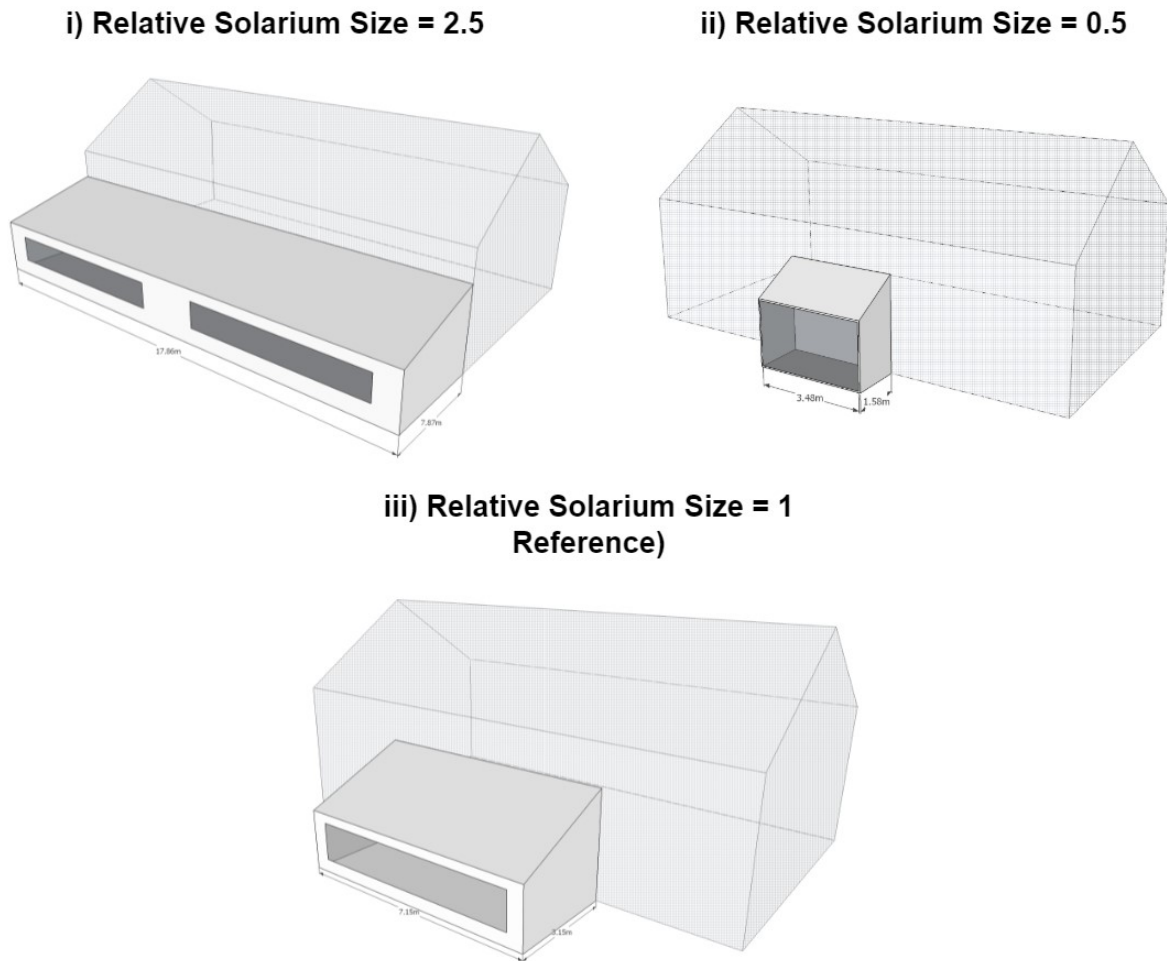


Figure 3.9: Parametric relative solarium size bounds i) Upper bound at 2.5, ii) Lower bound at 0.5, and iii) Reference at 1

Table 3.4: Parametric analysis specifications

Parameter	Reference Value	Lower Bound	Upper Bound
Tank volume (L)	170	100	1500
Relative heat pump size (-)	1	0.5	2.5
Relative solarium building size (-)	1	0.5	2.5
Packing factor for STPV (-)	0.5	0.1	0.9

The Sensitivity Analyzer calculates the average BEFI (the specified output property) for the entire 3-month simulation runtime (January, February, and March). The average BEFI during a peak event is calculated using equation (3.15) (Athienitis, Dumont, Morovat, Lavigne, & Date, 2020).

$$\overline{BEFI}(t, \Delta t) = \frac{\int_t^{t+\Delta t} P_{flex} dt - \int_t^{t+\Delta t} P_{ref} dt}{\Delta t} \quad (3.15)$$

where Δt is the duration of the flexibility event, t is the start time of the event, P_{ref} and P_{flex} are the power consumed during the reference case and utilizing a demand response strategy, respectively. To generalize and compare the BEFI between scenarios, the BEFI is expressed as the percentage change in power compared with the reference scenario, as seen in equation (3.16).

$$BEFI = \frac{\overline{BEFI}(t, \Delta t)}{\int_t^{t+\Delta t} P_{ref} dt} * 100\% \quad (3.16)$$

The output requirement or evaluation criteria for the output signal is to minimize the mean BEFI. The BEFI reference configuration does not use any added control strategies. This means that the P_{ref} in equation (3.15) refers to a scenario without any demand response controls. The parametric analysis input range and reference configuration values can be found in Table 3.4.

Two different analyses were conducted: 1) Parametric influence and 2) One-at-a-time parametric analysis. The first parametric analysis calculates the statistical representation of the parametric influence on the average BEFI of the system utilizing a combination of the selected parameters to study the impact on the average BEFI. This statistical analysis was conducted through the Sensitivity Analyzer in MATLAB using a linear correlation methodology and normalized based on the results. The one-at-a-time analysis compared the average BEFI when changing a single parameter to identify the optimal parametric values for each configuration and demand response strategy.

3.2 Results

In this section, the developed mathematical model is utilized to analyze and compare the heating season electricity consumption for the reference (BIPV-HPWH), ducted (BIPV/T-HPWH), and passive solar (STPV-HPWH) configurations. The same model is utilized to determine the parametric influence and optimal parameter values for the tank volume, heat pump size, solarium building size, and packing factor based on different demand response strategies, including daytime charging, critical peak pricing, and time-of-use.

3.2.1 Heating Season Electricity Consumption

Figure 3.10 shows the electricity consumed by the heat pump water heater, auxiliary elements within the tank and solarium (including the baseboard heaters in the solarium), and the energy generated by the PV throughout the heating season. The energy analysis of the main house will be included within another study as this analysis will focus on the displacement of solar heat gain into the solarium, with little interaction with the main house through a well-insulated wall. The house electricity consumption has minimal differences (<1%) between configurations.

Each scenario considers only the mechanical system utilized to maintain the solarium room temperature. Configuration 1 (reference) shows the highest electricity consumption, while the passive solar configuration has the lowest. This is due to the increased temperature supplied to the heat pump. The increased environmental temperature in configuration 3 extends the operating limits for the HPWH and improves the COP of the system. Configuration 3 is the only

configuration where the heat pump is located indoors; in all other configurations, the heat pump uses supply air from outdoors.

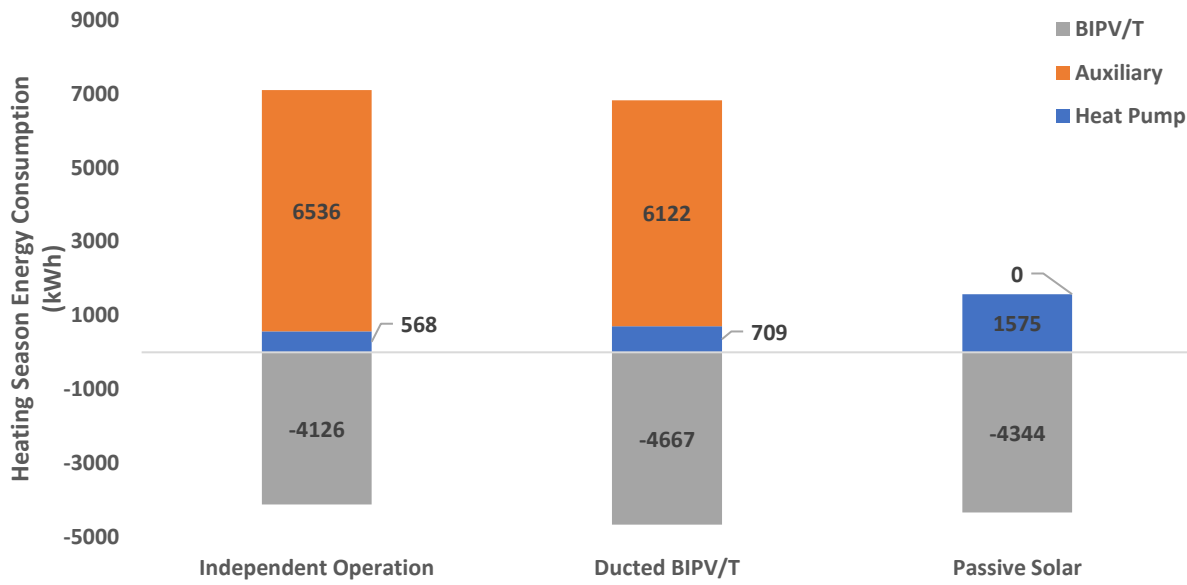


Figure 3.10: Mechanical system electricity consumption during the heating season

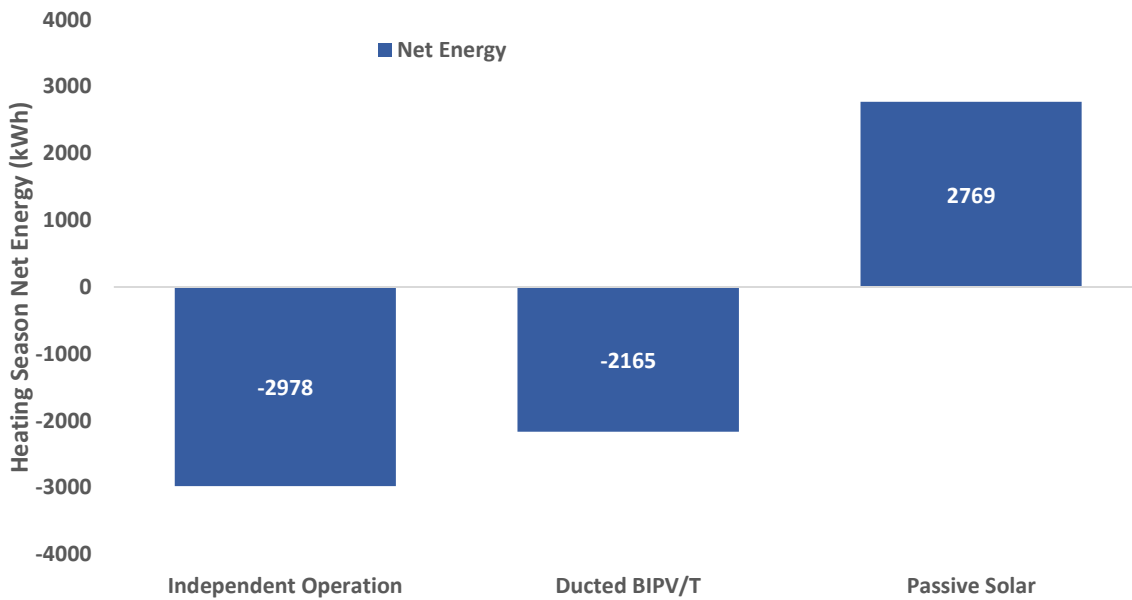


Figure 3.11: Mechanical system net energy used during the heating season

Consequently, the HPWH is in electric-only mode for a significant portion of the winter due to the cut-off temperature (2.5 °C). Thus, there is a considerable increase in power consumption from the auxiliary element usage. This effect can be seen in Figure 3.12, where the auxiliary element runs much of the day with higher power consumption for configuration 2. As the mean temperature is below -10 °C, the BIPV/T outlet in configuration 2 could not reach above the heat pump's cut-off temperature while matching the heat pump's required flow rate. In contrast, configuration 3 shows the heat pump running at a lower power consumption of 1 kW. It should be noted that during the entire heating season in configuration 3, the solarium is kept above 5 °C heated entirely by the HPWH with no use of the auxiliary elements in the water tank or solarium.

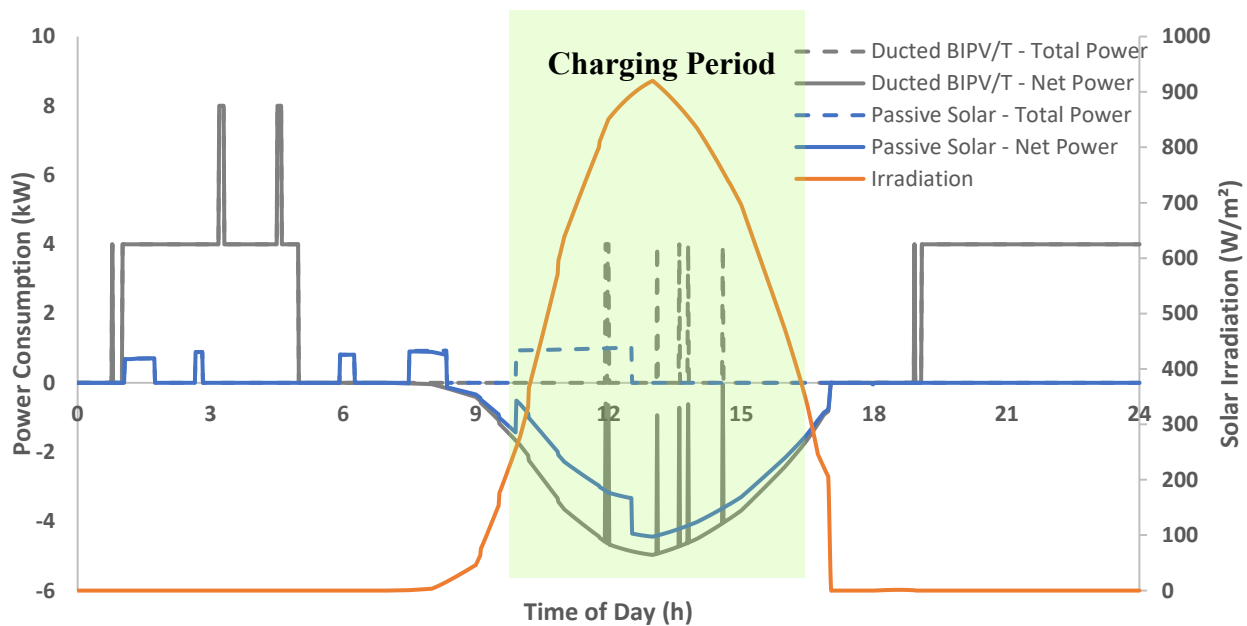


Figure 3.12: Power consumption on a typical cold sunny day on February 10th with a daily average temperature of -13 °C

Configuration 3 is not commonly seen; however, this system has the potential to yield improved performance compared to the other configurations (~80% compared to the reference case) due to a higher temperature environment for the heat pump heated by solar irradiation. In addition, a solarium tends to overheat, even throughout the winter, and the inclusion of the heat pump within the solarium will benefit from cooling the space when it is operating. However, the heat pump's

noise level should be considered, as a high noise level will disturb occupants within the solarium. The heat pump chosen has a moderate to quiet noise level of 49 DB, equivalent to a small fan.

Although configuration 2 resulted in a lower performance than configuration 3, it is a valid option that does not require installing more specialized STPV panels, potentially replacing existing windows in a retrofit option. In the case of an existing solarium, BIPV/T may prove a simpler solution to installing ducting and PV panels on the roof than configuration 3. The generated heat improves the system's overall performance by around 5 % compared to the reference case.

3.2.2 Flexibility Characterization

Each of the models created was developed to analyze the overall energy flexibility of the various BIPV/T and STPV configurations. The simulation was conducted for three months (January, February, and March) during the heating season. The following sections will analyze and identify the parameter influence and optimal parameter values based on the BIPV/T configuration and DR technique.

3.2.2.1 Parameter Influence

A graphical representation of the parameter influence on the calculated average BEFI (shifted load during peak periods) throughout the simulation runtime is presented in Figure 3.13 to Figure 3.15. The analysis shows that the parameters have varying influences on the system's flexibility for each configuration. The tank volume had the greatest impact on the system in most cases. The solarium size typically had the least in all configurations except the passive solar system, which had the highest. Tank volume size influences the amount of thermal energy stored in the system that can be transferred to heat the solarium at night. Therefore, a larger tank can store and shift more heat into off-event periods. In configuration 3, the solarium size would influence the possible temperature of the zone and the inlet temperature to the heat pump as larger zones would heat up slower and may not reach the same temperatures as smaller zones.

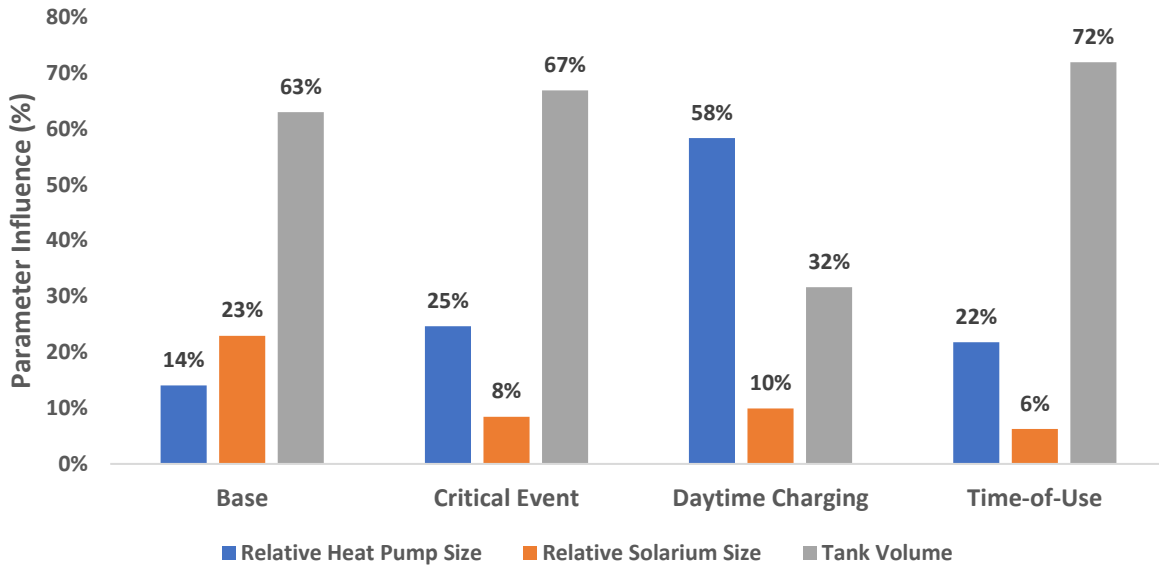


Figure 3.13: Parameter influence on the BEFI for the reference configuration

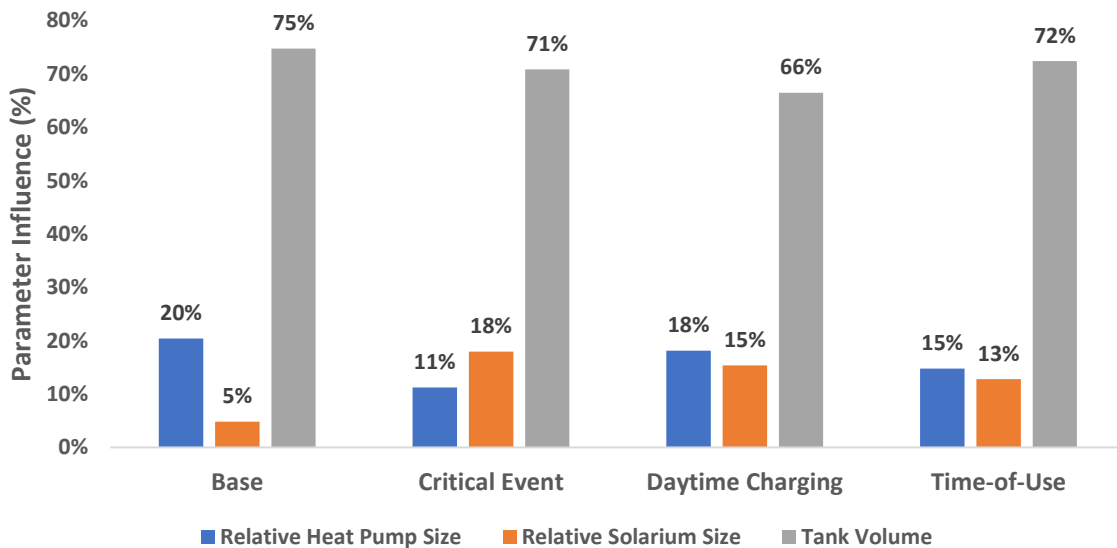


Figure 3.14: Parameter influence on the BEFI for the ducted configuration

The heat pump did not significantly impact configurations 1 and 2 as the heat pump ducted air from outdoors (or pre-heated air from outdoors in configuration 2). At lower temperatures, the heat pump shuts off, allowing for electrical only operation of the water heater. This is particularly true when heat pump operation occurs most often during the night unless using a daytime charging

strategy. As can be seen for configuration 2, the heat pump influence became the highest when utilizing daytime strategy as the heat pump can fully use the heat generated by the BIPV/T system.

Configuration 1 shows a similar parameter influence for all DR techniques. This is due to the absence of a thermal recovery system increasing the heat pump performance. The heat pump output capacity decreases at lower ambient temperatures limiting the heat capacity to the tank.

However, configuration 3 shows a more significant difference between DR strategies. This could be due to the addition of a solarium, as the solar irradiance had a considerable impact on the environmental temperature of the solarium. Therefore, the size of the solarium had the highest impact on the system for all DR strategies except daytime charging, where the heat pump size was the largest. With a daytime charging strategy, the heat pump's inlet temperature (environment temperature of the solarium) and the system's capacity were increased for the heat pump size. Thus, the system can provide additional heat to the tanks with a larger heat pump size, especially when the tank volume rises. As the building size increases, the demand on the system similarly increases; therefore, with a larger heat pump and a small tank, the tank would charge rapidly at the beginning of the day, causing the heat pump to cycle more frequently to maintain the tank temperature during the day.

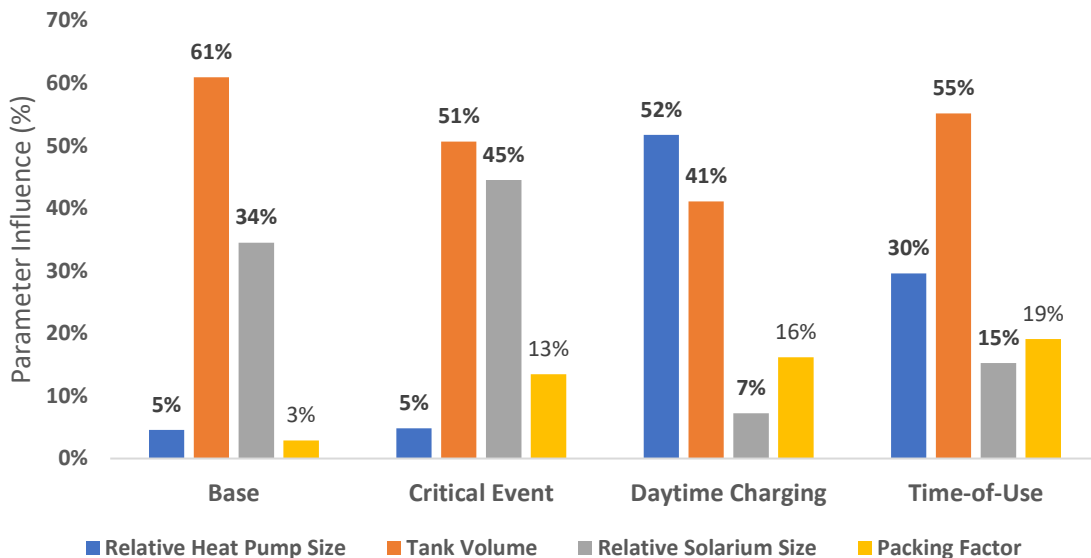


Figure 3.15: Parameter influence on the BEFI for the passive solar configuration

The packing factor had a significant impact on the system. At lower STPV packing factors (i.e. higher transparency), the heat gain into the solarium rises similarly, increasing the heat pump's COP. However, when isolating the packing factor parameter as a function of the average load shifted during peak periods, the average peak power consumption remains consistent between each value. Although the packing factor can affect the performance, it did not significantly influence the overall performance.

3.2.2.2 *Optimal parametric variables*

Table 3.5 summarizes the parametric analysis results with the optimal parametric values for each configuration. The tank volume remained consistent between DR strategies for configuration 1 with a volume between 300 – 500 L. However, the other configurations had a wider range of optimal values with a tank volume between 250 – 1000 L for the ducted configuration and 300 – 1000 L for the passive solar configuration. The highest tank volume was observed with a time-of-use schedule, whereas, with no DR technique, the tank size required is closer to the actual size of the tank. This could be due to a higher storage capacity needed to shift the load twice daily with a TOU schedule instead of the more infrequent peak events with the critical peak pricing strategy and did not fully utilize the solar gains as the daytime charging strategy does.

However, although a 500 - 600 L tank size is reasonable for a storage tank, the tank size found for the time-of-use strategy is more of an unreasonable size to store heat in residential homes. Additionally, the simulation was run using only one tank. Tanks larger than 500 L would be split into multiple tanks either in series or in parallel, which may cause this study's results to differ slightly. Therefore, it can be concluded that there was consistent optimal tank volume for most configurations and DR techniques. The daytime charging requires a larger tank size to fully realize the potential of the DR strategy.

The passive solar configuration notably had higher tank requirements than the other configurations as configuration 3 can use a higher environmental temperature to increase output capacity and store more thermal energy. In configuration 3, the packing factor had optimal values between 0.15 and 0.6, whereas a more transparent STPV was better with no DR techniques and the TOU schedule.

Table 3.5: Optimal parametric values

Reference				
<i>Parameters</i>	<i>No Demand Response</i>	<i>Daytime Charging</i>	<i>Critical Peak Pricing</i>	<i>Time-of-Use</i>
<i>Tank volume (L)</i>	300	500	400	500
<i>Relative Heat Pump Size (-)</i>	1.7	2	2.4	2
<i>Relative Solarium Building Size (-)</i>	0.5	0.5	0.5	0.5
Ducted BIPV/T				
<i>Parameters</i>	<i>No Demand Response</i>	<i>Daytime Charging</i>	<i>Critical Peak Pricing</i>	<i>Time-of-Use</i>
<i>Tank volume (L)</i>	250	350	500	1000
<i>Relative Heat Pump Size (-)</i>	1	1.5	1	1.5
<i>Relative Solarium Building Size (-)</i>	1	1	1	1
Passive Solar				
<i>Parameters</i>	<i>No Demand Response</i>	<i>Daytime Charging</i>	<i>Critical Peak Pricing</i>	<i>Time-of-Use</i>
<i>Tank volume (L)</i>	300	600	600	1000
<i>Relative Heat Pump Size (-)</i>	2	2.2	2.5	2
<i>Relative Solarium Building Size (-)</i>	1	1	1	1
<i>Packing Factor (-)</i>	0.15	0.4	0.6	0.15

The heat pump size remains consistent between DR strategies; however, each configuration had a different range of optimal values. Configuration 1 had an optimal size between 1.7 – 2.4, configuration 2 was between 1 – 1.5, and the passive solar configuration was between 2 – 2.5. Overall, the range of values suggests that a higher capacity heat pump would be optimal for configurations 1 and 3, but configuration 2 benefits from the smaller heat pump size. This is due to the flow rate of the heat pump, as the flow rate increases the larger the heat pump, and this would similarly decrease the heat gained from the BIPV/T system, as previous studies demonstrated that the higher the flow rate, the lower the temperature rise from the BIPV/T (ASHRAE, 2019).

It is noted that, contrary to the parametric influence values, the solarium building size did not significantly impact the system's average flexibility as between DR techniques, the building size multiplier remains between 0.5 – 1, depending on the configuration. This shows that a smaller building (~100 m²) was optimal for this application.

Chapter 4. Demonstration and Experimental Verification

To demonstrate and verify the major configuration studied, an experiment was conducted in the new research house at Concordia University, known as the Future Buildings Laboratory (FBL), in Montreal, Canada. The experiment simulates the performance of scenario 3 (passive solar STPV – HPWH) from the simulation analysis in Chapter 3. The following sections present the objectives, experimental setup, equipment, instrumentation, and results from the experiment.

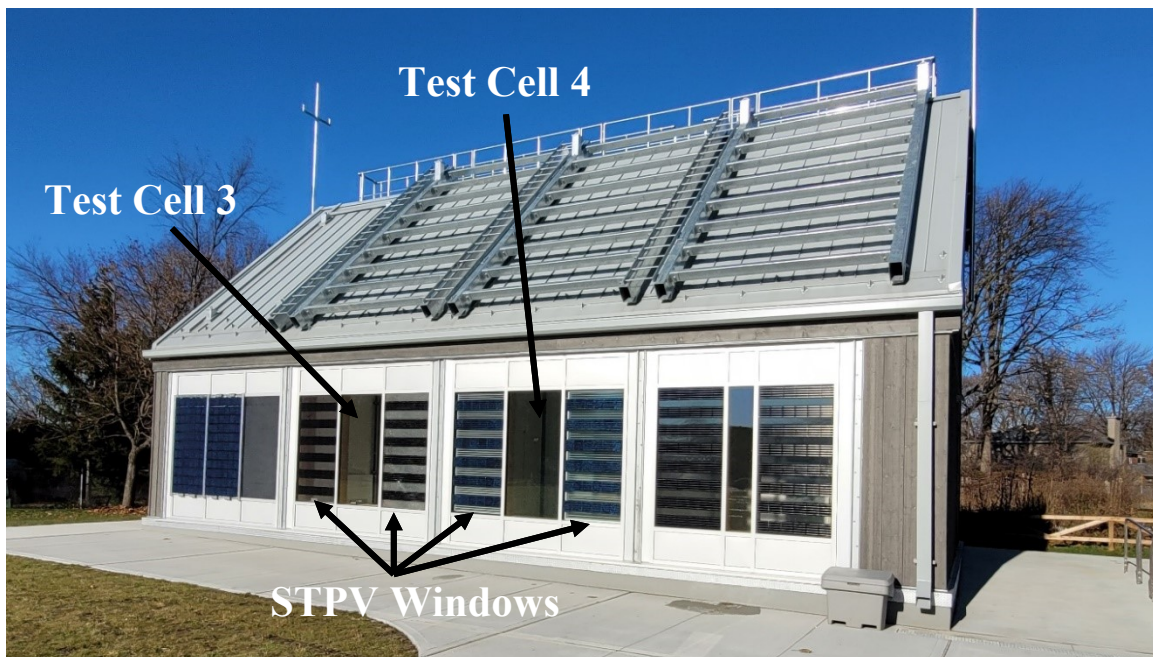


Figure 4.1: Future Buildings Laboratory at Concordia University

4.1 Objectives

The primary objectives of this experiment were:

- Demonstrate and analyze the performance of a passive solar building combined with a heat pump water heater and STPV windows with real data using two test rooms seen in Figure 4.1.

- Compare the simulated data with the experimental data to partially verify the model.

4.2 Experimental Setup

This experiment utilizes two isolated test rooms, test cells 3 and 4 (Figure 33). Two rooms were utilized in the experiment: one supplies air to the heat pump and is heated by the tank’s stored energy; the other room receives cooler return air from the heat pump. The purpose of the split solarium is to prevent heat pump cycling from supplying and exhausting air to the same room. The test cells windows are south-facing. A small air duct connects the two test rooms to allow airflow between rooms. The experiment utilizes three main components installed into the rooms: heat pump, fan coil, and water pump. The key equipment and controllers utilized are listed in Table 4.1.

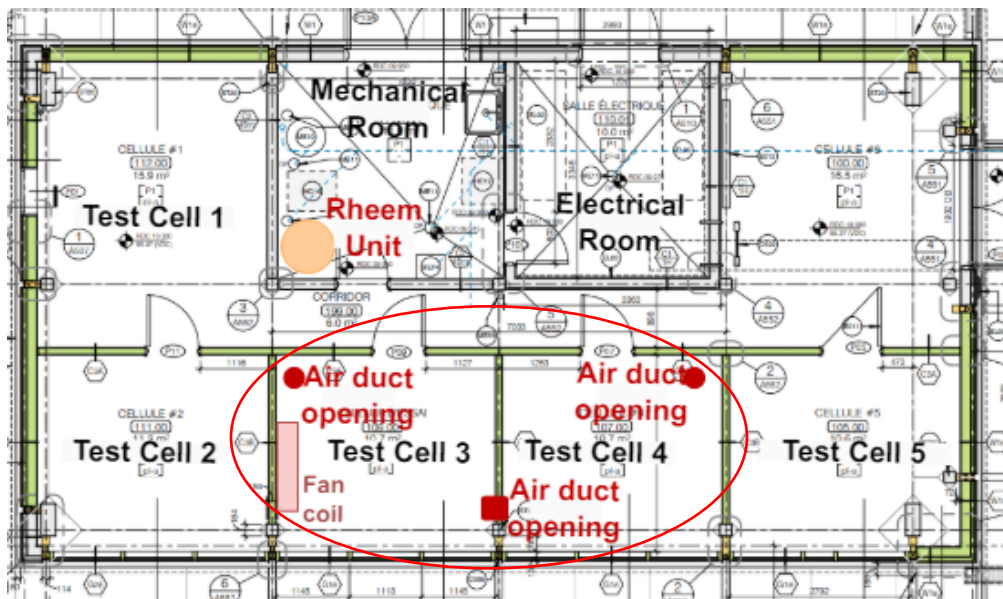


Figure 4.2: Future Building Laboratories (FBL) floor plan schematic

The heat pump used is a Rheem Hybrid Electric Heat Pump Water Heater, a relatively new innovation in the industry that enables use of ducted solar-heated air to be used a heat source for an integrated air-water heat pump. This unit is a combined heat pump (on top) with a 45-Gal tank on the bottom of the unit. The heat pump supplies solar-heated air from one test room (simulating the solarium) and exhausts air to the other room (seen in Figure 4.3). The heat pump is controlled by the manufacturer's mobile app Econet to adjust the water temperature setpoint and program a

setpoint schedule. The app provides the hourly electricity consumption of the heat pump and allows for remote motoring of the system. The water in the integrated storage tank is used to provide the stored heat to a fan-coil unit in one of the test rooms, and a thermostat-controlled water pump circulates the water. Note that the solar heat is stored in the tank during the daytime and used to heat the space during the time when solar radiation is low (or at night) and there is a need to reduce electricity consumption in response to grid signals/needs.

4.2.1 Equipment

The four main components utilized in the experiment are outlined in Table 4.1, including the heat pump, thermostat, fan coil, and water pump (circulator) utilized in the experiment. Figure 4.4 shows the setpoint temperature profile programmed into the heat pump, fan coil unit, and thermostat controlling the water pump. The water pump temperature sensor measures the room temperature near the fan coil, while the fan coil has an internal temperature sensor. The heat pump has an internal temperature sensor controlled by the mobile app connected to the device. Figure 4.5 and Figure 4.6 show the setup of the experiment and the placement of each component on the system.

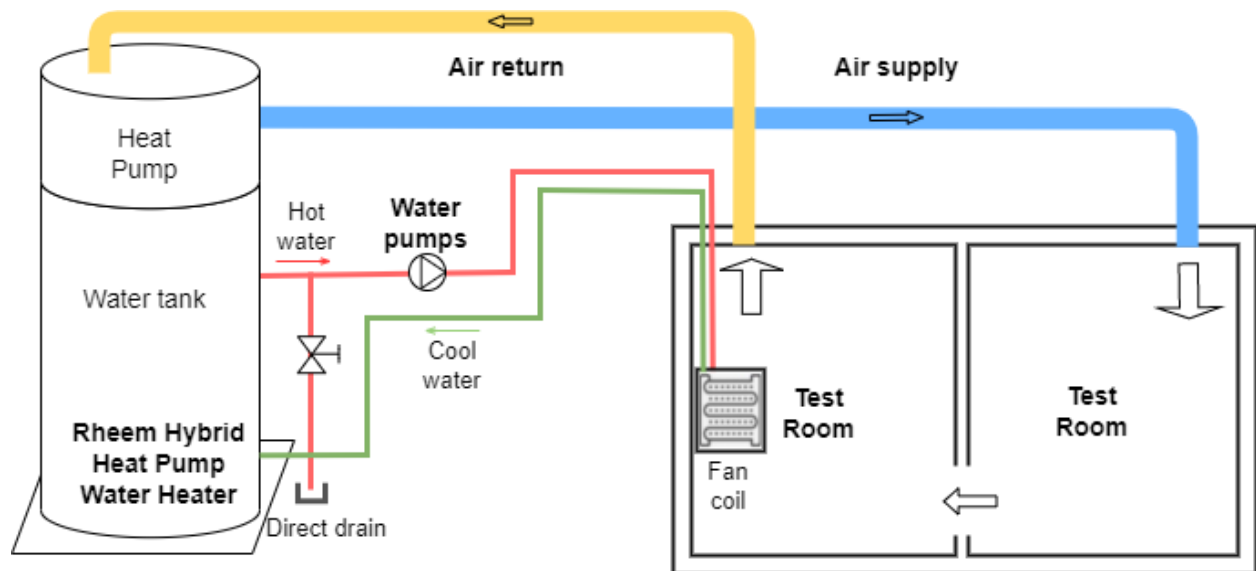


Figure 4.3: Experimental setup

4.2.2 Test Rooms

Each test room has approximately 6 m² of window area, with 4 m² of 50% transparent STPV. Test cell 4 has shades installed onto the windows, which are continuously open for the duration of the experiment. It should be noted that prior to testing, one STPV panel was damaged in test cell 3.

4.2.3 Measurement Instruments

Several measurement equipment was utilized for the experiment, and the instruments and the associated accuracy are listed in Table 4.2. The sampling time for the experiment was 1-minute intervals. A weather station was not yet installed on the façade for the experiment due to delays from the pandemic; therefore, all weather data was obtained from the Montreal International Airport weather station. The average airflow velocity of the Rheem heat pump was 5.35 ± 0.16 m/s at the exit of the vent in test cell 4, and this was measured with a manual air velocity meter as an average of 5 measurements.

Table 4.1: Key experimental equipment used

Equipment	Implementation
Rheem Heat Pump Water Heater (CPROPH50T)	Installed in the mechanical room, heats water supplied to the fan coil unit.
Inkbird Temperature Controller (ITC-306T)	Controls the water pump.
Myson iVector Hydronic Heating Fan Convectors (iV60 FX 080)	Fan coil installed in test cell 3 to heat the room at night.
Grundfos Water Pump Circulator (UP 15-29 SF)	Circulates water to the fan coil from the heat pump.

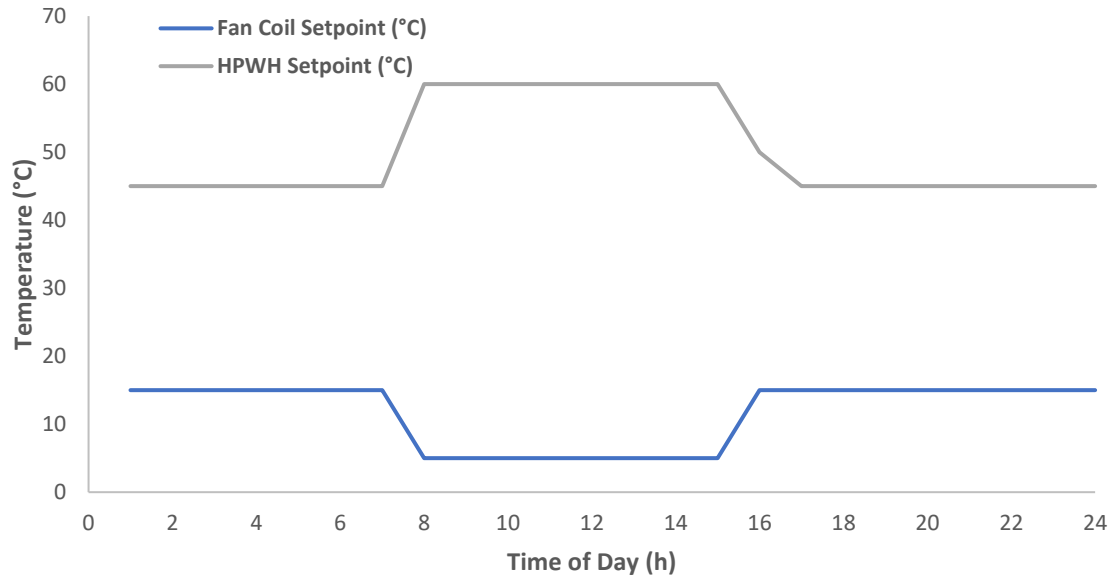


Figure 4.4: Fan coil and heat pump water heater temperature setpoints

4.2.4 Sensor Positioning

Fourteen sensors (thermocouples) in total were utilized to measure air temperatures. Four sensors were used for the inlet/outlet of the fan coil and heat pump’s water side. The list of each sensor and the name associated with the measurement are shown in Table 4.3, while Figure 4.7 shows the placement of the air temperature sensors in the test rooms. Four air sensors were placed in each testing room to measure the room temperatures, and two were placed at the entrance of the ducts that transmit air to/from the heat pump in each room. Two sensors were placed on the top and bottom vents of the fan coil unit in test cell 3. Finally, two sensors were placed as the air side exit of the heat pump.

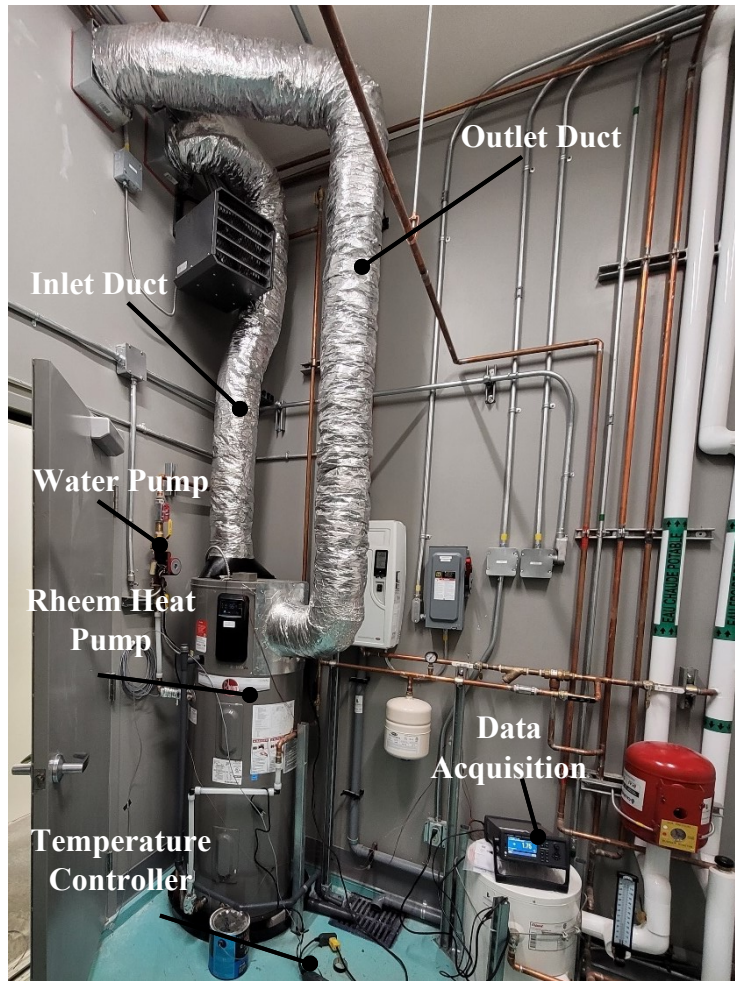


Figure 4.5: Installed Rheem Heat Pump Water Heater with ducting

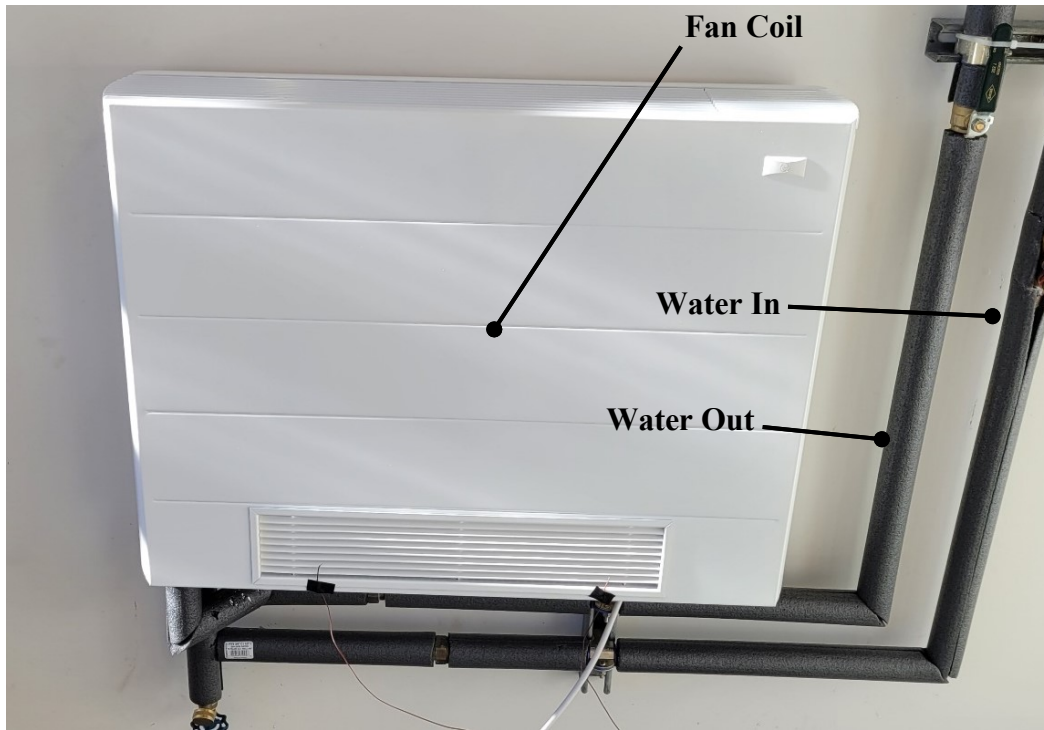


Figure 4.6: Installed iVector fan coil

Table 4.2: Experimental instrument accuracy and implementation

Instruments	Accuracy	Implementation
Thermocouple – Type T	± 0.5 °C	18 Thermocouples are used to measure air and water temperatures.
TSI Alnor 9535 VelociCalc Air Velocity Meter with straight probe	$\pm 3\%$ of reading or ± 0.015 m/s	Manual measurement of heat pump's airflow.
Turbine Flow Meter (K24)	$\pm 1\%$	Measures the water flow rate from the heat pump to the fan coil.
Rheem Energy Measurement	Not Provided	Measures and outputs the electricity consumed within 2 hours.
Keysight Data Acquisition System (DAQ 907A)	± 0.05 %	Reads the temperatures from the thermocouples every 1 minute.

Table 4.3: List of sensors installed and positions

Sensor Name	Description
T_{r1}	Thermocouples installed in test cell 3 (Figure 4.7)
T_{r2}	Thermocouples installed in test cell 4 (Figure 4.7)
T_{duct}	Thermocouples installed at the inlet/outlet of the heat pump's air side (Figure 4.7)
T_w	Thermocouples installed at the inlet/outlet of the fan coil's water side
T_{FC}	Thermocouples installed at the fan coil's air side (top vent and bottom vent)
T_{HP}	Thermocouples are installed at the inlet/outlet of the heat pump's water side.

4.3 Results and Comparison

In this section, the experimental results are presented and compared to the passive solar scenario from Chapter 3 to verify the model's key components. The building model was modified and split into two solarium rooms to simulate the experimental setup for the verification.

4.3.1 Experimental Results

The experiment was conducted between December 10th and December 17th, 2021. Figure 4.8 to 4.11 present the results obtained for sunny and cloudy weather conditions on December 11th and 12th, 2021 with a mean temperature of 3.5 °C and calculated max irradiance levels of 230 W/m² (cloudy day) and 830 W/m² (sunny day). Additional experimental results can be found in Appendix D.

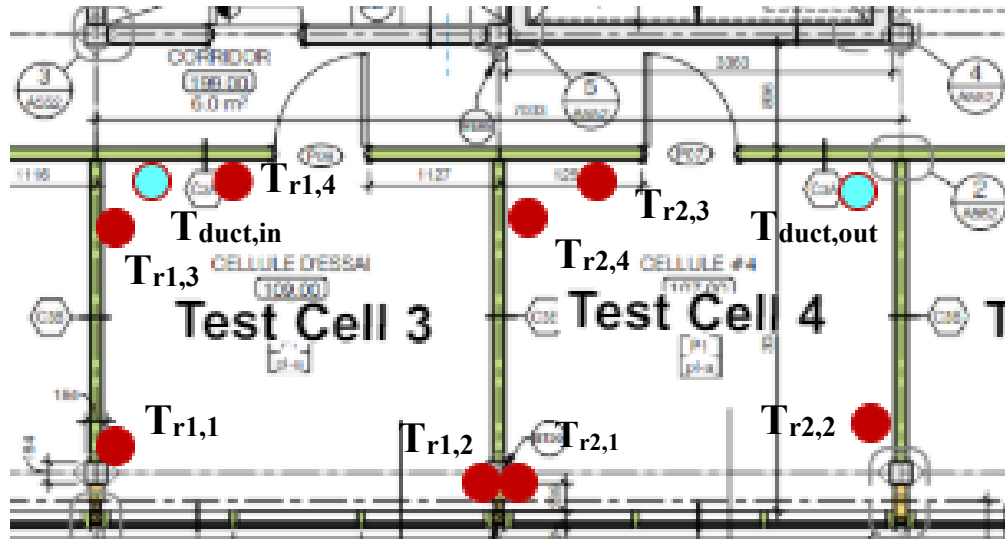


Figure 4.7: Thermocouple placement. Red Dots: Room temperature. Blue Dots: Inlet/outlet duct temperatures

The figures, as expected, show a minimal temperature increase during a cloudy day. The heat pump and fan coil run periodically during the night to maintain the room and water tank temperatures. The fan coil operation is seen by the sharp increase in temperature, as indicated in Figure 4.8. In contrast, the heat pump operation is ascertained from the sharp decrease in temperature from Figure 4.9. However, on December 12th (sunny day), the room temperature increased to over 25 °C (test cell 3) and 21 °C (test cell 4) during the day solely from solar heat gain when the fan coil unit was not active.

The test room supplying air to the heat pump (test cell 3) is consistently above 15 °C, which means that the heat pump operates at a higher COP than outdoor air. This is particularly true on December 12th, when the room temperature reaches above 25 °C.

Test cell 4 is consistently 4 – 5 °C colder than test cell 3, indicating that the small opening between the two rooms for air circulation does not provide sufficient heat transfer to maintain the temperature in both rooms and this is acceptable since the main objective of the opening is to allow the air pressure to equalize between the two rooms and accommodate the return air from the heat pump. This is also seen when the fan coil provides heat, as the temperature in test cell 3 increases by over 4 °C when the fan coil is running, while test cell 4 increases by 2 °C. Additionally, test cell 4 is supplied with cooler exhaust air from the heat pump, and there is no heating in the room; the room temperature is typically colder than test cell 3. On a sunny day, test cell 4 has a lower

peak temperature due to the constant operation of the heat pump to pre-heat the tank. This effect shows the secondary function of the passive solar configuration, where the heat pump can serve as a means of transfer heat from one part of a house to another part – storing part of the solar heat for later use, while cooling another space.

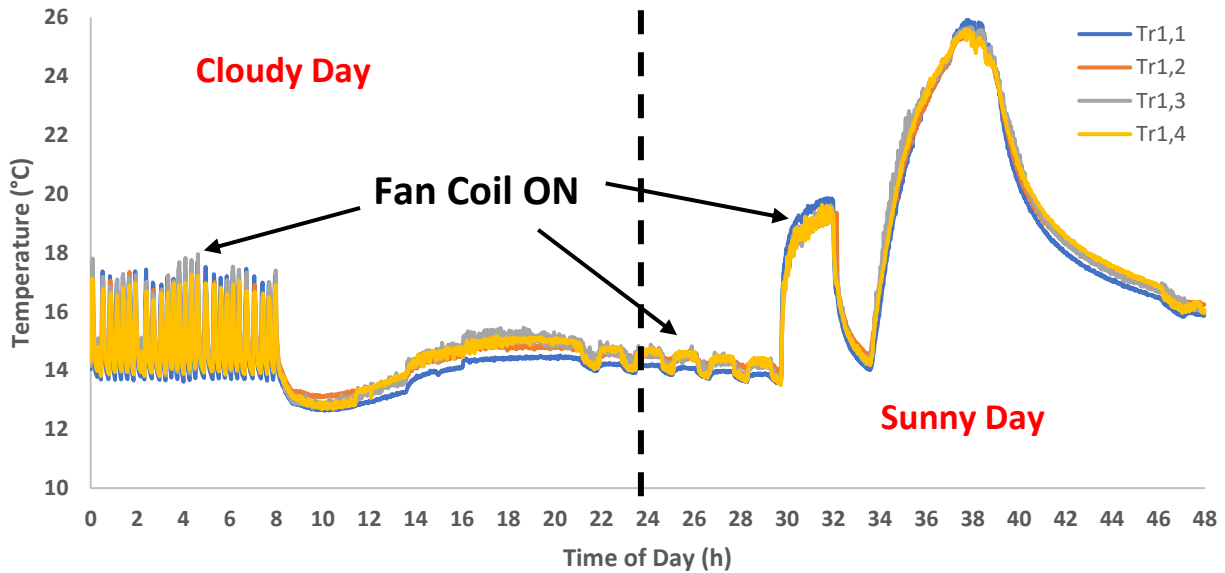


Figure 4.8: Room temperatures in test cell 3 on December 11th (cloudy) and 12th (sunny), 2021

It is important to note that a temperature sensor in test cell 4, $T_{r2,2}$, has a temperature similar to test cell 3, which could be due to poor heat distribution in the room or an error in the sensor. It is interesting to note that following a sunny day, the room temperature stayed above 15 °C, meaning that the fan coil was not operational until the following day. The water tank temperature similarly decreased slowly due to no draw on the tank; hence, the heat pump was not required to run until the following day, as seen in Figure 4.10.

Figure 4.10 shows the outlet water and air temperature supplied to test rooms 3 and 4, respectively, as well as the electricity consumed by the heat pump every 2 hours. This figure shows that the heat pump operates at the beginning of the day to pre-heat the water tank and periodically at night to maintain the lower temperature. The actual operation of the heat pump can be discerned from $T_{duct,out}$, as, when the heat pump is operating, the outlet air temperature from the heat pump is close to 5 °C. Following a sunny day, the heat pump decreased electricity consumption compared to the cloudy day.

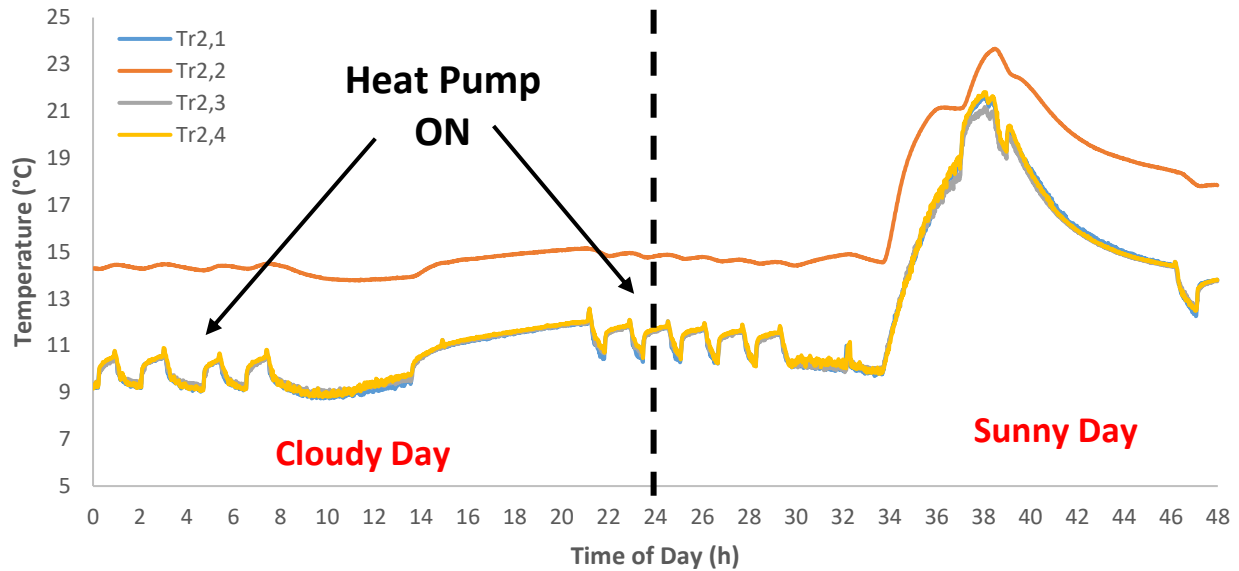


Figure 4.9: Room temperatures in test cell 4 on December 11th (cloudy) and 12th (sunny), 2021

4.3.2 Verification

The measurements gathered throughout the experiment were utilized to verify and compare the models in MATLAB and Python. Figure 4.11 compares the solarium room temperature of test cell 3 with the simulation results. Overall, the temperatures follow the experimental results closely with an RMSE of 2.03 °C except for a brief temperature increase at the beginning of the second day. This is due to the simulation parameters, as the simulated fan coil did not switch on at the temperature increase on December 12th. In the simulation, the temperature setpoint for the fan coil lowers before the setpoint in the experiment. Other minor deviations in the temperature results are likely due to estimated parameters in the model, such as the true thermal capacitance of the room as well as slight deviations in the control schemes.

Figure 4.12 compares the simulation and experimental results for the water tank. The water temperatures generally follow a similar trend in the simulation as the experimental results. However, the simulated water tank tends to have a lower heat loss than the experimental tank. This could be due to the estimations and assumptions utilized in the model, such as the tank's insulation, which is estimated based on a typical water tank structure. In addition, the position and properties of the water coils within the tank, heated by the heat pump, were estimated.

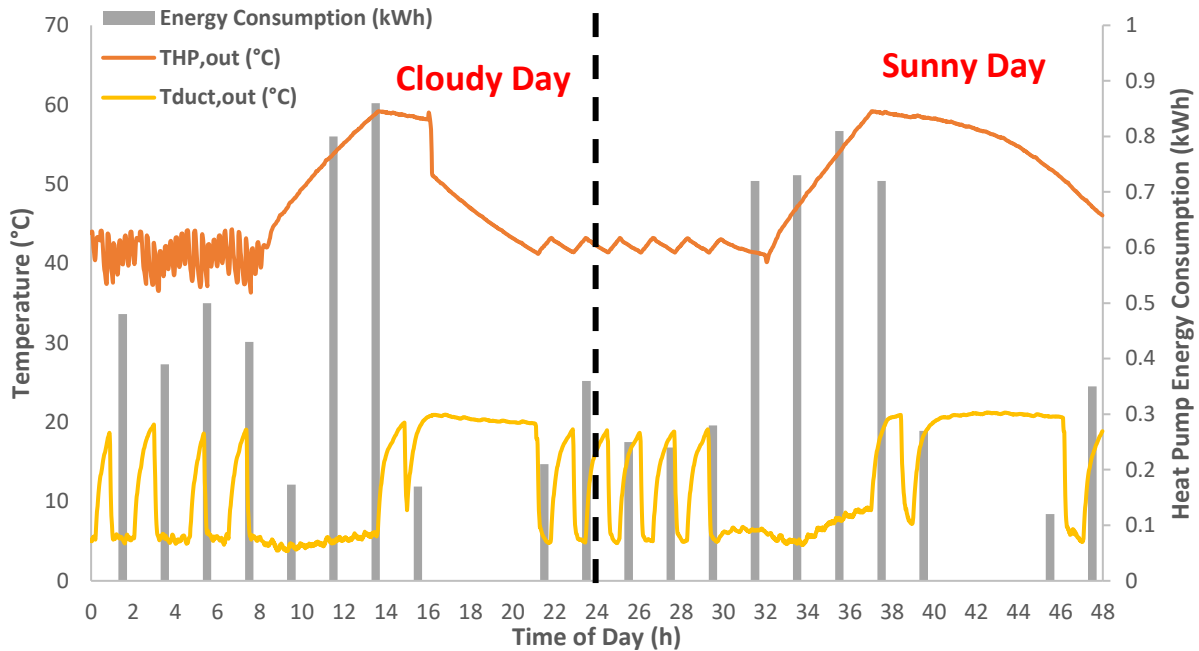


Figure 4.10: Heat pump water temperature out of the tank, air temperature out, and electricity consumption on December 11th (cloudy) and 12th (sunny), 2021

Furthermore, there was no exact measurement obtained for the operation of the water pump. An estimation of the draw was calculated based on the room temperature of test cell 3 (where the temperature sensor for the water pump thermostat is located) and used within the model. In addition, the temperature controlling the thermostat was not logged. Another thermostat placed at a similar position was used instead to calculate the flowrate indicator. This means that the actual draw on the tank may vary compared to the experiment. This is likely why the temperature decrease on December 11th after 4:00 pm is different from the simulation model.

Figure 4.12 shows that the water pump is operating starting from 4:00 pm, as seen from the similar temperature exiting the heat pump and entering the fan coil ($T_{HP,out}$ and $T_{w,in}$). The temperature difference is up to 6 °C when the water pump is not operating. The water draws from the tank at the beginning of December 11th have slightly more exaggerated downward spikes in temperature with the experimental results compared to the simulation. However, the temperatures and overall trend are similar in both cases despite these differences.

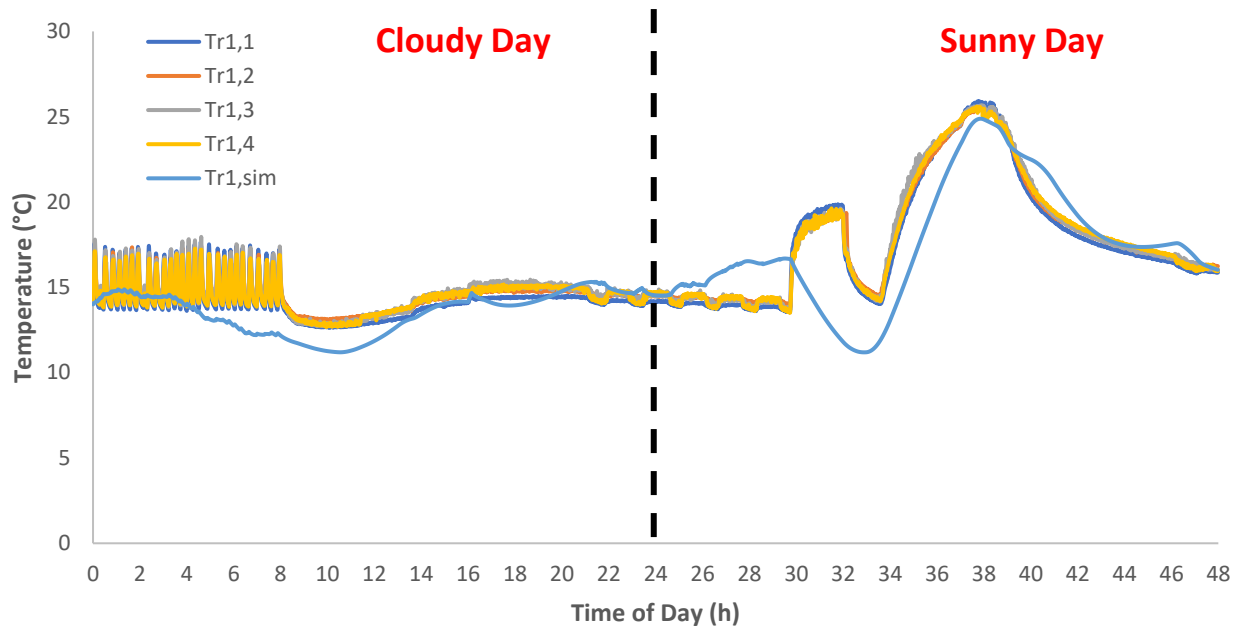


Figure 4.11: Test cell 3 room temperature simulation and experimental results comparison on December 11th and 12th, 2021

The total electricity consumption of the heat pump was compared to the heat pump’s simulated output for those two days. The total heat pump electricity consumed in the experiment is 8.9 kWh, whereas the simulated heat pump outputted 8.7 kWh (~0.2 kWh deviation), which is acceptable for a preliminary proof-of-concept test. A summary of the deviation and RMSE calculated for each measurement is found in Table 4.4.

4.4 Conclusions

The experiment resulted in a successful demonstration and proof-of-concept of the passive solar configuration, and the results provided a preliminary verification of the configuration and simulation model. Despite the cold ambient temperature, the test room temperatures increased to over 20 °C from the solar gains, verifying the concept and providing a lower electricity consumption than predicted. This means that the test rooms’ (and solarium’s) excess thermal energy can be utilized for other applications, such as ventilation to the rest of the building to reduce the building’s space heating electricity consumption.

The heat pump and fan electricity consumption were reduced after charging the tank on a sunny day. The simulation model provided a temperature and electrical output similar to the experimental

results with minimal deviation in test cell 3’s air temperature. Deviations in the results are due to the assumptions made in the simulation that differ from the experimental setup. Overall, the simulation model adequately represents the experimental results, verifying the use of the model and subsequent simulation results.

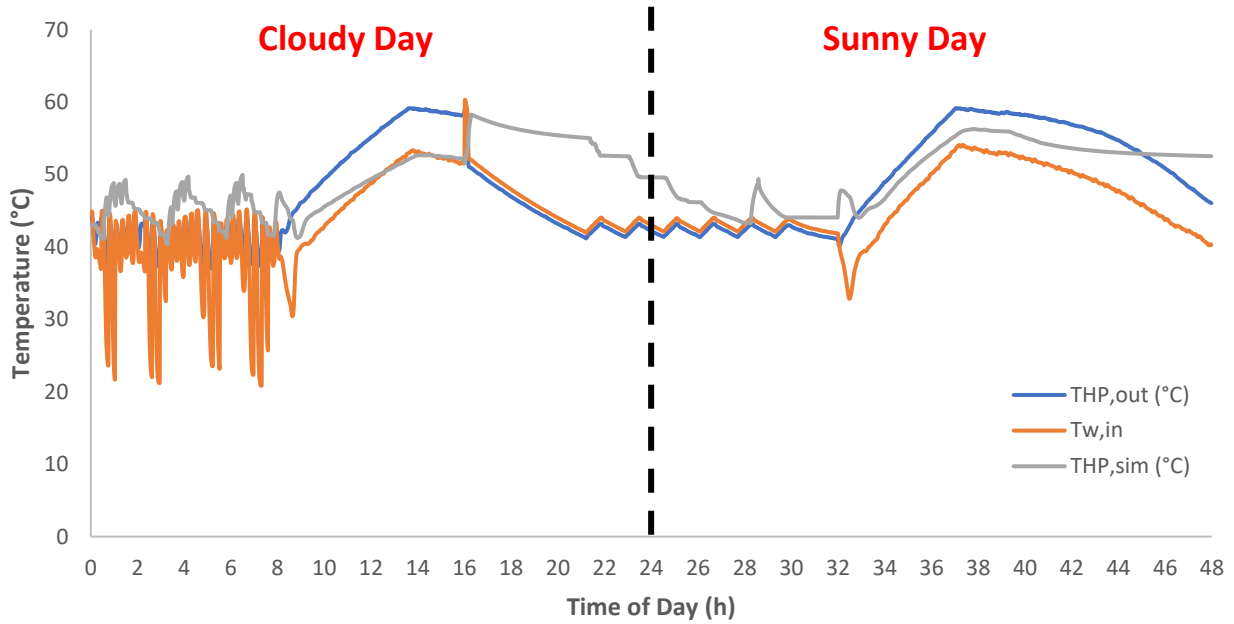


Figure 4.12: Heat pump water temperature simulation and experimental results comparison on December 11th and 12th, 2021

Table 4.4: Average deviation and RMSE comparing the simulation and experimental results

Variable	Average Deviation	RMSE	Normalized RMSE**
Average test cell 3 room temperature *	0.72 °C	2.0 °C	0.1
Average test cell 4 room temperature *	4.0 °C	6.7 °C	0.3
Water tank outlet temperature	1.7 °C	5.7 °C	0.4
Heat pump electricity consumed	0.2 kWh	-	-

*Experimental room temperature calculated from the average of the four sensors in each room

**Normalized based on the allowed temperature range

Chapter 5. Summary and Conclusions

In this thesis, different BIPV-HPWH configurations, parameters, and demand response strategies are used to maximize the energy flexibility of the system and determine the optimal parameter sizes to achieve this goal, while also enhancing energy efficiency. The passive solar configuration outperformed the other configurations in terms of electrical consumption with a decreased electricity consumption of over 80% compared to the reference configuration (BIPV-HPWH). In addition, this passive solar configuration (configuration 3) could heat the solarium without using auxiliary heating.

An analysis of the parametric influence on the average load shifted showed that for all configurations except configuration 3, the tank volume had the highest impact on performance due to the use of outdoor air. In contrast, a stronger influence of the solarium size was shown in configuration 3. This means that the temperature increased from solar gain will vary depending on the solarium size, affecting the inlet temperature to the heat pump. Additionally, the DR strategies significantly impacted the parametric influence for configuration 3. For example, the heat pump size had the greatest effect on daytime charging strategy, which is expected due to the addition of the solarium and a higher dependence on solar irradiation. This indicates that the heat pump size had the strongest influence with an increased inlet temperature.

In terms of demand response strategies, there is optimal region of thermal storage (tank size) size between 300 L and 600 L for all DR strategies except time-of-use, where the optimal size is closer to 1000 L. The relative heat pump size had an apparent near-optimal of 2 – 2.5 times the regular size for configuration 3. The STPV packing factor (on the solarium windows) yielded a higher performance at lower values with all DR techniques except daytime charging and TOU, where mid-range values of 0.4 and 0.6, respectively, were ideal.

In summary, the prominent factors that influence the system's flexibility are the heat pump size and the tank volume for most demand response techniques and configurations. The solarium size had the strongest influence with configuration 3. Additionally, the passive solar design yielded the best results when combined with the daytime charging technique. The added solarium provides a better environment for improved heat pump performance than the other configurations. In addition,

this configuration provides a way to transfer solar heat from the southern to the northern part of a house.

An experimental analysis was conducted in Concordia University's Future Buildings Laboratory to simulate the performance of the passive solar configuration and verify the simulation model. The experiments confirmed the as-planned operation of each of the components. There were slight differences in the temperatures and operation of the components for the simulation compared to the experimental setup where temperature spiked or lowered based on different operation times. However, the temperature and electricity consumption trends were similar to the simulation and experimental results.

The experimental analysis provided a partial verification and demonstrated the potential of the new passive solar configuration from the high environmental temperature achieved on a sunny day. Excess heat is available within the solarium despite storing the thermal energy gained on a sunny day. This extra thermal energy can be used for other applications such as the building's ventilation (reducing space heating load) or heating the building with the heat pump water heater in addition to the solarium. The experimental analysis demonstrated the need for further research on applying the excess heat.

It should be noted that this is a preliminary experiment with limitations due to the pandemic. As such, measurements were only taken for around a week. The tests will be in-depth and gather data for an extended period in future experiments. Additionally, the experiment was limited in the sensors used. Ideally, the irradiance into the room, water flowrate, water tank temperature, STPV generation, and fan coil airflow would be measured and logged. Another limitation is the assumptions made for the experiment and simulation, such as the solarium's thermal capacitance, water pump operation, and thermal storage properties. Due to the assumptions and limitations of the experiment, there were explainable differences between the model and experimental results.

5.1 Contributions

A fully integrated numerical model implemented in MATLAB and Python was developed and verified. The model can simulate the energy performance of a complete system, including an air-to-water heat pump, water storage, multi-zone building, and BIPV/T systems and determine the

potential flexibility of multiple demand response strategies. These methods allowed for an annual electricity consumption analysis that showed that the passive solar configuration improved the energy performance of the air-to-water heat pump by ~80% compared to a standard system. In addition, the parametric analysis provided the optimal water tank, heat pump, and building sizes of four different control strategies. The experimental analysis provided a partial verification of the results achieved, confirmed the performance, and validated using a solarium to increase the inlet temperature provided to the heat pump room. A significant contribution of this research was not only in the results presented but the future potential of this field due to the solarium's high environmental temperature. This work has been presented at the 16th Conference on Sustainable Development of Energy, Water, and Environment Systems, and submitted to the Renewable Energy Journal.

5.2 Future Work

This research provided the basis for future work as it demonstrated the importance of utilizing a solar-heated room to reduce a heat pump's electricity consumption and determined key components' parametric influence to maximize flexibility. However, several aspects of this study should be expanded, such as generalizing the analysis for different building configurations and systems and going more in-depth into the different options. This includes building sizes, window areas for the solarium, different heat pumps. A complete experimental analysis will be performed to confirm the simulation results for each configuration. The experiment will include proper measurement tools for the weather station and an additional temperature sensor for the interior of the water tank. The BIPV/T model will also be improved to optimize the system's operation and provide the best output temperature. Finally, as the experimental and simulation results showed, the passive solar configuration has the potential for further study to improve system's operation, utilize excess heat in the solarium for other applications, further analyze the winter operation's current configuration, and study the summer operation.

Chapter 6. References

- Abdelsalam, M., Lightstone, M., & Cotton, J. (2019, 6 1). A novel approach for modelling thermal energy storage with phase change materials and immersed coil heat exchangers. *International Journal of Heat and Mass Transfer*, 136, 20-33.
- Adeli, M. M., Sobhnamayan, F., Farahat, S., Alavi, M. A., & Sarhaddi, F. (2012). Experimental Performance Evaluation of a Photovoltaic Thermal (PV/T) Air Collector and Its Optimization. *Journal of Mechanical Engineering*, 58, 309-318.
- Allison, J., Bell, K., Clarke, J., Cowie, A., Elsayed, A., Flett, G., . . . Tuohy, P. (2018). Assessing domestic heat storage requirements for energy flexibility over varying timescales. *Applied Thermal Engineering*, 136, 602-616.
- Al-Waeli, A. H., Kazem, H. A., Chaichan, M. T., & Sopian, K. (2019). Applications and PV/T Systems. In *Photovoltaic/Thermal (PV/T) Systems* (pp. 223-263). Springer, Cham.
- Arteconi, A., Mugnini, A., & Polonara, F. (2019). Energy flexible buildings: A methodology for rating the flexibility performance of buildings with electric heating and cooling systems. *Applied Energy*(251), 113387.
- ASHRAE. (2018). *ASHRAE Handbook - HVAC Applications 2018*. Atlanta: ASHRAE.
- ASHRAE. (2019). *2019 ASHRAE Handbook—HVAC Applications*. Atlanta: ASHRAE.
- Athienitis, A. (1998). *Building Thermal Analysis*. Boston MA: Electronic Mathcad Book, MathSoft Inc.
- Athienitis, A., Dumont, E., Morovat, N., Lavigne, K., & Date, J. (2020). Development of a dynamic energy flexibility index for buildings and their interaction with smart grids. *Summer Study on Energy Efficiency in Buildings*. Montreal.
- Bambara, J. (2012). *Experimental Study of a Façade-integrated Photovoltaic/thermal System with Unglazed Transpired Collector*. Montreal: Concordia University.
- Bambara, J., & Athienitis, A. (2019). Energy and economic analysis for the design of greenhouses with semi-transparent photovoltaic cladding. *Renewable Energy*(131), 1274-1287.
- Bastien, D., & Athienits, A. (2010). Analysis of the Solar Radiation Distribution and Passive Thermal Response of an Attached Solarium/Greenhouse. *International High Performance Buildings Conference*. Purdue.
- Bastien, D., & Athienits, A. (2012). A control algorithm for optimal energy performance of a solarium/greenhouse with combined interior and exterior motorized shading. *Energy Procedia*, 30, 995-1005.

- Benli, H. (2011). Energetic performance analysis of a ground-source heat pump system with latent heat storage for a greenhouse heating. *Energy Conversion and Management*, 52, 581-589.
- Biancardo, M., Taira, K., Kogo, N., Kikuchi, H., Kumagai, N., Kuratani, N., . . . Nakata, J. (2006). Characterization of microspherical semi-transparent solar cells and modules. *Solar Energy*(81), 711-716.
- Bigaila, E., & Athienitis, A. (2017). Modeling and simulation of a photovoltaic/thermal air collector assisting a façade integrated small scale heat pump with radiant PCM panel. *Energy and Buildings*, 149, 298-309.
- Burch, J., & Christensen, C. (2004). *TOWARDS DEVELOPMENT OF AN ALGORITHM FOR MAINS WATER TEMPERATURE*. Golden, Colorado: National Renewable Energy Laboratory.
- Candanedo, L., Athienitis, A., Candanedo, J., O'Brien, W., & Chen, Y. (2010). Transient and Steady State Models for Open-Loop Air-Based BIPV/T Systems. *ASHRAE Transactions* 2010, 116, 600-612.
- Chae, Y. T., Kim, J., Park, H., & Shin, B. (2014). Building energy performance evaluation of building integrated photovoltaic (BIPV) window with semi-transparent solar cells. *Applied Energy*(129), 217-227.
- Chen, Y., Athienitis, A., & Galal, K. (2010). Modeling, design and thermal performance of a BIPV/T system thermally coupled with a ventilated concrete slab in a low energy solar house: Part 1, BIPV/T system and house energy concept. *Solar Energy*(84), 1892-1907.
- Chow, T., Chan, A., Fong, K., Lin, Z., He, W., & Ji, J. (2009). Annual performance of building-integrated photovoltaic/water-heating system for warm climate application. *Applied Energy*, 86(5), 689-696.
- Coninck, R. D., Baetens, R., Verbruggen, B., Driesen, J., Saelens, D., & Helsen, L. (2010). Modelling and simulation of a grid connected photovoltaic heat pump system with thermal energy using Modelica. *8th International Conference on System Simulation in Buildings*. Liege.
- Cruikshank, C. A. (2009). *EVALUATION OF A STRATIFIED MULTI-TANK THERMAL STORAGE FOR SOLAR HEATING APPLICATIONS*. Kingston: Queen's University.
- Debbarma, M., Sudhakar, K., & Baredar, P. (2017). Thermal modeling, exergy analysis, performance of BIPV and BIPVT: A review. *Renewable and Sustainable Energy Reviews*, 73, 1276-1288.
- Delisle, V. (2015). *A Model to Evaluate the Performance of BIPV-T Air Systems*. Varennes: Natural Resources Canada.
- Delisle, V., & Kummert, M. (2016). Cost-benefit analysis of integrating BIPV-T air systems into energy-efficient homes. *Solar Energy*(136), 385-400.

- Deschesne, B., Tello-Oquendo, F., Gendebien, S., & Lemort, V. (2019). Residential air-source heat pump with refrigerant injection and variable speed compressor: Experimental investigation and compressor modeling. *International Journal of Refrigeration*, 108, 79-90.
- Dimri, N., Tiwari, A., & Tiwary, G. (2018). Effect of thermoelectric cooler (TEC) integrated at the base of opaque photovoltaic (PV) module to enhance an overall electrical efficiency. *Solar Energy*(166), 159-170.
- Duffie, J., Beckman, W., & W.M., W. (2003). Solar Engineering of Thermal Processes. *Journal of Solar Energy Engineering*.
- Dumoulin, R. (2019). *Integrated Modelling and Analysis of a Heat Pump BIPV/T System with*. Montreal: Concordia University.
- Emmott, C. J., Röhr, J. A., Campoy-Quiles, M., Kirchartz, T., Urbina, A., Ekins-Daukes, N. J., & Nelson, J. (2015). Organic photovoltaic greenhouses: a unique application for semi-transparent PV? *Energy and Environmental Science*(8), 1317-1328.
- Facci, A., Krastev, V., Falcucci, G., & Ubertini, S. (2018). Smart integration of photovoltaic production, heat pump and thermal energy storage in residential applications. *Solar Energy*. Retrieved from <https://doi.org/10.1016/j.solener.2018.06.017>
- Farshchimonfared, M., Bilbao, J., & Sproul, A. (2015). Channel depth, air mass flow rate and air distribution duct diameter optimization of photovoltaic thermal (PV/T) air collectors linked to residential buildings. *Renewable Energy*, 76, 27-35.
- Federal Energy Regulatory Commission. (2006). *Assessment of Demand Response and Advanced Metering*. Washington: Federal Energy Regulatory Commission.
- Fischer, D., & Madani, H. (2017). On heat pumps in smart grids: A review. *Renewable and Sustainable Energy Reviews*(70), 342-357.
- Gaillard, L., Ménézo, C., Giroux, S., Pabiou, H., & Le-Berre, R. (2014). Experimental study of thermal response of PV modules integrated into naturally-ventilated double skin facades. *Energy Procedia*(48), 1254-1261.
- Gaillard, L., Giroux-Julien, S., Ménézo, C., & Pabiou, H. (2014). Experimental evaluation of a naturally ventilated PV double-skin building envelope in real operating conditions. *Solar Energy*(103), 223-241.
- Gan, G. (2009). Effect of air gap on the performance of building-integrated photovoltaics. *Energy*(34), 913-921.
- Gautam, K. R., & Andresen, G. B. (2017). Performance comparison of building-integrated combined photovoltaic thermal solar collectors (BiPVT) with other building-integrated solar technologies. *Solar Energy*, 155, 93-102.

- Ghorab, M., Entchev, E., & Yang, L. (2017). Inclusive analysis and performance evaluation of solar domestic hot water system (a case study). *AEJ - Alexandria Engineering Journal*, 56(2).
- Ghosh, A., Sundaram, S., & Mallick, T. K. (2019). Colour properties and glazing factors evaluation of multicrystalline based semi-transparent Photovoltaic-vacuum glazing for BIPV application. *Renewable Energy*(131), 730-736.
- Gorjian, S., Ebadi, H., Najafi, G., Chandel, S. S., & Yildizhan, H. (2021). Recent advances in net-zero energy greenhouses and adapted thermal energy storage systems. *Sustainable Energy Technologies and Assessments*, 43.
- Guarino, F., Cassara, P., Longo, S., Cellura, M., & Ferro, E. (2015). Load match optimisation of a residential building case study: A cross-entropy based electricity storage sizing algorithm. *Applied Energy*, 154, 380-391.
- Hailu, G., Dash, P., & Fung, A. (2015). Performance Evaluation of an Air Source Heat Pump Coupled with a Building-Integrated Photovoltaic/Thermal (BIPV/T) System under Cold Climate Conditions. *Energy Procedia*(78), 1913-1918.
- Han, J., Lu, L., & Yang, H. (2010). Numerical evaluation of the mixed convective heat transfer in a double-pane window integrated with see-through a-Si PV cells with low-e coatings. *Applied Energy*, 87(11), 3431-3437.
- Han, J., Lu, L., Peng, J., & Yang, H. (2013). Performance of ventilated double-sided PV façade compared with conventional clear glass façade. *Energy and Buildings*, 56, 204-209.
- Hassanien, R. H., Li, M., & Tang, Y. (2018). The evacuated tube solar collector assisted heat pump for heating greenhouses. *Energy and Buildings*, 169, 305-318.
- Hollands, T., Unny, T., Raithby, G., & Konicek, L. (1976). Free Convection Heat Transfer Across Inclined Air Layers. *Journal of Heat Transfer*, 189-193.
- Hydro Quebec. (2019). *2019 Electricity Rates*. Quebec: Hydro Quebec.
- Incropera, F., Dewitt, D., Bergman, T., & Lavien, A. (2011). *Fundamentals of Heat and Mass Transfer* (7th ed.). Jefferson: John Wiley & Sons, Inc.
- Ioannidis, Z., Kapsis, K., Buonomano, A., Athienitis, A., Rounis, E. D., & Stathopoulos, T. (2017). Experimental Comparison on the Energy Performance of Semi-Transparent PV Facades Under Continental Climate. *IEA SHC International Conference on Solar Heating and Cooling for Buildings and Industry*. Montreal.
- Jabir, H. J., Teh, J., Ishak, D., & Abunima, H. (2018). Impacts of Demand-Side Management and Electrical Power Systems: A Review. *Energies*, 11.
- Jian, Z., He, Z., Jia, J., & Xie, Y. (2013). A Review of Control Strategies for DC Micro-grid. *2013 Fourth International Conference on Intelligent Control and Information Processing (ICICIP)* . Beijing, China.

- Jordehi, A. R. (2019). Optimisation of demand response in electric power systems, a review. *Renewable and Sustainable Energy Reviews*, 103, 308-319.
- Kamel, R. S., & Fung, A. S. (2014). Modeling, simulation and feasibility analysis of residential BIPV/T+ASHP system in cold climate—Canada. *Energy and Buildings*(82), 758-770.
- Kamel, R., Ekrami, N., Dash, P., Fung, A., & Hailu, G. (2015). BIPV/T+ASHP: Technologies for NZEBs. *Energy Procedia*(78), 424-429.
- Kamel, R., Fung, A., & Dash, P. (2015). Solar systems and their integration with heat pumps: A review. *Energy and Buildings*(87), 395-412.
- Kapsis, K. (2016). *Modelling, Design and Experimental Study of Semi-Transparent Photovoltaic Windows for Commercial Building Applications*. Montreal: Concordia University.
- Karthick, A., Murugavel, K. K., & Kalaivani, L. (2018). Performance analysis of semitransparent photovoltaic module for skylights. *Energy*(162), 798-812.
- Kasaeian, A., Khanjari, Y., Golzari, S., Mahian, O., & Wongwises, S. (2017). Effects of forced convection on the performance of a photovoltaic thermal system: An experimental study. *Experimental Thermal and Fluid Science*, 85, 13-21.
- Khaki, M., Shahsavari, A., Khanmohammadi, S., & Salmanzadeh, M. (2017). Energy and exergy analysis and multi-objective optimization of an air based building integrated photovoltaic/thermal (BIPV/T) system. *Solar Energy*, 158, 380-395.
- Larson, B., & Kvaltine, N. (2015). *Laboratory Assessment of Demand Response Characteristics of Two CO2 Heat Pump Water Heaters*. Ecotope inc.
- Larson, B., Logston, M., & Baylon, D. (2011). *Residential Heat Pump Water Heater Evaluation: Lab Testing & Energy Use Estimates*. Seattle, USA: Ecotope, inc.
- Li, D. H., Lam, T. N., & Cheung, K. (2009). Energy and cost studies of semi-transparent photovoltaic skylight. *Energy Conversion and Management*(50), 1981-1990.
- Li, S., Joe, J., Hu, J., & Karava, P. (2015). System identification and model-predictive control of office buildings with integrated photovoltaic-thermal collectors, radiant floor heating and active thermal storage. *Solar Energy*, 113, 139-157.
- Lim, T., Baik, Y.-K., & Kim, D. D. (2020). Heating Performance Analysis of an Air-to-Water Heat Pump Using Underground Air for Greenhouse Farming. *Energies*, 13, 3863.
- Lioa, W., & Xu, S. (2015). Energy performance comparison among see-through amorphous-silicon PV (Photovoltaic) glazings and traditional glazings under different architectural conditions in China. *Energy*(83), 267-275.
- Liu, D., Sun, Y., Wilson, R., & Wu, Y. (2020). Comprehensive evaluation of window-integrated semi-transparent PV for building daylight performance. *Renewable Energy*(145), 1399-1411.

- Lizana, J., Friedrich, D., Renaldi, R., & Chacartegui, R. (2018). Energy flexible building through smart demand-side management and latent heat storage. *Applied Energy*(230), 471-485.
- Lu, L., & Law, K. M. (2013). Overall energy performance of semi-transparent single-glazed photovoltaic (PV) window for a typical office in Hong Kong. *Renewable Energy*(49), 250-254.
- Luo, Y., Zhang, L., Liu, Z., Xie, L., Wang, X., & Wu, J. (2018). Experimental study and performance evaluation of a PV-blind embedded double skin façade in winter season. *Energy*, 165, 326-342.
- Lynn, N., & Mohanty, L. (2012). Color rendering properties of semi-transparent thin-film PV modules. *Building Environemnt*(54), 148-158.
- Marrec, J. (2019). *Set Site Water Mains Temperature*. (NREL) Retrieved February 2020, from <https://bcl.nrel.gov/node/83628>
- Martin-Escudero, K., Salazar-Herran, E., Campos-Celador, A., Diarce-Belloso, G., & Gomez-Arriaran, I. (2019). Solar energy system for heating and domestic hot water supply by means of a heat pump coupled to a photovoltaic ventilated façade. *Solar Energy*(183), 453-462.
- Marwan, M., & Kamel, F. (2011). Demand Side Response to Mitigate Electrical Peak Demand in Eastern and Southern Australia. *Energy Procedia*, 12, 133-142.
- McLaughlin, D. V., Kapsis, K., Athienitis, A., Siassi, S., & Nichilo, L. (2014). Analysis of Building Envelope Performance effects of an Insulating Semi-transparent Photovoltaic (STPV) Glazing Unit. *Proceedings of the ASME 2014 International Mechanical Engineering Congress and Exposition*. Montreal.
- Miyazaki, T., Akisawa, A., & Kashiwagi, T. (2005). Energy savings of office buildings by the use of semi-transparent solar cells for windows. *Renewable Energy*(30), 281-304.
- Naghibi, Z., Carriveau, R., & Ting, D. S.-K. (2020). Improving clean energy greenhouse heating with solar thermal energy storage and phase change materials. *Energy Storage*, 2.
- Nash, A., Badithela, A., & Jain, N. (2017). Dynamic modeling of a sensible thermal energy storage tank with an immersed coil heat exchanger under three operation modes. *Applied Energy*, 195, 877-889.
- National Renewable Energy Laboratory. (2020). *Best Research-Cell Efficiency Chart*. (U.S. Department of Energy) Retrieved January 2020, from <https://www.nrel.gov/pv/cell-efficiency.html>
- National Research Council of Canada. (2015). *National Building Code of Canada 2015*. Ottawa: National Research Council of Canada.

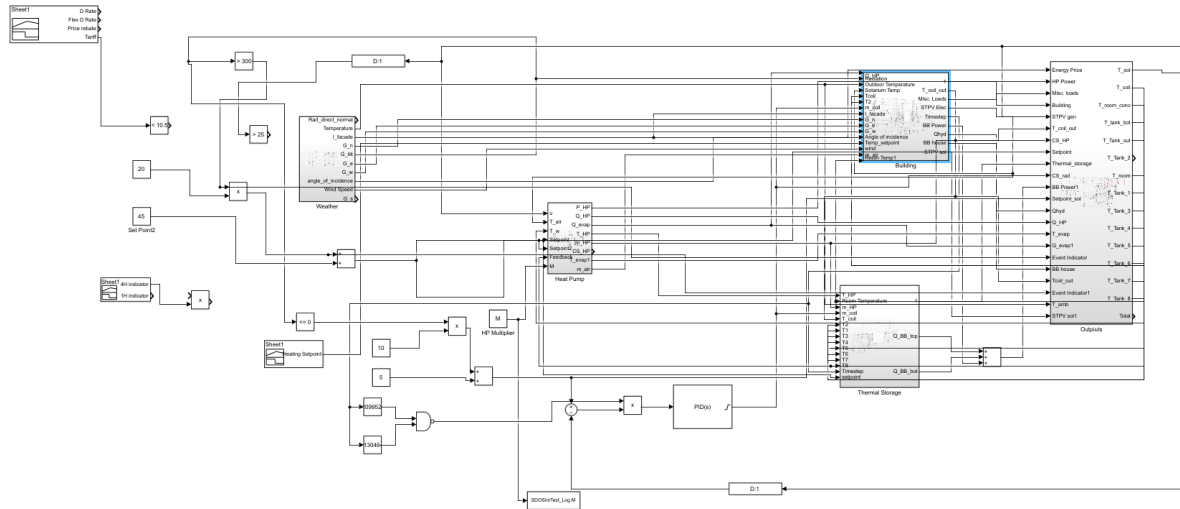
- Newsham, G., & Bowker, B. (2010). The effect of utility time-varying pricing and load control strategies on residential summer peak electricity use: A review. *Energy Policy*, 38(7), 3289-3296.
- Ng, P. K., Mithraratne, N., & Kua, H. W. (2013). Energy analysis of semi-transparent BIPV in Singapore buildings. *Energy and buildings*(66), 274-281.
- Office of Energy Efficiency. (2014). *Energy Efficiency trends in Canada*. Ottawa, Canada: Natural Resources Canada.
- Ontario Energy Board. (2020). *Historical electricity rates*. Retrieved May 2020, from <https://www.oeb.ca/rates-and-your-bill/electricity-rates/historical-electricity-rates>
- Ontario Energy Board. (2020). *Managing costs with time-of-use rates*. Retrieved May 2020, from <https://www.oeb.ca/rates-and-your-bill/electricity-rates/managing-costs-time-use-rates>
- Ozgener, O., & Hepbasli, A. (2005). Experimental performance analysis of a solar assisted ground-source heat pump greenhouse heating system. *Energy and Buildings*, 37, 101-110.
- Palyvos, J. (2008). Survey of wind convection coefficient correlations for building envelop energy systems' modeling. *Applied Thermal Engineering*, 28, 801-808.
- Park, K., Kang, G., Kim, H., Yu, G., & Kim, J. (2010). Analysis of thermal and electrical performance of semi-transparent photovoltaic (PV) module. *Energy*(35), 2681-2687.
- Patteeuw, D., Henze, G., & Helsen, L. (2016). Comparison of load shifting incentives for low-energy buildings with heat pumps to attain grid flexibility benefits. *Applied Energy*, 167, 80-92.
- Peng, J., Curcija, D., Lu, L., Selkowitz, S., Yang, H., & Zhang, W. (2016). Numerical investigation of the energy saving potential of a semi-transparent photovoltaic double-skin facade in a cool-summer Mediterranean climate. *Applied Energy*, 165, 345-356.
- Rahman, A., Fumo, N., & Smith, A. (2015). Simplified modeling of thermal storage tank for distributed energy heat recovery applications. *ASME 2015 9th International Conference on Energy Sustainability, ES 2015, collocated with the ASME 2015 Power Conference, the ASME 2015 13th International Conference on Fuel Cell Science, Engineering and Technology, and the ASME 2015 Nuclear Forum. 2*. American Society of Mechanical Engineers.
- Rashmi, Tiwari, A., Tiwari, G., & Bhatti, T. (2019). Performance evaluation of a semi-transparent photovoltaic thermal (SPVT) inverted absorber flat plate collector (IAFPC) for constant collection temperature (CCT) mode. *Solar Energy*(186), 382-391.
- Renaldi, R., Kiprakis, A., & Friedrich, D. (2017). An optimisation framework for thermal energy storage integration in a residential heat pump heating system. *Applied Energy*(186), 520-529.

- Robinson, L., & Athienitis, A. (2009). Design methodology for optimization of electrical generation and daylight utilization for façade with semi-transparent photovoltaics. *Eleventh international IBPSA Conference*. Glasgow.
- Rounis, E. D. (2018). *Modelling and Design Methodology for Air-based Building Integrated Photovoltaic/Thermal Systems including Thermal Enhancements and Wind Effects*. Montreal: Concordia University.
- Sager, J., Mackintosh, T., St-Onge, G., McDonald, E., & Kegel, M. (2018). Detailed performance Assessment of Variable Capacity Inverter-Driven Cold-Climate Air Source Heat Pumps. *Cold Climate HVAC Conference*. Sweden.
- Saloux, E., & Candanedo, J. (2018). Control-oriented modelling of stratified storage tanks: an enhanced approach. *eSim*. Montreal, Canada.
- Schuetz, P., Gwerder, D., Gasser, L., Fischer, L., Wellig, B., & Worlitschek, J. (2017). Thermal storage improves flexibility of residential heating systems for smart grids. *12th IEA Heat Pump Conference 2017*. Rotterdam.
- Simple, L., Carriveau, R., & Ting, D. S.-K. (2017). A techno-economic analysis of seasonal thermal energy storage for greenhouse applications. *Energy and Buildings*, 154, 175-187.
- Shahsavari, A., & Khanmohammadi, S. (2019). Feasibility of a hybrid BIPV/T and thermal wheel system for exhaust air heat recovery: Energy and exergy assessment and multi-objective optimization. *Applied Thermal Engineering*, 146, 104-122.
- Shariatzadeh, F., Mandal, P., & Srivastava, A. K. (2015). Demand response for sustainable energy systems: A review, application and implementation strategy. *Renewable and Sustainable Energy Reviews*, 45, 343-350.
- Shuxue, X., & Guoyuan, M. (2017). Performance Evaluation of a Vapor Injection Refrigeration System Using Mixture Working Fluid R32/R1234ze. *12th IEA Heat Pump Conference 2017*. Rotterdam: 12th IEA Heat Pump Conference 2017.
- Sioshansi, F. P. (2011). So What's So Smart about the Smart Grid? *The Electricity Journal*, 24(10), 91-99.
- Sun, W., Ji, J., Luo, C., & He, W. (2011). Performance of PV-Trombe wall in winter correlated with south façade design. *Applied Energy*, 86(1), 224-231.
- Tello-Oquendo, F. M., Navarro-Peris, E., & González-Maciá, J. (2019). Comparison of the performance of a vapor-injection scroll compressor and a two-stage scroll compressor working with high pressure ratios. *Applied Thermal Engineering*, 160, 114023.
- Thür, A., Calabrese, T., & Streicher, W. (2018). Smart grid and PV driven ground heat pump as thermal battery in small buildings for optimized electricity consumption. *Solar Energy*(174), 273-285.

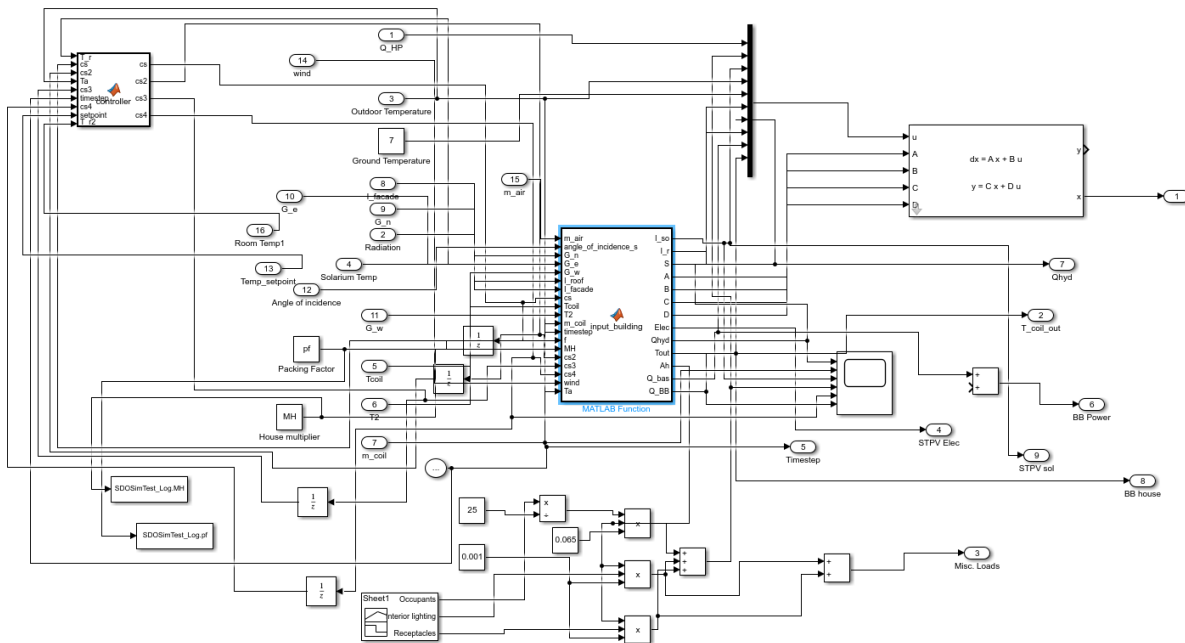
- Tiwari, A., & Sodha, M. (2007). Parametric study of various configurations of hybrid PV/thermal air collector: Experimental validation of theoretical model. *Solar Energy Materials and Solar Cells*, 91, 17-28.
- Tonui, J., & Tripanagnostopoulos, Y. (2007). Improved PV/T solar collectors with heat extraction by forced or natural air circulation. *Renewable Energy*, 32, 623-637.
- Tsai, H.-L. (2015). Modeling and validation of refrigerant-based PVT-assisted heat pump water heating (PVT-HPWH) system. *Solar Energy*, 122, 36-47.
- Tsai, H.-L., Hsu, C.-Y., & Yang, C.-Y. (2013). Design and performance evaluation of building integrated PVT and heat pump water heating (BIPVT/HPWH) system. *IEEE 39th Photovoltaic Specialists Conference (PVSC)*. Tampa.
- Tyagi, V., Kaushik, S., & Tyagi, S. (2012). Advancement in solar photovoltaic/thermal (PV/T) hybrid collector technology. *Renewable and Sustainable Energy Reviews*, 16, 1383-1398.
- Underwood, C., Royapoor, M., & Sturm, B. (2017). Parametric modelling of domestic air-source heat pumps. *Energy and Buildings*, 139, 578-589.
- University of Wisconsin. (2017). *Transient System Simulation Tool* (18 ed.). Madison, Wisconsin: Solar Energy Laboratory.
- Vandewalle, J., Keyaerts, N., & D'haeseleer, W. (2012). The role of thermal storage and natural gas in a smart energy system. *2012 9th International Conference on the European Energy Market*. Florence.
- Vats, K., & Tiwari, G. (2012). Performance evaluation of a building integrated semitransparent photovoltaic thermal system for roof and facade. *Energy and Buildings*(45), 211-218.
- Vats, K., Tomar, V., & Tiwari, G. (2012). Effect of packing factor on the performance of a building integrated semitransparent photovoltaic thermal (BISPVT) system with air duct. *Energy and Buildings*(53), 159-165.
- Wang, M., Peng, J., Li, N., Yang, H., Wang, C., Li, X., & Lu, T. (2017). Comparison of energy performance between PV double skin facades and PV insulating glass units. *Applied Energy*(194), 148-160.
- Wong, P., Shimoda, Y., Nonaka, M., Inoue, M., & Mizuno, M. (2008). Semi-transparent PV: Thermal performance, power generation, daylight modelling and energy saving potential in a residential application. *Renewable Energy*(33), 1024-1036.
- Yan, C., Xue, X., Wang, S., & Cui, B. (2015). A novel air-conditioning system for proactive power demand response to smart grid. *Energy Conversion and Management*(102), 239-546.
- Yang, L., Zhao, L.-X., Zhang, C.-L., & Gu, B. (2009). Loss-efficiency model of single and variable-speed compressors using neural networks. *International Journal of Refrigeration*, 32, 1423-1432.

- Yang, S.-H., & Rhee, J. Y. (2013). Utilization and performance evaluation of a surplus air heat pump system for greenhouse cooling and heating. *Applied Energy*, *105*, 244-251.
- Yang, T. (2015). *A Numerical and Experimental Investigation of Enhanced Open-Loop Air-Based Building-Integrated Photovoltaic/Thermal (BIPV/T) Systems*. Montreal: Concordia University.
- Yang, T., & Athienitis, A. (2014). A study of design options for a building integrated photovoltaic/thermal (BIPV/T) system with glazed air collector and multiple inlets. *Solar Energy*, *104*, 82-92.
- Zhang, L., Good, N., & Mancarella, P. (2019). Building-to-grid flexibility: Modelling and assessment metrics for residential demand response from heat pump aggregations. *Applied Energy*, *233-234*, 709-723.
- Zhang, S., Guo, Y., Zhao, H., Wang, Y., Chow, D., & Fang, Y. (2020). Methodologies of control strategies for improving energy efficiency in agricultural greenhouses. *Journal of Cleaner Production*, *274*, 122695.
- Zhang, X., Zhao, X., Smith, S., Xu, J., & Yu, X. (2012). Review of R&D progress and practical application of the solar photovoltaic/thermal (PV/T) technologies. *Renewable and Sustainable Energy Reviews*, *16*, 599-617.
- Zondag, H., & Helden, W. v. (2003). PV-thermal domestic systems. *3rd World Conference on Photovoltaic Energy Conversion*. Osaka, Japan.

Appendix A: Programming Code



MATLAB Code: Building Model



```
function [I_so,I_r,S,A,B,C,D,Elec,Q_hyd,Tout,Ah,Q_bas,Q_BB] =
input_building(m_air,angle_of_incidence_s,G_n,G_e,G_w,I_roof,I_facade,cs,Tcoil,T2,m_c
oil,timestep,f,MH,cs2,cs3,cs4,wind,Ta)
```

```
%%%%%%%%%%
%%%%%%%%%%/%%%%%%%%%%/%%%%%%%%%%/%%%%%%%%%%/%%%%%%%%%%/%%%%%%%%%%/%%%%%%%%%%/
%Building dimensions in m
```

```
%%%%%%%%%%%%%%%%%%%%%%%%%%%%%%%%%%%%%%%%%%%%%%%%%%%%%%%%%%%%%%%%%%%%%%%%
```

```
%Solarium
```

```
H_s=3.048;  
L_s=7.146/2*MH;  
W_s=3.145*MH;  
As_floor=L_s*W_s;  
As_roof=As_floor;  
As_front=L_s*H_s;  
As_side=W_s*H_s;
```

```
ACH_s=1;
```

```
%Building Room
```

```
H=7.832;  
H_slope=3.884;  
W_slope=3.812;  
L=14.703;  
W=7.904;  
Ah=L*W-As_floor;  
Ah_front_n=H*L;  
Ah_front_s=(L*(H-H_slope)-As_front)+((H_slope^2+W_slope^2)^(1/2))*L;  
Ah_side=W*(H-H_slope)+((H_slope*W_slope)/2)+(W-W_slope)*H_slope;  
Ah_back=Ah_front_n;  
Ha=3.884;  
Ah_ex=Ah_front_n+Ah_front_s+Ah_side*2+Ah_back;
```

```
ACH=0.5;
```

```
%%%%%%%%%%%%%%%%%%%%%%%%%%%%%%%%%%%%%%%%%%%%%%%%%%%%%%%%%%%%%%%%%%%%%%%%
```

```
%Properties
```

```
%%%%%%%%%%%%%%%%%%%%%%%%%%%%%%%%%%%%%%%%%%%%%%%%%%%%%%%%%%%%%%%%%%%%%%%%
```

```
%Concrete
```

```
row_c=2200; %density in kg/m3  
k_conc=1.7; %thermal conductance mK/W  
cp_c=800; %specific capacity in J/kgK  
t_c=0.2; %thickness of the slab in m  
R_ins=20;
```

```
%air
```

```
row_a=1.225;  
cp_a=1000;  
h_i=6.77;  
h_o=30/3.6;
```

```
%Shades characteristics
```

```
tau_blind=0.05;  
alpha_blind=0.5;  
A_blind=As_front;
```

```
R_g=(1/2)*1.25; %both in the case of double glazed windows with and without PV
```

```
A_eff=(As_front)/2;
```

```
A_sw=H_s*L_s;  
U_wall=3;  
R_ex=3.5;  
% WWR_s=0.3;  
WWR_ew=0.2;  
WWR_n=0.1;  
La=sqrt(Ha^2+W^2);  
Ah_exa=L*La^2+Ha*W;  
A_win=10;  
A_eff2=(As_front)/2-A_win;
```

```
U_ra=1/(1/Ah/h_i+1/(U_wall*Ah))/1000;  
U_ao=1/(1/(Ah_exa*h_o)+1/(Ah_exa*h_i)+R_ex/Ah_exa)/1000;  
U_eff=1/(1/(A_eff2*h_o)+1/(A_eff2*h_i)+R_g/A_win)/1000;  
U_ro=1/(1/(Ah_ex*h_o)+1/(Ah_ex*h_i)+R_ex/Ah_ex+R_g/((Ah_side*WWR_ew)*2+Ah_front_n*WWR_n))/1000;  
U_airw=1/(1/(A_eff*h_i)+1/(U_wall*A_sw))/1000;  
U_airf=1/(1/(A_eff*h_i))/1000;  
U_r2=U_airf;  
U1g=1/(((t_c+0.1))/(k_conc*As_floor)+R_ins/As_floor)/1000/2;  
U2g=1/(((t_c+0.1))/(k_conc*Ah)+R_ins/Ah)/1000;
```

```
A_12=As_side;  
U12=1/(1/(A_12*h_i)+1/(U_wall*A_12))/1000;  
U2g_s=1/(((t_c+0.1))/(k_conc*As_floor)+R_ins/As_floor)/1000/2;  
U_eff2=1/(1/(A_eff2*h_o)+1/(A_eff2*h_i)+R_g/A_win)/1000;
```

```
Ceff=((L_s*W_s*H_s)/2)*row_a*cp_a/1000*3;  
C1=(t_c+0.1)*As_floor*row_c*cp_c/1000/2*3;  
Ceff_2=((L_s*W_s*H_s)/2)*row_a*cp_a/1000*3;  
C2_s=(t_c+0.1)*As_floor*row_c*cp_c/1000/2*3;  
A_f=4; %area of window exposed to sunlight  
% A_f=Ah_back*WWR_s; %area of window exposed to sunlight  
A_fn=Ah_back*WWR_n;  
A_fw=Ah_side*WWR_ew;
```

```

A_fe=Ah_side*WWR_ew;
C2=t_c/2*Ah*row_c*cp_c/1000;
Cenv=(L*H*W)*row_a*cp_a/1000*10;
Ca=(L*Ha*W)*row_a*cp_a/1000*10/2;

V=H_s*L_s*W_s;
diameter=1;%8/39.37; %8in hole in the wall
Ainf=pi*((diameter/2)^2)*2;
v=m_air/3600/row_a/Ainf;
ACH_opening=v*Ainf*3600/V;

U_inf_opening=ACH_opening/3600*L_s*W_s*H_s/2*row_a*cp_a/1000*0;
U_inf=ACH/3600*L*H*W*row_a*cp_a/1000;
U_infs=ACH_s/3600*((H_s)*W_s*L_s/2)*row_a*cp_a/1000;
U_inf_a=ACH_s/3600*L*H*W*row_a*cp_a/1000/2;

% f=0.6; %packing factor
rated_power=5.25;
eff=0.15;
A_total=rated_power/(1*eff*f);
if A_total>As_roof
A_STPV=As_roof;
A_total=(rated_power-A_STPV*1*eff*f)/(1*eff);
A_BIPV=A_total-A_STPV;
else
A_STPV=As_roof;
A_BIPV=0;
end
% A_BIPV=25;
% A_STPV=10;
alpha_stpv=1-f-0.1;

%section for STPV
tau11=0.8*f;
tau22=0.8;
rowf22=0.1;
rowb11=0.1;
rowb22=0.1;
rowf11=0.1;
rowf32=0.2;

tau=tau11*tau22/(1-rowf22*rowb11);
rowf=rowf11+(tau^2)*(rowf22^2)/(1-rowf22*rowb11);
rowb=rowb11+(tau^2)*(rowb22^2)/(1-rowf22*rowb11);
alpha=(tau11*(1-tau22-rowf22)+tau*rowf32*(1-tau22-rowb22))/(1-rowf22*rowb11);

```

```

%King's model for electrical production (ASHRAE)
temp_coef=-0.00261;

%for a double glazing BIPV window
a=-2.85;
b=-0.0351;
dT=9;
T_back=I_facade*exp(a+b*wind)+Ta;
Tcell=T_back+I_facade/1000*dT;
Elec_STPV=eff*(1+temp_coef*(Tcell-25))*I_facade*A_STPV*f;

temp_coef=-0.0035;
%for BIPV with medium ventilation
a=-2.81;
b=-0.0455;
dT=0;
T_back=I_roof*exp(a+b*wind)+Ta;
Tcell=T_back+I_roof/1000*dT;
Elec_BIPV=eff*(1+temp_coef*(Tcell-25))*I_roof*A_BIPV;

% Elec_STPV=I_roof*A_STPV/1000*f*eff;
% Elec_BIPV=I_roof*A_BIPV/1000*eff;
Elec=(Elec_STPV+Elec_BIPV)/1000;

%Non STPV wndows
tau11=0.8;
tau22=0.8;
rowf22=0.1;
rowb11=0.1;
rowb22=0.1;
rowf11=0.1;
rowf32=0.2;

tau=tau11*tau22/(1-rowf22*rowb11);
rowf=rowf11+(tau^2)*(rowf22^2)/(1-rowf22*rowb11);
rowb=rowb11+(tau^2)*(rowb22^2)/(1-rowf22*rowb11);
alpha=(tau11*(1-tau22-rowf22)+tau*rowf32*(1-tau22-rowb22))/(1-rowf22*rowb11);

I_so=tau*I_facade*A_win/1000*(1-cs)*(1-f-0.05);
S=(1-cs)*alpha*I_facade*A_f/1000+(cs)*alpha_blind*I_facade*A_blind/1000*alpha;

k1=0.02;
ng=1.53;
%angle of refraction
refraction=asind((sind(angle_of_incidence_s)/ng));

```

```

reflectivity=(1/2)*((sind(angle_of_incidence_s-
refraction)/sind(angle_of_incidence_s+refraction))^2+(tand(angle_of_incidence_s-
refraction)/tand(angle_of_incidence_s+refraction))^2);

```

```

a=exp(-k1/(sqrt(1-(sind(angle_of_incidence_s)/ng)^2)));
tau_it=(((1-reflectivity)^2)*a)/(1-(reflectivity^2)*(a^2));
row_it=reflectivity+(reflectivity*((1-reflectivity)^2)*(a^2))/(1-
(reflectivity^2)*(a^2));
alpha_it=1-row_it-tau_it;

```

```

% tau11=0.8;
% rowb11=0.1;

```

```

tau=(tau_it^2)/(1-row_it^2);

```

```

tau_t=(tau_it^3)/(1-row_it^3);

```

```

alpha_i=alpha_it*tau_it/(1-(row_it)^2);
alpha_o=alpha_it+alpha_it*tau_it*row_it/(1-(row_it)^2);

```

```

A_room=5;
I_s=tau*I_facade*A_room/1000;
I_n=tau*G_n*A_fn/1000;
I_w=tau*G_w*A_fw/1000;
I_e=tau*G_e*A_fe/1000;

```

```

I=I_n+I_w+I_e+I_s;

```

```

tau_shade_o=0.9;

```

```

shadefactor=tau_shade_o;

```

```

S_s=0.3*I*A_room/(A_room+A_fn+A_fw+A_fe)*shadefactor;
S_n=0.3*I_n*A_fn/(A_room+A_fn+A_fw+A_fe)*shadefactor;
S_w=0.3*I_w*A_fw/(A_room+A_fn+A_fw+A_fe)*shadefactor;
S_e=0.3*I_e*A_fe/(A_room+A_fn+A_fw+A_fe)*shadefactor;
S_floor=0.7*I*shadefactor;
I_r=S_n+S_w+S_e+S_floor+S_s;

```

```

if isnan(I_r)
I_r=0;

```

```

end

%x=[Ts T1]
%u=[Qhp Qint Qsol Tr To Tg S]
% A=[-(U_eff+U_airf+U_airw)/Ceff (U_airf)/Ceff;U_airf/C1 -(U_airf+U1g)/C1];
% B=[-1/Ceff 1/Ceff 0 U_airw/Ceff U_eff/Ceff 0 1/Ceff;0 0 1/C1 0 0 U1g/C1 0];
% C=[1 0;0 1];
% D=[0 0 0 0 0 0;0 0 0 0 0 0];

cp_w=4.19;
n_c=13; %number of circuits
cmin=min(m_coil*cp_w,C2/timestep*3600/n_c);
cmin=m_coil*cp_w;
Qhyd=cmin*(Tcoil-T2)/3600*n_c;
if m_coil==0
    Tout=Tcoil;
else
    Tout=Tcoil-Qhyd/cmin*3600/n_c;
    m_coil=m_coil*0.00000028;
end
c=4200;
% delta_T=(0.0524*(Tcoil*9/5+32)-3.2566)*5/9;
delta_T=(0.0976*(Tcoil)-1.9563);
Qhyd=m_coil*1000*c*(delta_T)/1000;
% Qhyd=Qhyd*(m+coil^0.04)*0.00096865*(delta_T/2-T2-5)^1.4172;
Tout= Tcoil-delta_T-5;

% delta_T=(0.0524*(Tout*9/5+32)-3.2566)*5/9;
% delta_T=(0.1252*(Tout)-2.505);
% Qhyd2=m_coil*1000*c*(delta_T)/1000;
% Tout=Tout-delta_T;
%
% Qhyd=Qhyd+Qhyd2;

U_mot=5/3600*((L_s*W_s*H_s)/2)*row_a*cp_a/1000*cs3; % gain from motorized windows in
the summer
Q_bas=cs2*2; %baseboard heater for the solarium - 2 kW
Q_BB=cs4*10; %baseboard heater for the house - 10 kW
%radiatiant floor
%x=[Ts_1 Ts_2 T1 T2_s Tr T2]
%u=[Qhp Qint Qsol To Tg S Qhyd Qsol_r Q_bas Q_BB]
U_m=210/3600*cp_a/1000;
a=1; %1 = heat pump dumping cold back to the room, 0 = dump air outside

%Experimental Verification Building Model

```

```

A=[-(U_eff+U_airf+U_airw+U_infs+U_mot+U12+U_inf_opening)/Ceff
(U12+U_inf_opening)/Ceff (U_airf)/Ceff 0 U_airw/Ceff 0;
(U12+U_inf_opening)/Ceff_2 -
(U_eff2+U_airf+U_airw+U_infs+U_mot+U12+U_inf_opening+U_m*(1-a))/Ceff_2 0
(U_airf)/Ceff_2 U_airw/Ceff_2 0;
U_airf/C1 0 -(U_airf+U1g)/C1 0 0 0;
0 U_airf/C2_s 0 -(U_airf+U2g_s)/C2_s 0 0;
U_airw/Cenv U_airw/Cenv 0 0 -(U_airw+U_ro+U_r2+U_inf+U_ra)/Cenv U_r2/Cenv;
0 0 0 U_r2/C2 -(U_r2+U2g)/C2];
% 0 0 0 U_ra/Ca 0 -(U_ra+U_ao+U_infa)/Ca];

B=[0 0 0 (U_eff+U_infs+U_mot)/Ceff 0 1/Ceff 1/Ceff 0 0 0;
-1/Ceff_2*a 0 0 (U_eff2+U_infs+U_mot+U_m*(1-a))/Ceff_2 0 1/Ceff_2 0 0 1/Ceff_2 0;
0 0 1/C1/2 0 U1g/C1 0 0 0 0 0;
0 0 1/C2_s/2 0 U2g_s/C2_s 0 0 0 0 0;
0 1/Cenv 0 (U_ro+U_inf)/Cenv 0 0 0 1/Cenv 0 1/Cenv;
0 0 0 0 U2g/C2 0 0 1/C2 0 0];
% 0 0 0 (U_ao+U_infa)/Ca 0 0 0 0 0 0];

C=[1 0 0 0 0 0;0 1 0 0 0 0;0 0 1 0 0 0;0 0 0 1 0 0;0 0 0 0 1 0;0 0 0 0 0 1 ];
D=[0 0 0 0 0 0 0 0 0 0;0 0 0 0 0 0 0 0 0 0;0 0 0 0 0 0 0 0 0 0;0 0 0 0 0 0 0 0 0 0;0
0 0 0 0 0 0 0 0 0 0];

%Simulation Building Model
%A=[-(U_eff+U_airf+U_airw+U_infs+U_mot)/Ceff (U_airf)/Ceff U_airw/Ceff 0 0;
% U_airf/C1 -(U_airf+U1g)/C1 0 0 0;
% U_airw/Cenv 0 -(U_airw+U_ro+U_r2+U_inf+U_ra)/Cenv U_r2/Cenv U_ra/Cenv;
% 0 0 U_r2/C2 -(U_r2+U2g)/C2 0]
% 0 0 U_ra/Ca 0 -(U_ra+U_ao+U_infa)/Ca];

%B=[1/Ceff 0 0 (U_eff+U_infs+U_mot)/Ceff 0 1/Ceff 0 0 1/Ceff 0;
% 0 0 1/C1 0 U1g/C1 0 0 0 0 0;
% 0 1/Cenv 0 (U_ro+U_inf)/Cenv 0 0 0 0 0 1/Cenv;
% 0 0 0 0 U2g/C2 0 1/C2 1/C2 0 0]
% 0 0 0 (U_ao+U_infa)/Ca 0 0 0 0 0 0];

%C=[1 0 0 0 ;0 1 0 0 ;0 0 1 0 ;0 0 0 1 ];
%D=[0 0 0 0 0 0 0 0 0 0;0 0 0 0 0 0 0 0 0 0;0 0 0 0 0 0 0 0 0 0;0 0 0 0 0 0 0 0 0 0];

%
% A=[-(U_eff+U_airf+U_airw+U_infs+U_mot+U_m*(1-a)+U12+U_inf_opening)/Ceff
(U12+U_inf_opening)/Ceff (U_airf)/Ceff 0 U_airw/Ceff 0;
% (U12+U_inf_opening)/Ceff_2 -
(U_eff2+U_airf+U_airw+U_infs+U_mot+U12+U_inf_opening)/Ceff_2 0 (U_airf)/Ceff_2
U_airw/Ceff_2 0;
% U_airf/C1 0 -(U_airf+U1g)/C1 0 0 0;
% 0 U_airf/C2_s 0 -(U_airf+U2g_s)/C2_s 0 0;

```

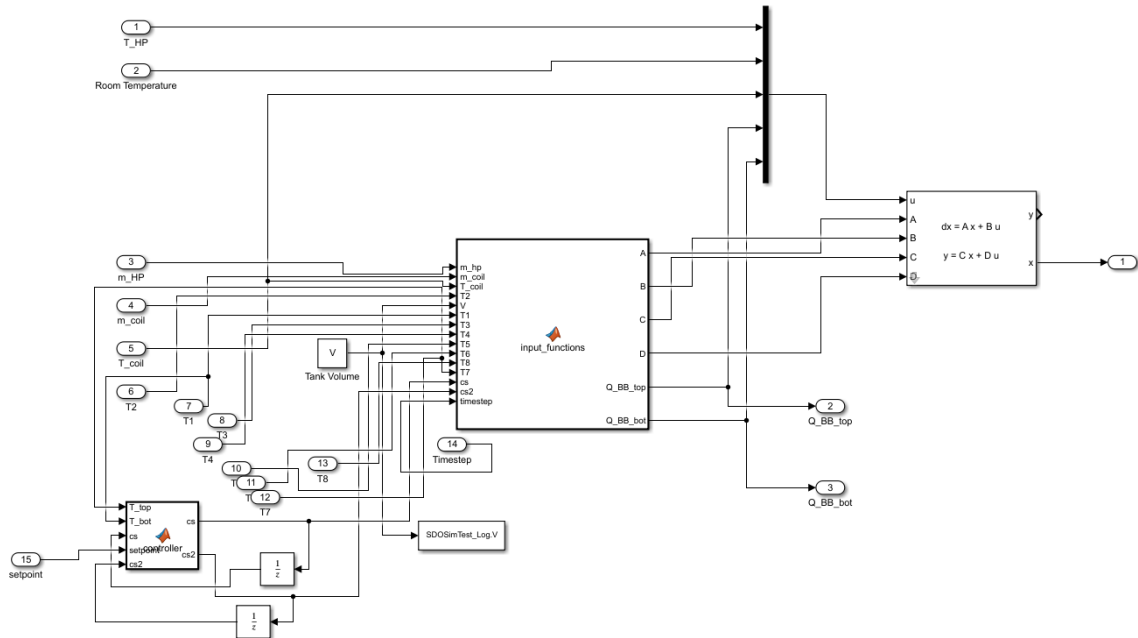
```

%      U_airw/Cenv U_airw/Cenv 0 0 -(U_airw+U_ro+U_r2+U_inf+U_ra)/Cenv U_r2/Cenv;
%      0 0 0 U_r2/C2 -(U_r2+U2g)/C2];
% %      0 0 0 U_ra/Ca 0 -(U_ra+U_ao+U_infa)/Ca];
%
% B=[0 0 0 (U_eff+U_infs+U_mot+U_m*(1-a))/Ceff 0 1/Ceff 1/Ceff 0 0 0;
%      -1/Ceff_2*a 0 0 (U_eff2+U_infs+U_mot)/Ceff_2 0 1/Ceff_2 0 0 1/Ceff_2 0;
%      0 0 1/C1/2 0 U1g/C1 0 0 0 0 0;
%      0 0 1/C2_s/2 0 U2g/C2_s 0 0 0 0 0;
%      0 1/Cenv 0 (U_ro+U_inf)/Cenv 0 0 0 1/Cenv 0 1/Cenv;
%      0 0 0 0 U2g/C2 0 0 1/C2 0 0];
% %      0 0 0 (U_ao+U_infa)/Ca 0 0 0 0 0 0];
%
% C=[1 0 0 0 0 0;0 1 0 0 0 0;0 0 1 0 0 0;0 0 0 1 0 0;0 0 0 0 1 0;0 0 0 0 0 1 ];
% D=[0 0 0 0 0 0 0 0 0 0;0 0 0 0 0 0 0 0 0;0 0 0 0 0 0 0 0 0;0 0 0 0 0 0 0 0 0;0
0 0 0 0 0 0 0 0 0];

% %radiatiant floor
% %x=[Ts T1 Tr T2]
% %u=[Qhp Qint Qsol To Tg S Qhyd Qsol_r]
% A=[-(U_eff+U_airf+U_airw+U_infs)/Ceff (U_airf)/Ceff U_airw/Ceff 0;
%      U_airf/C1 -(U_airf+U1g)/C1 0 0;
%      U_airw/Cenv 0 -(U_airw+U_ro+U_r2+U_inf)/Cenv U_r2/Cenv;
%      0 0 U_r2/C2 -(U_r2+U2g)/C2];
%
% B=[-1/Ceff 0 0 (U_eff+U_infs)/Ceff 0 1/Ceff 0 0;
%      0 0 1/C1 0 U1g/C1 0 0 0;
%      0 1/Cenv 0 (U_ro+U_inf)/Cenv 0 0 0 0;
%      0 0 0 0 U2g/C2 0 1/C2 1/C2];
%
% C=[1 0 0 0;0 1 0 0;0 0 1 0;0 0 0 1];
% D=[0 0 0 0 0 0 0 0;0 0 0 0 0 0 0 0;0 0 0 0 0 0 0 0;0 0 0 0 0 0 0 0];

```

MATLAB Code: Thermal Storage Model



```

function [A,B,C,D,Q_BB_top,Q_BB_bot] =
input_functions(m_hp,m_coil,T_coil,T2,V,T1,T3,T4,T5,T6,T8,T7,cs,cs2,timestep)
Tmain=T_coil;
if timestep<=10
    T1=15;
    T2=15;
    T3=15;
    T4=15;
    T5=15;
    T6=15;
    T7=15;
    T8=15;
end

cp_w=4.19;
T1_K=T1+273.15;
T2_K=T2+273.15;
T3_K=T3+273.15;
T4_K=T4+273.15;
T5_K=T5+273.15;
T6_K=T6+273.15;
T7_K=T7+273.15;
T8_K=T8+273.15;

cp_w1=31.74724-0.3195258*T1_K+0.001388784*T1_K^2-0.000002687546*T1_K^3+(1.9579*10^-
09)*T1_K^4;
rho1=878.5596+1.140717*T1_K-0.00248152*T1_K^2;

```

```
cp_w2=31.74724-0.3195258*T2_K+0.001388784*T2_K^2-0.000002687546*T2_K^3+(1.9579*10^-09)*T2_K^4;  
rho2=878.5596+1.140717*T2_K-0.00248152*T2_K^2;
```

```
cp_w3=31.74724-0.3195258*T3_K+0.001388784*T3_K^2-0.000002687546*T3_K^3+(1.9579*10^-09)*T3_K^4;  
rho3=878.5596+1.140717*T3_K-0.00248152*T3_K^2;
```

```
cp_w4=31.74724-0.3195258*T4_K+0.001388784*T4_K^2-0.000002687546*T4_K^3+(1.9579*10^-09)*T4_K^4;  
rho4=878.5596+1.140717*T4_K-0.00248152*T4_K^2;
```

```
cp_w5=31.74724-0.3195258*T5_K+0.001388784*T5_K^2-0.000002687546*T5_K^3+(1.9579*10^-09)*T5_K^4;  
rho5=878.5596+1.140717*T5_K-0.00248152*T5_K^2;
```

```
cp_w6=31.74724-0.3195258*T6_K+0.001388784*T6_K^2-0.000002687546*T6_K^3+(1.9579*10^-09)*T6_K^4;  
rho6=878.5596+1.140717*T6_K-0.00248152*T6_K^2;
```

```
cp_w7=31.74724-0.3195258*T7_K+0.001388784*T7_K^2-0.000002687546*T7_K^3+(1.9579*10^-09)*T7_K^4;  
rho7=878.5596+1.140717*T7_K-0.00248152*T7_K^2;
```

```
cp_w8=31.74724-0.3195258*T8_K+0.001388784*T8_K^2-0.000002687546*T8_K^3+(1.9579*10^-09)*T8_K^4;  
rho8=878.5596+1.140717*T8_K-0.00248152*T8_K^2;
```

```
m_hp=m_hp/3.6/1000;  
m_coil=m_coil/3.6/1000;  
% m_main=m_main/1000; %m_coil/3.6/1000;
```

```
%%%%%%%%%%%%%%%%%%%%%%%%%%%%%%%%%%%%%%%%%%%%%%%%%%%%%%%%%%%%%%%%%%%%%%%%  
%Tank specs  
%%%%%%%%%%%%%%%%%%%%%%%%%%%%%%%%%%%%%%%%%%%%%%%%%%%%%%%%%%%%%%%%%%%%%%%%  
%V=0.2; %in m3  
% H_tot=2;  
d=0.7;  
H_tot=V/pi/((d/2)^2);  
num_nodes=8;  
H_node=H_tot/num_nodes;  
V_node=V/num_nodes*1.2;
```

```

U_loss_s=0; %0.000237;
A_loss_s=2*pi*d/2*H_node;
U_loss_tb=0; %0.000237; %kJ/K/s
A_loss_tb=pi*(d/2)^2+2*pi*d/2*H_node;
L_cond1=H_node;
L_cond2=L_cond1;
k_w=2.14/1000/3.6;
A_1=pi*(d/2)^2;
A_2=A_1;
Cw=V_node*rho1*cp_w1;
Cw2=V_node*rho2*cp_w2;
Cw3=V_node*rho3*cp_w3;
Cw4=V_node*rho4*cp_w4;
Cw5=V_node*rho5*cp_w5;
Cw6=V_node*rho6*cp_w6;
Cw7=V_node*rho7*cp_w7;
Cw8=V_node*rho8*cp_w8; %kJ/K
% m_main=0;
% m_hp=0;
m_invert=75/1000/3.6; %kg/s

%%%%%%%%%%
%HX coil specs
%%%%%%%%%%
d_o=0.032;
c_w=2.14; %conductivity
density=1000;
v=3.21;
b=0.00026;
d_coil=0.3;
d_i=0.03;
L=15;
pitch=0.02;
Ao=pi*d_o*L;
Ai=pi*d_i*L;
cp_w22=4.19;
Ch=pi*(d_i^2)*L/4*density*cp_w22;

u=v/density;
alpha=c_w/density/cp_w22;

Ra=(9.81*3600*3600*b*(abs(T_coil-T2))*d_o^3)/(u*alpha);
Nud=0.6*(Ra^0.25)*(1^1);
ho=Nud*c_w/d_o;

Rw=log(d_o/d_i)/(2*pi*L*c_w);
Re_critical=20000*(d_i/d_coil)^0.32;
Re=4*m_coil/(pi*d_i*v);

```

```

Pr=cp_w22*v/c_w*1000;
if Re==0
Re=0;
end

if Re_critical>Re %laminar
HE=Re*(d_i/d_coil)^0.5/(1+(pitch/pi/d_i)^2);
if m_coil<=0
Nu=0;
else
Nu=((48/11+(51/11)/(1+(1342/Pr/(HE^2))^2))^3+1.816*(HE/(1+1.15/Pr))^(1.5))^(1/3);
end
else
Nu=0.023*(Re^0.85)*(Pr^0.4)*(d_i/d_coil)^0.1;
end
hi=Nu*k_w/d_i;

n=10; %number of identical pipes in the HX coil

U_coil=0;%n/(1/ho/Ao+Rw+1/hi/Ai)/1000/4;
Q_BB_top=cs*4;
Q_BB_bot=cs2*4;

% A=[(U_loss*A_loss-k_w*A_1/L_cond1+m_main*cp_w+m_hp)/Cw (-k_w*A_1/L_cond1-m_hp*cp_w-
m_main*cp_w)/Cw 0;(-k_w*A_1/L_cond1+m_hp*cp_w-m_main*cp_w)/Cw2 (-k_w*A_1/L_cond1-
k_w*A_2/L_cond2+U_loss*A_loss)/Cw2 (-k_w*A_2/L_cond2-m_hp*cp_w-m_main*cp_w)/Cw2;0 (-
k_w*A_2/L_cond2+m_hp*cp_w-m_main*cp_w)/Cw3 ((-k_w*A_2/L_cond2+U_loss*A_loss-
m_hp*cp_w))/Cw3];
% A=[(-U_loss*A_loss-k_w*A_1/L_cond1-m_main*cp_w-m_hp*cp_w)/Cw
(k_w*A_1/L_cond1+m_hp*cp_w)/Cw 0;(k_w*A_1/L_cond1+m_hp*cp_w+m_main*cp_w)/Cw2 (-
k_w*A_1/L_cond1-k_w*A_2/L_cond2-U_loss*A_loss-m_hp*cp_w*2-m_main*cp_w*2)/Cw2
(k_w*A_2/L_cond2+m_hp*cp_w+m_main*cp_w)/Cw2;0
(k_w*A_2/L_cond2+m_hp*cp_w+m_main*cp_w)/Cw3 ((-k_w*A_2/L_cond2-U_loss*A_loss-
m_hp*cp_w*2-m_main*cp_w))/Cw3];
% B=[0 U_loss*A_loss/Cw m_main*cp_w/Cw 0;0 U_loss*A_loss/Cw2 0 0;m_hp*cp_w/Cw3
U_loss*A_loss/Cw3 0 0];
% C=[1 0 0;0 1 0;0 0 1];
% D=[0 0 0 0;0 0 0 0;0 0 0 0];

% %HX coil
%x=[T1 T2 T3 T4 T5 T6 T7 T8 Tout_HP Tout_ Tcoil_out]
% A=[(-U_loss_tb*A_loss_tb-k_w*A_1/L_cond1-m_hp*cp_w-m_main*cp_w*2)/Cw
(k_w*A_1/L_cond1+m_hp*cp_w+m_main*cp_w)/Cw 0 0 0 0 0 0 0;
% (k_w*A_1/L_cond1+m_hp*cp_w+m_main*cp_w)/Cw2 (-k_w*A_1/L_cond1-k_w*A_2/L_cond2-
U_loss_s*A_loss_s-m_hp*cp_w*2-m_main*cp_w*2-U_coil)/Cw2
(k_w*A_2/L_cond2+m_hp*cp_w+m_main*cp_w)/Cw2 0 0 0 0 0 0;

```

```

% 0 (k_w*A_2/L_cond2+m_hp*cp_w+m_main*cp_w)/Cw3 (-k_w*A_1/L_cond1-k_w*A_2/L_cond2-
U_loss_s*A_loss_s-m_hp*cp_w*2-m_main*cp_w*2-U_coil)/Cw3
(k_w*A_2/L_cond2+m_hp*cp_w+m_main*cp_w)/Cw3 0 0 0 0 0;
% 0 0 (k_w*A_2/L_cond2+m_hp*cp_w+m_main*cp_w)/Cw4 (-k_w*A_1/L_cond1-k_w*A_2/L_cond2-
U_loss_s*A_loss_s-m_hp*cp_w*2-m_main*cp_w*2-U_coil)/Cw4
(k_w*A_2/L_cond2+m_hp*cp_w+m_main*cp_w)/Cw4 0 0 0 0;
% 0 0 0 (k_w*A_2/L_cond2+m_hp*cp_w+m_main*cp_w)/Cw5 (-k_w*A_1/L_cond1-k_w*A_2/L_cond2-
U_loss_s*A_loss_s-m_hp*cp_w*2-m_main*cp_w*2-U_coil)/Cw5
(k_w*A_2/L_cond2+m_hp*cp_w+m_main*cp_w)/Cw5 0 0 0;
% 0 0 0 0 (k_w*A_2/L_cond2+m_hp*cp_w+m_main*cp_w)/Cw6 (-k_w*A_1/L_cond1-
k_w*A_2/L_cond2-U_loss_s*A_loss_s-m_hp*cp_w*2-m_main*cp_w*2)/Cw6
(k_w*A_2/L_cond2+m_hp*cp_w+m_main*cp_w)/Cw6 0 0;
% 0 0 0 0 0 (k_w*A_2/L_cond2+m_hp*cp_w+m_main*cp_w)/Cw7 (-k_w*A_1/L_cond1-
k_w*A_2/L_cond2-U_loss_s*A_loss_s-m_hp*cp_w*2-m_main*cp_w*2)/Cw7
(k_w*A_2/L_cond2+m_hp*cp_w+m_main*cp_w)/Cw7 0;
% 0 0 0 0 0 0 (k_w*A_2/L_cond2+m_hp*cp_w+m_main*cp_w)/Cw8 -
(k_w*A_2/L_cond2+m_hp*cp_w*2+m_main*cp_w)/Cw8 0;
% 0 U_coil/Ch U_coil/Ch U_coil/Ch U_coil/Ch 0 0 0 (-m_coil*cp_w2/1000-U_coil)/Ch];
%
% B=[0 U_loss_tb*A_loss_tb/Cw m_main*cp_w/Cw 0;
% 0 U_loss_s*A_loss_s/Cw2 0 U_coil/Cw2;
% 0 U_loss_s*A_loss_s/Cw3 0 U_coil/Cw3;
% 0 U_loss_s*A_loss_s/Cw4 0 U_coil/Cw4;
% 0 U_loss_s*A_loss_s/Cw5 0 U_coil/Cw5;
% 0 U_loss_s*A_loss_s/Cw6 0 0;
% 0 U_loss_s*A_loss_s/Cw7 0 0;
% m_hp*cp_w/Cw8 U_loss_tb*A_loss_tb/Cw8 0 0;
% 0 0 0 m_coil*cp_w2/Ch/1000];
%
% C=[1 0 0 0 0 0 0 0;0 1 0 0 0 0 0 0;0 0 1 0 0 0 0 0;0 0 0 1 0 0 0 0;0 0 0 0
1 0 0 0 0;0 0 0 0 1 0 0 0;0 0 0 0 0 1 0 0;0 0 0 0 0 0 1 0;0 0 0 0 0 0 0 1];
% D=[0 0 0 0;0 0 0 0;0 0 0 0;0 0 0 0;0 0 0 0;0 0 0 0;0 0 0 0;0 0 0 0];

% if T8>T7 && T1<T2
% mix_on=1;
%
% A=[(-U_loss_tb*A_loss_tb-k_w*A_1/L_cond1-m_invert*cp_w1)/Cw
(k_w*A_1/L_cond1+m_invert*cp_w1)/Cw 0 0 0 0 0 0 0 0;
% (k_w*A_1/L_cond1+m_invert*cp_w2)/Cw2 (-k_w*A_1/L_cond1-k_w*A_2/L_cond2-
U_loss_s*A_loss_s-m_hp*cp_w2-m_main*cp_w2*2-U_coil-m_invert*cp_w2)/Cw2
(k_w*A_2/L_cond2+m_hp*cp_w2+m_main*cp_w2)/Cw2 0 0 0 0 U_coil*2/Cw2 0 0 0 0;
% 0 (k_w*A_2/L_cond2+m_hp*cp_w3+m_main*cp_w3)/Cw3 (-k_w*A_1/L_cond1-k_w*A_2/L_cond2-
U_loss_s*A_loss_s-m_hp*cp_w3*2-m_main*cp_w3*2-U_coil)/Cw3
(k_w*A_2/L_cond2+m_hp*cp_w3+m_main*cp_w3)/Cw3 0 0 0 0 U_coil/Cw3 0 0 0;
% 0 0 (k_w*A_2/L_cond2+m_hp*cp_w4+m_main*cp_w4)/Cw4 (-k_w*A_1/L_cond1-k_w*A_2/L_cond2-
U_loss_s*A_loss_s-m_hp*cp_w4*2-m_main*cp_w4*2-U_coil)/Cw4
(k_w*A_2/L_cond2+m_hp*cp_w4+m_main*cp_w4)/Cw4 0 0 0 0 U_coil/Cw4 0 0;
% 0 0 0 (k_w*A_2/L_cond2+m_hp*cp_w5+m_main*cp_w5)/Cw5 (-k_w*A_1/L_cond1-
k_w*A_2/L_cond2-U_loss_s*A_loss_s-m_hp*cp_w5*2-m_main*cp_w5*2-U_coil)/Cw5
(k_w*A_2/L_cond2+m_hp*cp_w5+m_main*cp_w5)/Cw5 0 0 0 0 U_coil/Cw5 0;

```



```

% 0 0 (k_w*A_2/L_cond2+m_hp*cp_w4+m_main*cp_w4)/Cw4 (-k_w*A_1/L_cond1-k_w*A_2/L_cond2-
U_loss_s*A_loss_s-m_hp*cp_w4*2-m_main*cp_w4*2-U_coil)/Cw4
(k_w*A_2/L_cond2+m_hp*cp_w4+m_main*cp_w4)/Cw4 0 0 0 0 U_coil/Cw4 0 0;
% 0 0 0 0 (k_w*A_2/L_cond2+m_hp*cp_w5+m_main*cp_w5)/Cw5 (-k_w*A_1/L_cond1-
k_w*A_2/L_cond2-U_loss_s*A_loss_s-m_hp*cp_w5*2-m_main*cp_w5*2-U_coil)/Cw5
(k_w*A_2/L_cond2+m_hp*cp_w5+m_main*cp_w5)/Cw5 0 0 0 0 U_coil/Cw5 0;
% 0 0 0 0 (k_w*A_2/L_cond2+m_hp*cp_w6+m_main*cp_w6)/Cw6 (-k_w*A_1/L_cond1-
k_w*A_2/L_cond2-U_loss_s*A_loss_s-m_hp*cp_w6*2-m_main*cp_w6*2-U_coil)/Cw6
(k_w*A_2/L_cond2+m_hp*cp_w6+m_main*cp_w6)/Cw6 0 0 0 0 U_coil/Cw6;
% 0 0 0 0 0 (k_w*A_2/L_cond2+m_hp*cp_w7+m_main*cp_w7)/Cw7 (-k_w*A_1/L_cond1-
k_w*A_2/L_cond2-U_loss_s*A_loss_s-m_hp*cp_w7*2-m_main*cp_w7)/Cw7
(k_w*A_2/L_cond2)/Cw7 0 0 0 0;
% 0 0 0 0 0 0 0 (k_w*A_2/L_cond2+m_invert*cp_w7)/Cw8 -
(k_w*A_2/L_cond2+U_loss_tb*A_loss_tb+m_invert*cp_w7)/Cw8 0 0 0 0;
% 0 U_coil/Ch 0 0 0 0 0 0 (-m_coil*cp_w22*2/1000-U_coil)/Ch (m_coil*cp_w22/1000)/Ch 0
0 0;
% 0 0 U_coil/Ch 0 0 0 0 0 (m_coil*cp_w22/1000)/Ch (-m_coil*cp_w22*2/1000-U_coil)/Ch
(m_coil*cp_w22/1000)/Ch 0 0;
% 0 0 0 U_coil/Ch 0 0 0 0 0 (m_coil*cp_w22/1000)/Ch (-m_coil*cp_w22*2/1000-U_coil)/Ch
(m_coil*cp_w22/1000)/Ch 0;
% 0 0 0 0 U_coil/Ch 0 0 0 0 0 (m_coil*cp_w22/1000)/Ch (-m_coil*cp_w22*2/1000-U_coil)/Ch
(m_coil*cp_w22/1000)/Ch;
% 0 0 0 0 0 U_coil/Ch 0 0 0 0 0 (m_coil*cp_w22/1000)/Ch (-m_coil*cp_w22/1000-
U_coil)/Ch];
%
% B=[0 U_loss_tb*A_loss_tb/Cw 0 0 0 1/Cw;
% 0 U_loss_s*A_loss_s/Cw2 m_main*cp_w2*1/Cw2 U_coil/Cw2 0 0;
% 0 U_loss_s*A_loss_s/Cw3 0 0 0 0;
% 0 U_loss_s*A_loss_s/Cw4 0 0 0 0;
% 0 U_loss_s*A_loss_s/Cw5 0 0 0 0;
% 0 U_loss_s*A_loss_s/Cw6 0 0 0 0;
% m_hp*cp_w7/Cw7 U_loss_s*A_loss_s/Cw7 0 0 1/Cw7 0;
% 0 U_loss_tb*A_loss_tb/Cw8 0 0 0 0;
% 0 0 0 m_coil*cp_w22/Ch/1000 0 0;
% 0 0 0 0 0 0;
% 0 0 0 0 0 0;
% 0 0 0 0 0 0;
% 0 0 0 0 0 0];
%
% C=[1 0 0 0 0 0 0 0 0 0 0 0;0 1 0 0 0 0 0 0 0 0 0 0;0 0 1 0 0 0 0 0 0 0 0 0;0
0 0 1 0 0 0 0 0 0 0 0 0;0 0 0 0 1 0 0 0 0 0 0 0;0 0 0 0 0 1 0 0 0 0 0 0;0 0 0 0 0
0 1 0 0 0 0 0 0;0 0 0 0 0 0 0 1 0 0 0 0;0 0 0 0 0 0 0 0 1 0 0 0;0 0 0 0 0 0 0 0 0
1 0 0 0;0 0 0 0 0 0 0 0 0 1 0 0;0 0 0 0 0 0 0 0 0 0 0 1 0;0 0 0 0 0 0 0 0 0 0 0 0
0 1];
% D=[0 0 0 0 0 0;0 0 0 0 0 0;0 0 0 0 0 0;0 0 0 0 0 0;0 0 0 0 0 0;0 0 0 0 0 0;0 0 0
0 0 0;0 0 0 0 0 0;0 0 0 0 0 0;0 0 0 0 0 0;0 0 0 0 0 0];
% else if T8>T7
% mix_on=1;
%
% A=[(-U_loss_tb*A_loss_tb-k_w*A_1/L_cond1-m_invert*cp_w1)/Cw
(k_w*A_1/L_cond1+m_invert*cp_w1)/Cw 0 0 0 0 0 0 0 0 0 0;

```

```

%      (k_w*A_1/L_cond1+m_invert*cp_w2)/Cw2      (-k_w*A_1/L_cond1-k_w*A_2/L_cond2-
U_loss_s*A_loss_s-m_hp*cp_w2-m_main*cp_w2*2-U_coil-m_invert*cp_w2)/Cw2
(k_w*A_2/L_cond2+m_hp*cp_w2+m_main*cp_w2)/Cw2 0 0 0 0 U_coil*2/Cw2 0 0 0 0;
% 0 (k_w*A_2/L_cond2+m_hp*cp_w3+m_main*cp_w3)/Cw3 (-k_w*A_1/L_cond1-k_w*A_2/L_cond2-
U_loss_s*A_loss_s-m_hp*cp_w3*2-m_main*cp_w3*2-U_coil)/Cw3
(k_w*A_2/L_cond2+m_hp*cp_w3+m_main*cp_w3)/Cw3 0 0 0 0 U_coil/Cw3 0 0 0 0;
% 0 0 (k_w*A_2/L_cond2+m_hp*cp_w4+m_main*cp_w4)/Cw4 (-k_w*A_1/L_cond1-k_w*A_2/L_cond2-
U_loss_s*A_loss_s-m_hp*cp_w4*2-m_main*cp_w4*2-U_coil)/Cw4
(k_w*A_2/L_cond2+m_hp*cp_w4+m_main*cp_w4)/Cw4 0 0 0 0 U_coil/Cw4 0 0;
% 0 0 0 (k_w*A_2/L_cond2+m_hp*cp_w5+m_main*cp_w5)/Cw5 (-k_w*A_1/L_cond1-
k_w*A_2/L_cond2-U_loss_s*A_loss_s-m_hp*cp_w5*2-m_main*cp_w5*2-U_coil)/Cw5
(k_w*A_2/L_cond2+m_hp*cp_w5+m_main*cp_w5)/Cw5 0 0 0 0 U_coil/Cw5 0;
% 0 0 0 0 (k_w*A_2/L_cond2+m_hp*cp_w6+m_main*cp_w6)/Cw6 (-k_w*A_1/L_cond1-
k_w*A_2/L_cond2-U_loss_s*A_loss_s-m_hp*cp_w6*2-m_main*cp_w6*2-U_coil)/Cw6
(k_w*A_2/L_cond2+m_hp*cp_w6+m_main*cp_w6)/Cw6 0 0 0 0 U_coil/Cw6;
% 0 0 0 0 0 (k_w*A_2/L_cond2+m_hp*cp_w7+m_main*cp_w7)/Cw7 (-k_w*A_1/L_cond1-
k_w*A_2/L_cond2-U_loss_s*A_loss_s-m_hp*cp_w7*2-m_main*cp_w7)/Cw7
(k_w*A_2/L_cond2)/Cw7 0 0 0 0 0;
% 0 0 0 0 0 0 (k_w*A_2/L_cond2)/Cw8 -(k_w*A_2/L_cond2+U_loss_tb*A_loss_tb)/Cw8 0 0 0
0 0;
% 0 U_coil/Ch 0 0 0 0 0 0 (-m_coil*cp_w22*2/1000-U_coil)/Ch (m_coil*cp_w22/1000)/Ch 0
0 0;
% 0 0 U_coil/Ch 0 0 0 0 0 0 (m_coil*cp_w22/1000)/Ch (-m_coil*cp_w22*2/1000-U_coil)/Ch
(m_coil*cp_w22/1000)/Ch 0 0;
% 0 0 0 U_coil/Ch 0 0 0 0 0 0 (m_coil*cp_w22/1000)/Ch (-m_coil*cp_w22*2/1000-U_coil)/Ch
(m_coil*cp_w22/1000)/Ch 0;
% 0 0 0 0 U_coil/Ch 0 0 0 0 0 0 (m_coil*cp_w22/1000)/Ch (-m_coil*cp_w22*2/1000-U_coil)/Ch
(m_coil*cp_w22/1000)/Ch;
% 0 0 0 0 0 U_coil/Ch 0 0 0 0 0 0 (m_coil*cp_w22/1000)/Ch (-m_coil*cp_w22/1000-
U_coil)/Ch];
%
% B=[0 U_loss_tb*A_loss_tb/Cw 0 0 0 1/Cw;
% 0 U_loss_s*A_loss_s/Cw2 m_main*cp_w2*1/Cw2 U_coil/Cw2 0 0;
% 0 U_loss_s*A_loss_s/Cw3 0 0 0 0;
% 0 U_loss_s*A_loss_s/Cw4 0 0 0 0;
% 0 U_loss_s*A_loss_s/Cw5 0 0 0 0;
% 0 U_loss_s*A_loss_s/Cw6 0 0 0 0;
% m_hp*cp_w7/Cw7 U_loss_s*A_loss_s/Cw7 0 0 1/Cw7 0;
% 0 U_loss_tb*A_loss_tb/Cw8 0 0 0 0;
% 0 0 0 m_coil*cp_w22/Ch/1000 0 0;
% 0 0 0 0 0 0;
% 0 0 0 0 0 0;
% 0 0 0 0 0 0;
% 0 0 0 0 0 0];
%
% C=[1 0 0 0 0 0 0 0 0 0 0 0 0 0 0 0;0 1 0 0 0 0 0 0 0 0 0 0 0 0 0 0;0 0 1 0 0 0 0 0 0 0 0 0 0 0 0;0
0 0 1 0 0 0 0 0 0 0 0 0 0 0 0;0 0 0 0 1 0 0 0 0 0 0 0 0 0 0;0 0 0 0 0 1 0 0 0 0 0 0 0 0 0;0 0 0 0 0 0 1 0 0 0 0 0 0 0 0
0 1 0 0 0 0 0 0;0 0 0 0 0 0 0 1 0 0 0 0 0 0;0 0 0 0 0 0 0 0 1 0 0 0 0 0 0;0 0 0 0 0 0 0 0 0 1 0 0 0 0 0 0 0 0 0 0 0 0 0 0 0
1];
% D=[0 0 0 0 0 0;0 0 0 0 0 0;0 0 0 0 0 0;0 0 0 0 0 0;0 0 0 0 0 0;0 0 0 0 0 0;0 0 0 0
0 0;0 0 0 0 0 0;0 0 0 0 0 0;0 0 0 0 0 0;0 0 0 0 0 0];

```

```

% else
% mix_on=0;
% A=[(-U_loss_tb*A_loss_tb-k_w*A_1/L_cond1)/Cw (k_w*A_1/L_cond1)/Cw 0 0 0 0 0 0 0 0
0 0;
% (k_w*A_1/L_cond1)/Cw2 (-k_w*A_1/L_cond1-k_w*A_2/L_cond2-U_loss_s*A_loss_s-
m_hp*cp_w2-m_main*cp_w2*2-U_coil)/Cw2 (k_w*A_2/L_cond2+m_hp*cp_w2+m_main*cp_w2)/Cw2 0
0 0 0 U_coil/Cw2 0 0 0 0;
% 0 (k_w*A_2/L_cond2+m_hp*cp_w3+m_main*cp_w3)/Cw3 (-k_w*A_1/L_cond1-k_w*A_2/L_cond2-
U_loss_s*A_loss_s-m_hp*cp_w3*2-m_main*cp_w3*2-U_coil)/Cw3
(k_w*A_2/L_cond2+m_hp*cp_w3+m_main*cp_w3)/Cw3 0 0 0 0 U_coil*2/Cw3 0 0 0;
% 0 0 (k_w*A_2/L_cond2+m_hp*cp_w4+m_main*cp_w4)/Cw4 (-k_w*A_1/L_cond1-k_w*A_2/L_cond2-
U_loss_s*A_loss_s-m_hp*cp_w4*2-m_main*cp_w4*2-U_coil)/Cw4
(k_w*A_2/L_cond2+m_hp*cp_w4+m_main*cp_w4)/Cw4 0 0 0 0 U_coil/Cw4 0 0;
% 0 0 0 (k_w*A_2/L_cond2+m_hp*cp_w5+m_main*cp_w5)/Cw5 (-k_w*A_1/L_cond1-
k_w*A_2/L_cond2-U_loss_s*A_loss_s-m_hp*cp_w5*2-m_main*cp_w5*2-U_coil)/Cw5
(k_w*A_2/L_cond2+m_hp*cp_w5+m_main*cp_w5)/Cw5 0 0 0 0 U_coil/Cw5 0;
% 0 0 0 0 (k_w*A_2/L_cond2+m_hp*cp_w6+m_main*cp_w6)/Cw6 (-k_w*A_1/L_cond1-
k_w*A_2/L_cond2-U_loss_s*A_loss_s-m_hp*cp_w6*2-m_main*cp_w6*2-U_coil)/Cw6
(k_w*A_2/L_cond2+m_hp*cp_w6+m_main*cp_w6)/Cw6 0 0 0 0 U_coil/Cw6;
% 0 0 0 0 0 (k_w*A_2/L_cond2+m_hp*cp_w7+m_main*cp_w7)/Cw7 (-k_w*A_1/L_cond1-
k_w*A_2/L_cond2-U_loss_s*A_loss_s-m_hp*cp_w7*2-m_main*cp_w7)/Cw7
(k_w*A_2/L_cond2)/Cw7 0 0 0 0 0;
% 0 0 0 0 0 0 (k_w*A_2/L_cond2)/Cw8 -(k_w*A_2/L_cond2+U_loss_tb*A_loss_tb)/Cw8 0 0 0
0 0;
% 0 U_coil/Ch 0 0 0 0 0 0 (-m_coil*cp_w22*2/1000-U_coil)/Ch (m_coil*cp_w22/1000)/Ch 0
0 0;
% 0 0 U_coil/Ch 0 0 0 0 0 (m_coil*cp_w22/1000)/Ch (-m_coil*cp_w22*2/1000-U_coil)/Ch
(m_coil*cp_w22/1000)/Ch 0 0;
% 0 0 0 U_coil/Ch 0 0 0 0 0 (m_coil*cp_w22/1000)/Ch (-m_coil*cp_w22*2/1000-U_coil)/Ch
(m_coil*cp_w22/1000)/Ch 0;
% 0 0 0 0 U_coil/Ch 0 0 0 0 0 (m_coil*cp_w22/1000)/Ch (-m_coil*cp_w22*2/1000-U_coil)/Ch
(m_coil*cp_w22/1000)/Ch;
% 0 0 0 0 0 U_coil/Ch 0 0 0 0 0 (m_coil*cp_w22/1000)/Ch (-m_coil*cp_w22/1000-
U_coil)/Ch];
%
% B=[0 U_loss_tb*A_loss_tb/Cw 0 0 0 1/Cw;
% 0 U_loss_s*A_loss_s/Cw2 m_main*cp_w2*1/Cw2 U_coil/Cw2 0 0;
% 0 U_loss_s*A_loss_s/Cw3 0 0 0 0;
% 0 U_loss_s*A_loss_s/Cw4 0 0 0 0;
% 0 U_loss_s*A_loss_s/Cw5 0 0 0 0;
% 0 U_loss_s*A_loss_s/Cw6 0 0 0 0;
% m_hp*cp_w7/Cw7 U_loss_s*A_loss_s/Cw7 0 0 1/Cw7 0;
% 0 U_loss_tb*A_loss_tb/Cw8 0 0 0 0;
% 0 0 0 m_coil*cp_w22/Ch/1000 0 0;
% 0 0 0 0 0 0;
% 0 0 0 0 0 0;
% 0 0 0 0 0 0;
% 0 0 0 0 0 0];
%
% C=[1 0 0 0 0 0 0 0 0 0 0 0;0 1 0 0 0 0 0 0 0 0 0 0;0 0 1 0 0 0 0 0 0 0 0 0;0
0 0 1 0 0 0 0 0 0 0 0 0;0 0 0 0 1 0 0 0 0 0 0 0;0 0 0 0 0 1 0 0 0 0 0 0;0 0 0 0 0
0 1 0 0 0 0 0 0;0 0 0 0 0 0 0 1 0 0 0 0;0 0 0 0 0 0 0 0 1 0 0 0;0 0 0 0 0 0 0 0 0
0 1 0 0 0 0 0 0 0 0 0 0];

```

```

1 0 0 0;0 0 0 0 0 0 0 0 0 0 1 0 0;0 0 0 0 0 0 0 0 0 0 0 1 0;0 0 0 0 0 0 0 0 0 0 0 0 0
1];
% D=[0 0 0 0 0 0;0 0 0 0 0 0;0 0 0 0 0 0;0 0 0 0 0 0;0 0 0 0 0 0;0 0 0 0 0 0;0 0 0 0
0 0;0 0 0 0 0 0;0 0 0 0 0 0;0 0 0 0 0 0;0 0 0 0 0 0;0 0 0 0 0 0];
% end
%
%
% end
%
%
if T8>T7 && T1<T2
mix_on=1;
A=[(-U_loss_tb*A_loss_tb-k_w*A_1/L_cond1-m_invert*cp_w1)/Cw
(k_w*A_1/L_cond1+m_invert*cp_w1)/Cw 0 0 0 0 0;
(k_w*A_1/L_cond1+m_invert*cp_w2)/Cw2 (-k_w*A_1/L_cond1-k_w*A_2/L_cond2-
U_loss_s*A_loss_s-m_hp*cp_w2-m_coil*cp_w2*2-U_coil-m_invert*cp_w2)/Cw2
(k_w*A_2/L_cond2+m_hp*cp_w2+m_coil*cp_w2)/Cw2 0 0 0 0;
0 (k_w*A_2/L_cond2+m_hp*cp_w3+m_coil*cp_w3)/Cw3 (-k_w*A_1/L_cond1-k_w*A_2/L_cond2-
U_loss_s*A_loss_s-m_hp*cp_w3*2-m_coil*cp_w3*2-U_coil)/Cw3
(k_w*A_2/L_cond2+m_hp*cp_w3+m_coil*cp_w3)/Cw3 0 0 0 0;
0 0 (k_w*A_2/L_cond2+m_hp*cp_w4+m_coil*cp_w4)/Cw4 (-k_w*A_1/L_cond1-k_w*A_2/L_cond2-
U_loss_s*A_loss_s-m_hp*cp_w4*2-m_coil*cp_w4*2-U_coil)/Cw4
(k_w*A_2/L_cond2+m_hp*cp_w4+m_coil*cp_w4)/Cw4 0 0 0;
0 0 0 (k_w*A_2/L_cond2+m_hp*cp_w5+m_coil*cp_w5)/Cw5 (-k_w*A_1/L_cond1-k_w*A_2/L_cond2-
U_loss_s*A_loss_s-m_hp*cp_w5*2-m_coil*cp_w5*2-U_coil)/Cw5
(k_w*A_2/L_cond2+m_hp*cp_w5+m_coil*cp_w5)/Cw5 0 0 0;
0 0 0 0 (k_w*A_2/L_cond2+m_hp*cp_w6+m_coil*cp_w6)/Cw6 (-k_w*A_1/L_cond1-
k_w*A_2/L_cond2-U_loss_s*A_loss_s-m_hp*cp_w6*2-m_coil*cp_w6*2-U_coil)/Cw6
(k_w*A_2/L_cond2+m_coil*cp_w6)/Cw6 0;
0 0 0 0 0 (k_w*A_2/L_cond2+m_coil*cp_w7)/Cw7 (-k_w*A_1/L_cond1-k_w*A_2/L_cond2-
U_loss_s*A_loss_s-m_coil*cp_w7)/Cw7 (k_w*A_2/L_cond2)/Cw7;
0 0 0 0 0 0 0 (k_w*A_2/L_cond2+m_invert*cp_w7)/Cw8 -
(k_w*A_2/L_cond2+U_loss_tb*A_loss_tb+m_invert*cp_w7)/Cw8
];

B=[0 U_loss_tb*A_loss_tb/Cw 0 0 1/Cw;
0 U_loss_s*A_loss_s/Cw2 m_coil*cp_w2*1/Cw2 0 0;
0 U_loss_s*A_loss_s/Cw3 0 0 0;
0 U_loss_s*A_loss_s/Cw4 0 0 0;
0 U_loss_s*A_loss_s/Cw5 0 0 0;
m_hp*cp_w7/Cw7 U_loss_s*A_loss_s/Cw6 0 0 0;
0 U_loss_s*A_loss_s/Cw7 0 1/Cw7 0;
0 U_loss_tb*A_loss_tb/Cw8 0 0 0];

C=[1 0 0 0 0 0 0;0 1 0 0 0 0 0;0 0 1 0 0 0 0;0 0 0 1 0 0 0;0 0 0 0 1 0 0;0
0 0 0 0 1 0 0;0 0 0 0 0 1 0;0 0 0 0 0 0 1];
D=[0 0 0 0 0;0 0 0 0 0;0 0 0 0 0;0 0 0 0 0;0 0 0 0 0;0 0 0 0 0;0 0 0 0 0;0 0 0 0 0];
elseif T1<T2
mix_on=1;
A=[(-U_loss_tb*A_loss_tb-k_w*A_1/L_cond1)/Cw (k_w*A_1/L_cond1)/Cw 0 0 0 0 0 0;

```

```

(k_w*A_1/L_cond1+m_invert*cp_w2)/Cw2          (-k_w*A_1/L_cond1-k_w*A_2/L_cond2-
U_loss_s*A_loss_s-m_hp*cp_w2-m_coil*cp_w2*2-U_coil-m_invert*cp_w2)/Cw2
(k_w*A_2/L_cond2+m_hp*cp_w2+m_coil*cp_w2)/Cw2 0 0 0 0 0;
0 (k_w*A_2/L_cond2+m_hp*cp_w3+m_coil*cp_w3)/Cw3 (-k_w*A_1/L_cond1-k_w*A_2/L_cond2-
U_loss_s*A_loss_s-m_hp*cp_w3*2-m_coil*cp_w3*2-U_coil)/Cw3
(k_w*A_2/L_cond2+m_hp*cp_w3+m_coil*cp_w3)/Cw3 0 0 0 0;
0 0 (k_w*A_2/L_cond2+m_hp*cp_w4+m_coil*cp_w4)/Cw4 (-k_w*A_1/L_cond1-k_w*A_2/L_cond2-
U_loss_s*A_loss_s-m_hp*cp_w4*2-m_coil*cp_w4*2-U_coil)/Cw4
(k_w*A_2/L_cond2+m_hp*cp_w4+m_coil*cp_w4)/Cw4 0 0 0;
0 0 0 (k_w*A_2/L_cond2+m_hp*cp_w5+m_coil*cp_w5)/Cw5 (-k_w*A_1/L_cond1-k_w*A_2/L_cond2-
U_loss_s*A_loss_s-m_hp*cp_w5*2-m_coil*cp_w5*2-U_coil)/Cw5
(k_w*A_2/L_cond2+m_hp*cp_w5+m_coil*cp_w5)/Cw5 0 0;
0 0 0 0 (k_w*A_2/L_cond2+m_hp*cp_w6+m_coil*cp_w6)/Cw6 (-k_w*A_1/L_cond1-
k_w*A_2/L_cond2-U_loss_s*A_loss_s-m_hp*cp_w6*2-m_coil*cp_w6*2-U_coil)/Cw6
(k_w*A_2/L_cond2+m_coil*cp_w6)/Cw6 0;
0 0 0 0 0 (k_w*A_2/L_cond2+m_coil*cp_w7)/Cw7 (-k_w*A_1/L_cond1-k_w*A_2/L_cond2-
U_loss_s*A_loss_s-m_coil*cp_w7)/Cw7 (k_w*A_2/L_cond2)/Cw7;
0 0 0 0 0 0 0 (k_w*A_2/L_cond2+m_invert*cp_w7)/Cw8 -
(k_w*A_2/L_cond2+U_loss_tb*A_loss_tb+m_invert*cp_w7)/Cw8];

```

```

B=[0 U_loss_tb*A_loss_tb/Cw 0 0 1/Cw;
0 U_loss_s*A_loss_s/Cw2 m_coil*cp_w2*1/Cw2 0 0;
0 U_loss_s*A_loss_s/Cw3 0 0 0;
0 U_loss_s*A_loss_s/Cw4 0 0 0;
0 U_loss_s*A_loss_s/Cw5 0 0 0;
m_hp*cp_w7/Cw7 U_loss_s*A_loss_s/Cw6 0 0 0;
0 U_loss_s*A_loss_s/Cw7 0 1/Cw7 0;
0 U_loss_tb*A_loss_tb/Cw8 0 0 0];

```

```

C=[1 0 0 0 0 0 0 0;0 1 0 0 0 0 0 0;0 0 1 0 0 0 0 0;0 0 0 1 0 0 0 0;0 0 0 0 1 0 0 0;
0 0 0 0 1 0 0 0;0 0 0 0 0 1 0 0;0 0 0 0 0 0 1 0];

```

```

D=[0 0 0 0 0;0 0 0 0 0;0 0 0 0 0;0 0 0 0 0;0 0 0 0 0;0 0 0 0 0;0 0 0 0 0;0 0 0 0 0];

```

```

elseif T8>T7

```

```

mix_on=1;

```

```

A=[(-U_loss_tb*A_loss_tb-k_w*A_1/L_cond1-m_invert*cp_w1)/Cw
(k_w*A_1/L_cond1+m_invert*cp_w1)/Cw 0 0 0 0 0 0;
(k_w*A_1/L_cond1+m_invert*cp_w2)/Cw2          (-k_w*A_1/L_cond1-k_w*A_2/L_cond2-
U_loss_s*A_loss_s-m_hp*cp_w2-m_coil*cp_w2*2-U_coil-m_invert*cp_w2)/Cw2
(k_w*A_2/L_cond2+m_hp*cp_w2+m_coil*cp_w2)/Cw2 0 0 0 0 0;
0 (k_w*A_2/L_cond2+m_hp*cp_w3+m_coil*cp_w3)/Cw3 (-k_w*A_1/L_cond1-k_w*A_2/L_cond2-
U_loss_s*A_loss_s-m_hp*cp_w3*2-m_coil*cp_w3*2-U_coil)/Cw3
(k_w*A_2/L_cond2+m_hp*cp_w3+m_coil*cp_w3)/Cw3 0 0 0 0;
0 0 (k_w*A_2/L_cond2+m_hp*cp_w4+m_coil*cp_w4)/Cw4 (-k_w*A_1/L_cond1-k_w*A_2/L_cond2-
U_loss_s*A_loss_s-m_hp*cp_w4*2-m_coil*cp_w4*2-U_coil)/Cw4
(k_w*A_2/L_cond2+m_hp*cp_w4+m_coil*cp_w4)/Cw4 0 0 0;
0 0 0 (k_w*A_2/L_cond2+m_hp*cp_w5+m_coil*cp_w5)/Cw5 (-k_w*A_1/L_cond1-k_w*A_2/L_cond2-
U_loss_s*A_loss_s-m_hp*cp_w5*2-m_coil*cp_w5*2-U_coil)/Cw5
(k_w*A_2/L_cond2+m_hp*cp_w5+m_coil*cp_w5)/Cw5 0 0;

```

```

0 0 0 0 (k_w*A_2/L_cond2+m_hp*cp_w6+m_coil*cp_w6)/Cw6 (-k_w*A_1/L_cond1-
k_w*A_2/L_cond2-U_loss_s*A_loss_s-m_hp*cp_w6*2-m_coil*cp_w6*2-U_coil)/Cw6
(k_w*A_2/L_cond2+m_coil*cp_w6)/Cw6 0;
0 0 0 0 (k_w*A_2/L_cond2+m_coil*cp_w7)/Cw7 (-k_w*A_1/L_cond1-k_w*A_2/L_cond2-
U_loss_s*A_loss_s-m_coil*cp_w7)/Cw7 (k_w*A_2/L_cond2)/Cw7;
0 0 0 0 (k_w*A_2/L_cond2)/Cw8 -(k_w*A_2/L_cond2+U_loss_tb*A_loss_tb)/Cw8];

```

```

B=[0 U_loss_tb*A_loss_tb/Cw 0 0 1/Cw;
0 U_loss_s*A_loss_s/Cw2 m_coil*cp_w2*1/Cw2 0 0;
0 U_loss_s*A_loss_s/Cw3 0 0 0;
0 U_loss_s*A_loss_s/Cw4 0 0 0;
0 U_loss_s*A_loss_s/Cw5 0 0 0;
m_hp*cp_w7/Cw7 U_loss_s*A_loss_s/Cw6 0 0 0;
0 U_loss_s*A_loss_s/Cw7 0 1/Cw7 0;
0 U_loss_tb*A_loss_tb/Cw8 0 0 0];

```

```

C=[1 0 0 0 0 0 0;0 1 0 0 0 0 0;0 0 1 0 0 0 0;0 0 0 1 0 0 0;0 0 0 0 1 0 0;0
0 0 0 1 0 0;0 0 0 0 0 1 0;0 0 0 0 0 0 1];

```

```

D=[0 0 0 0 0;0 0 0 0 0;0 0 0 0 0;0 0 0 0 0;0 0 0 0 0;0 0 0 0 0;0 0 0 0 0];

```

```

else

```

```

mix_on=0;

```

```

A=[(-U_loss_tb*A_loss_tb-k_w*A_1/L_cond1)/Cw (k_w*A_1/L_cond1)/Cw 0 0 0 0 0;
(k_w*A_1/L_cond1)/Cw2 (-k_w*A_1/L_cond1-k_w*A_2/L_cond2-U_loss_s*A_loss_s-m_hp*cp_w2-
m_coil*cp_w2*2-U_coil)/Cw2 (k_w*A_2/L_cond2+m_hp*cp_w2+m_coil*cp_w2)/Cw2 0 0 0 0 0;
0 (k_w*A_2/L_cond2+m_hp*cp_w3+m_coil*cp_w3)/Cw3 (-k_w*A_1/L_cond1-k_w*A_2/L_cond2-
U_loss_s*A_loss_s-m_hp*cp_w3*2-m_coil*cp_w3*2-U_coil)/Cw3
(k_w*A_2/L_cond2+m_hp*cp_w3+m_coil*cp_w3)/Cw3 0 0 0 0;
0 0 (k_w*A_2/L_cond2+m_hp*cp_w4+m_coil*cp_w4)/Cw4 (-k_w*A_1/L_cond1-k_w*A_2/L_cond2-
U_loss_s*A_loss_s-m_hp*cp_w4*2-m_coil*cp_w4*2-U_coil)/Cw4
(k_w*A_2/L_cond2+m_hp*cp_w4+m_coil*cp_w4)/Cw4 0 0 0;
0 0 0 (k_w*A_2/L_cond2+m_hp*cp_w5+m_coil*cp_w5)/Cw5 (-k_w*A_1/L_cond1-k_w*A_2/L_cond2-
U_loss_s*A_loss_s-m_hp*cp_w5*2-m_coil*cp_w5*2-U_coil)/Cw5
(k_w*A_2/L_cond2+m_hp*cp_w5+m_coil*cp_w5)/Cw5 0 0;
0 0 0 0 (k_w*A_2/L_cond2+m_hp*cp_w6+m_coil*cp_w6)/Cw6 (-k_w*A_1/L_cond1-
k_w*A_2/L_cond2-U_loss_s*A_loss_s-m_hp*cp_w6*2-m_coil*cp_w6*2-U_coil)/Cw6
(k_w*A_2/L_cond2+m_coil*cp_w6)/Cw6 0;
0 0 0 0 (k_w*A_2/L_cond2+m_coil*cp_w7)/Cw7 (-k_w*A_1/L_cond1-k_w*A_2/L_cond2-
U_loss_s*A_loss_s-m_coil*cp_w7)/Cw7 (k_w*A_2/L_cond2)/Cw7;
0 0 0 0 0 (k_w*A_2/L_cond2)/Cw8 -(k_w*A_2/L_cond2+U_loss_tb*A_loss_tb)/Cw8];

```

```

B=[0 U_loss_tb*A_loss_tb/Cw 0 0 1/Cw;
0 U_loss_s*A_loss_s/Cw2 m_coil*cp_w2*1/Cw2 0 0;
0 U_loss_s*A_loss_s/Cw3 0 0 0;
0 U_loss_s*A_loss_s/Cw4 0 0 0;
0 U_loss_s*A_loss_s/Cw5 0 0 0;
m_hp*cp_w7/Cw7 U_loss_s*A_loss_s/Cw6 0 0 0;
0 U_loss_s*A_loss_s/Cw7 0 1/Cw7 0;
0 U_loss_tb*A_loss_tb/Cw8 0 0 0];

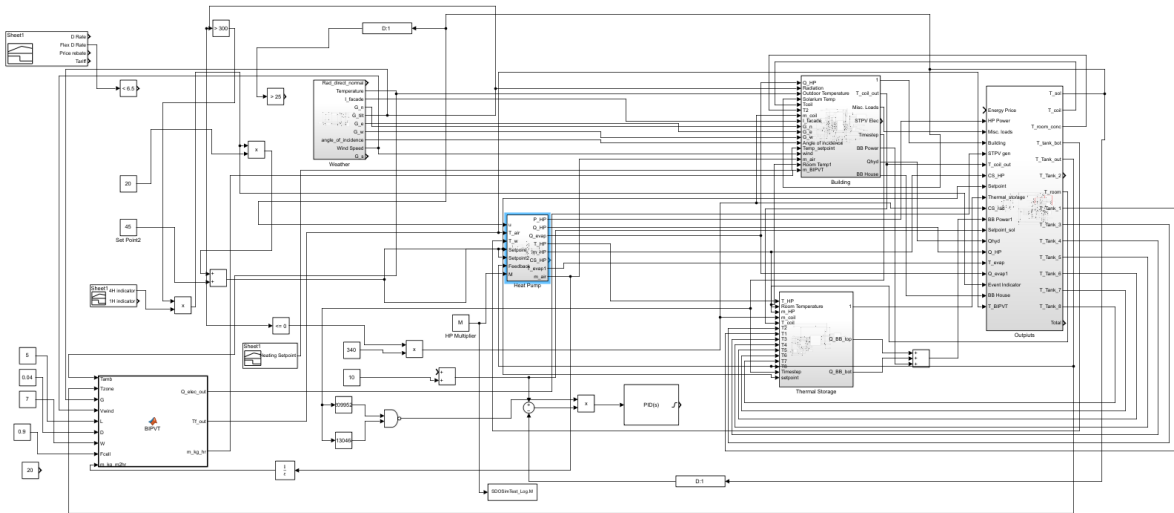
```

```

C=[1 0 0 0 0 0 0 0;0 1 0 0 0 0 0 0;0 0 1 0 0 0 0 0;0 0 0 1 0 0 0 0;0 0 0 0 1 0 0 0;0
0 0 0 0 1 0 0 0;0 0 0 0 0 1 0 0;0 0 0 0 0 0 1 0];
D=[0 0 0 0 0 0;0 0 0 0 0 0;0 0 0 0 0 0;0 0 0 0 0 0;0 0 0 0 0 0;0 0 0 0 0 0;0 0 0 0 0 0;0 0 0 0 0 0];
end
end

```

MATLAB Code: BIPVT Model



```

function [Q_elec_out,Tf_out,m_kg_hr] =
BIPVT(Tamb,Tzone,G,Vwind,L,D,W,Fcell,m_kg_m2hr)
    if isnan(G) || G>1500
        G=0;
    end
    G=G*3.6;
    %----Outdoor Conditions-----
    P=101.23;
    Rair=0.287;
    Tamb_K = Tamb+273.15;
    Tsky = (0.68+0.0552*Tamb_K^1.5)+0.32*Tamb_K-273.15;

    Tgn = Tamb_K;

    Fgn=0.5; %Fgn=(1-cos(Slope))/2
    Fsky=0.5; %Fsky=(1+cos(Slope))/2
    Tsur=(Fgn*Tgn^4+Fsky*(Tsky+273.15)^4)^(1/4)-273.15;

    coeff_effPV=-0.0027;
    a=28.11;
    b=0.001967;
    c=0.000004802;
    d=-1.966*10^(-9);
    mair=28.97;
    cp_amb=(a+b*Tamb_K+c*Tamb_K^2+d*Tamb_K^3)/mair;    %specific heat of air
    % rho_amb = 1.225;    %Air density

```

```

rho_amb=P/Rair/(Tamb_K);      %air density
% mu_amb = 18*10^(-6);      %Air viscosity
%Sutherland's Law
%0.0000171*((Tamb_K/273)^1.5)*((273+110.4)/(Tamb_K+110.4)); %
mu_amb= 0.0000017531+6.6382*10^(-8)*Tamb_K-3.8934*10^(-11)*Tamb_K^2+1.2279*10^(-
14)*Tamb_K^3; %air viscosity
% k_amb = 0.0247;          %Air conductivity
c1=0.00000000015207;
c2=0.000000048574;
c3=0.00010184;
c4=-0.00039333;
k_amb=c1*Tamb_K^3+c2*Tamb_K^2+c3*Tamb_K+c4; %air conductivity
Pr_amb = cp_amb*mu_amb/k_amb*1000; %prandlt number

cv = 100; %number of control volumes
sigma = 5.67E-8;

A = L*W; %area of BIPVT
Ac = W*D; %cross-sectional area of BIPVT
Dh = 4*Ac/(2*D+2*W); %hydraulic

e1=0.8; %glass emissivity
e2=0.9; %PV emissivity
e3=0.8; %insulation emssivity

ab=0.92;
ts=0.95;
ab_bk = 0.39; %absortance of BIPVT
efficiency_ref = 0.153; %efficiency of typical STPV % 0.153; %PV efficiency
epvg=0.85;
ts_bk = 0.92; %0.92; %transmittance of BIPVT backsheet (low-iron glass
transmittance
ag= 0.95; %zero when using opaque BIPV, absorptance of glass of the pv
module
tg= 0.9; %zero when using Opaque BIPV, transmissitance of glass of the pv
module

Rpv=0.00099;
Rpv=0.0042; %*3.6; %thermal resistance top cover
R23=0.9; %insulation resistance

% m_kg_m2hr = 20; %specific mass flow rate through channel

pins=(1-tg)*0.9; %reflectance of the insulation (back), equation from Miyazaki
(2005)
Acv = L/cv*W; %effective area of PV, equation from Miyazaki (2005)
R12=0.0072; %substrate resistance
m_kg_hr =20*A; % m_kg_m2hr*A;% m_kg_m2hr*A; %mass flow rate through channel
V = m_kg_hr/3600/rho_amb/Ac; %air velocity in channel
Re_amb = rho_amb*V*Dh/mu_amb; %Reynold's number for ambient temperature
h=(3*Vwind+2.8);

```

```

ho = repmat(h,1,cv); %wind driven convection coefficient
dx = L/cv;           % CV length
h = 1:cv;
x = h*dx;
if Re_amb<2300
    Nu_top=0.6883*Re_amb^(0.7)*Pr_amb^(0.8)*exp(-
(x).^(0.3)/(6.45*Dh))+0.0124*Re_amb^0.7*Pr_amb^0.8;
    Nu_bot=50*Re_amb^0.5*Pr_amb^0.2*exp(-
(x).^(0.3)/(1.37*Dh))+0.428*Re_amb^0.5*Pr_amb^0.2;
else
    Nu_top=8.188*Re_amb^0.77*Pr_amb^3.85*exp(-
(x).^(0.2)/(2.8*Dh))+0.061*Re_amb^0.77*Pr_amb^3.85;
    Nu_bot=4.02*Re_amb^1.09*Pr_amb^19.3*exp(-
(x).^(0.2)/(14*Dh))+0.005*Re_amb^1.09*Pr_amb^19.3;
end
%Convection coefficient based on ambient temperature
hc_top = Nu_top*k_amb/Dh;
hc_bot = Nu_bot*k_amb/Dh;

T_PV= zeros(1,cv); %temperature of the cell
Tin= zeros(1,cv); %temperature at the inlet of each control volume
% Tb= zeros(1,cv); %back surface temperature

Tf= zeros(1,cv); %fluid temperature (in BIPVT cavity)
T1= zeros(1,cv); %temperature of the top channel surface
T2= zeros(1,cv); %temperature of the bottom channel surface

Q_elec_cv = zeros(1,cv); %electricity generated
% S_pv_cv=zeros(1,cv); %irradiance absorbed by the PV
Q_th_cv = zeros(1,cv); %thermal energy generated
hrad = zeros(1,cv); %radiation convection
% hrad_sky = zeros(1,cv); %sky radiation convection
% hrad_sur = zeros(1,cv); %BIPVT surface radiation convection
nth=zeros(1,cv); %thermal efficiency
hrad_b = zeros(1,cv);
hrad_T = zeros(1,cv);
T_PVg = zeros(1,cv);
hconvb=30;
Tb=Tzone;
Tradb=Tzone;
T3= zeros(1,cv);

for i=1:cv
T_PV(1,i) = Tamb;
T_PVg(1,i) = Tamb;
T1(1,i) = Tamb;
T2(1,i) = Tamb;
T3(1,i) = Tamb;

```

```

if i==1
Tin(1,i) = Tamb;
else
Tin(1,i) = Tf(1,i-1);
end
error=1;
while abs(error)>=0.00001
T_previous = T_PV(1,i);
% efficiency=efficiency_ref;
if isnan(T_PV(1,i))
T_PV(1,i)=Tamb;
end
efficiency=(efficiency_ref)*(1+coeff_effPV*(T_PV(1,i)-25));
Q_elec_cv(1,i)= G*(efficiency*W*L/cv);
%
%equations from Véronique based on BIPVT (opaque)
S=(ab*ts*G*Fcell-efficiency*G)*(W*L/cv);
S1=ag*G*(1-Fcell)*(W*L/cv)*tg^2;

%equations from Yang (2015) PhD thesis for both BIPVT and STPV
% S=G*Acv*Fcell*ab+G*Acv*(1-Fcell)*ag+G*Acv*(1-Fcell)*tg*pins*ab-Q_elec_cv(1,i);
% S1=G*Acv*(1-Fcell)*ag*tg^2;
% S_tot_cv=G*Acv*Fcell*ab*ts+G*Acv*(1-Fcell)*ag+G*Acv*(1-Fcell)*tg*pins*ab;
%Stratos Rounis' equations
% S_tot_cv =ts*ab*G; % Total solar radiation absorbed in CV
% Q_elec_cv(1,i) = (efficiency*(1+coeff_effPV*(T_PV(1,i)-25)))*G*W*L/cv; % Converted
to electricity
% S_pv_cv(1,i) = S_tot_cv - Q_elec_cv(1,i); % Absorbed by PV layer

%radiative coefficient between top surface and bottom surface of channel
%
hrad(1,i)=0.75*sigma.*(((T2(1,i)+273.15)^2+(Tb(1,i)+273.15)^2).*(T2(1,i)+273.15+Tb(1,
i)+273.15))/((1/e2)+(1/e3)-1);
%
hrad_sky(1,i)=Fsky*e1*sigma.*((T1(1,i)+273.15)^2+(Tsky+273.15)^2).*(T1(1,i)+273.15+Ts
ky+273.15);
%
hrad_sur(1,i)=Fgn*e1*sigma.*((T1(1,i)+273.15)^2+(Tsur+273.15)^2).*(T1(1,i)+273.15+Tsu
r+273.15);
%
hrad(1,i)=0.75*sigma.*(((T2(1,i)+273.15)^2+(T1(1,i)+273.15)^2).*(T2(1,i)+273.15+T1(1,
i)+273.15))/((1/e2)+(1/e3)-1);
hrad_b(1,i)=e3*sigma.*(((T3(1,i)+273.15)^2+(Tzone+273.15)^2)*((T3(1,i)+273.15)+(Tzone
+273.15)));
hrad_T(1,i)=sigma*epvg.*(((T_PVg(1,i)+273.15)^2+(Tsur+273.15)^2)*((T_PVg(1,i)+273.15)
+(Tsur+273.15)));
% Veronique's Delisle's equations
fp=ho(1,i)*Rpvg+hrad_T(1,i)*Rpvg+1;
gp=1/Rpv+1/Rpvg-1/(Rpvg*fp);
hp=1+hrad_b(1,i)*R23+hconvb*R23;

```

```

jp=1/R23-1/(R23*hp)+hrad(1,i)+hc_bot(1,i);
mp=1-1/(gp*Rpv)+hrad(1,i)*Rpv+hc_top(1,i)*Rpv-hrad(1,i)*hrad(1,i)*Rpv/jp;
T_PVg(1,i)=(ho(1,i)*Rpv*gp*Tamb+hrad_T(1,i)*Rpv*gp*Tsur+T_PV(1,i))/fp;
T_PV(1,i)=S/(gp*W*L/cv)+T1(1,i)/(gp*Rpv)+ho(1,i)*Tamb/(gp*fp)+hrad_T(1,i)*Tsur/(gp*fp);
T3(1,i)=(T2(1,i)+hconvb*R23*Tb+hrad_b(1,i)*R23*Tradb)/hp;
T2(1,i)=hc_bot(1,i)*Tf(1,i)/jp+hrad(1,i)*T1(1,i)/jp+hconvb*Tb/(hp*jp)+hrad_b(1,i)*Tradb/(hp*jp);
T1(1,i)=S1*Rpv/(mp*W*L/cv)+S/(gp*mp*W*L/cv)+hrad_T(1,i)*Tsur/(mp*gp*fp)+ho(1,i)*Tamb/(gp*mp*fp)+Rpv*hrad_b(1,i)*hrad(1,i)*Tradb/(hp*jp*mp)+hconvb*hrad(1,i)*Rpv*Tb/(hp*jp*mp)+Rpv*hrad(1,i)*hc_bot(1,i)*Tf(1,i)/(jp*mp)+hc_top(1,i)*Rpv*Tf(1,i)/(mp);
aa=-hc_bot(1,i)-
hc_top(1,i)+hc_top(1,i)*hc_top(1,i)*Rpv/mp+hc_bot(1,i)*hrad(1,i)*hc_top(1,i)*Rpv/(jp*mp)+Rpv*hrad(1,i)*hc_bot(1,i)*hc_top(1,i)/(jp*mp)+hc_bot(1,i)*hc_bot(1,i)/jp+hc_bot(1,i)*hrad(1,i)*Rpv*hrad(1,i)*hc_bot(1,i)/(jp*jp*mp);
cc=(S1*Rpv/(W*L/cv*mp)+S/(gp*mp*W*L/cv)+hrad_T(1,i)*Tsur/(gp*fp*mp)+ho(1,i)*Tamb/(gp*fp*mp)+Rpv*hrad_b(1,i)*hrad(1,i)*Tradb/(hp*jp*mp)+hconvb*hrad(1,i)*Rpv*Tb/(hp*jp*mp))*(hc_top(1,i)+hc_bot(1,i)*hrad(1,i)/jp)+hc_bot(1,i)*hrad_b(1,i)*Tradb/(hp*jp)+hc_bot(1,i)*hconvb*Tb/(hp*jp);
Tf(1,i)=(Tin(1,i)+cc/aa).*exp(W*aa*L/cv/m_kg_hr/cp_amb)-cc/aa;

```

```

%These are more simplified equations that Stratos Rounis uses

```

```

%
Tf(1,i)=(hc_top(1,i).*T2(1,i)+hc_bot(1,i).*Tb(1,i))./(hc_top(1,i)+hc_bot(1,i))+
(Tin(1,i)-(hc_top(1,i).*T2(1,i)+hc_bot(1,i).*Tb(1,i))./(hc_top(1,i)+hc_bot(1,i))).*exp(-
W.*(L/cv).*(hc_top(1,i)+hc_bot(1,i))./(m_kg_hr*cp_amb/3600));
%
Tb(1,i)=(Tf(1,i).*hc_bot(1,i)+T2(1,i).*(hrad(1,i))+((1/R23))*Tzone)./(hc_bot(1,i)+(hrad(1,i))+
(1/R23));
%
T1(1,i)=(ho(1,i).*Tamb+((1/Rpv)).*T_PV(1,i)+(hrad_sky(1,i)).*(Tsky)+(hrad_sur(1,i)).*(Tsur)).
/(ho(1,i)+((1/Rpv))+hrad_sky(1,i))+hrad_sur(1,i));
%
T_PV(1,i)=(((1/Rpv)).*T1(1,i)+((1/R12)).*T2(1,i)+S_pv_cv(1,i)/(W*L/cv))./(((1/Rpv))+
(1/R12)));
%
T2(1,i)=(((1/R12)).*T_PV(1,i)+hc_top(1,i).*Tf(1,i)+(hrad(1,i)).*Tb(1,i))./(((1/R12))+
hc_top(1,i)+hrad(1,i));
if isnan(Tf(1,i))
Tf(1,i)=Tamb;
end
Q_th_cv(1,i)=m_kg_hr/3600*cp_amb*(Tf(1,i)-Tin(1,i));
% m_kg_hr_o=m_kg_hr;
nth(1,i)=Q_th_cv(1,i)/(G*W*L/cv);
% nth(1,i)=(m_kg_hr_o*cp_amb*(Tf(1,i)-Tin(1,i)))+(m_kg_hr_o-m_kg_hr)*cp_amb*(Tin(1,i)-
Tamb))/(G*Ac*3600)*100;
%nth(1,i)=(m_kg_hr*cp_amb*(Tf(1,i)-Tin(1,i)))/(G*Ac*3600)*100;
error=(T_PV(1,i)-T_previous)/T_previous;
end
end
Q_elec_out=sum(Q_elec_cv)/3600;
Q_th_out=sum(Q_th_cv)/3600;

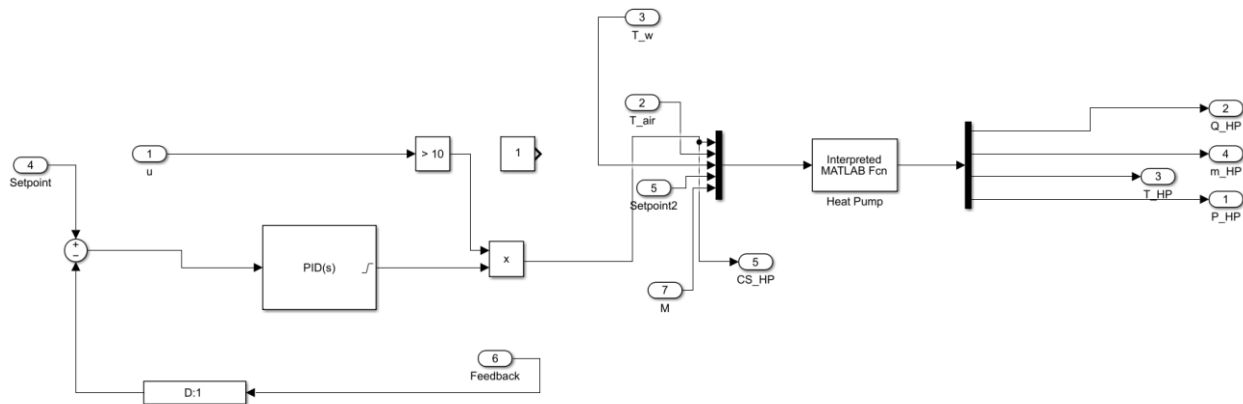
```

```

if isnan(T_PV(1,cv))
% T_PV_out=Tamb;
Tf_out=Tamb;
else
% T_PV_out=sum(T_PV)/cv;
if Tf(1,cv)>40
Tf_out=40;
else
Tf_out=Tf(1,cv);
end
end
end

```

MATLAB Code: Heat Pump



Importing Performance to MATLAB Code

```

function output_array = heat_pump6(input_array) %Tamb,Twater_in,CS_heating,m_water)
cs=input_array(1);
Tair_in=input_array(2);
Tw_in=input_array(3);
setpoint=input_array(4);
M=input_array(5);

if cs>=0.2
    if cs<0.2
        cs=0.2;
    end
    m_hp=500*cs*M;
    m_evap=193.4*cs/0.6*M;
    if Tair_in > 30
        Tair_in = 30;
    end

    values=py.heat_pump_model.specs(setpoint,cs*100,Tw_in,Tair_in,m_hp,m_evap);

    T_evap_out=values{1};
    T_HP=values{2};

```

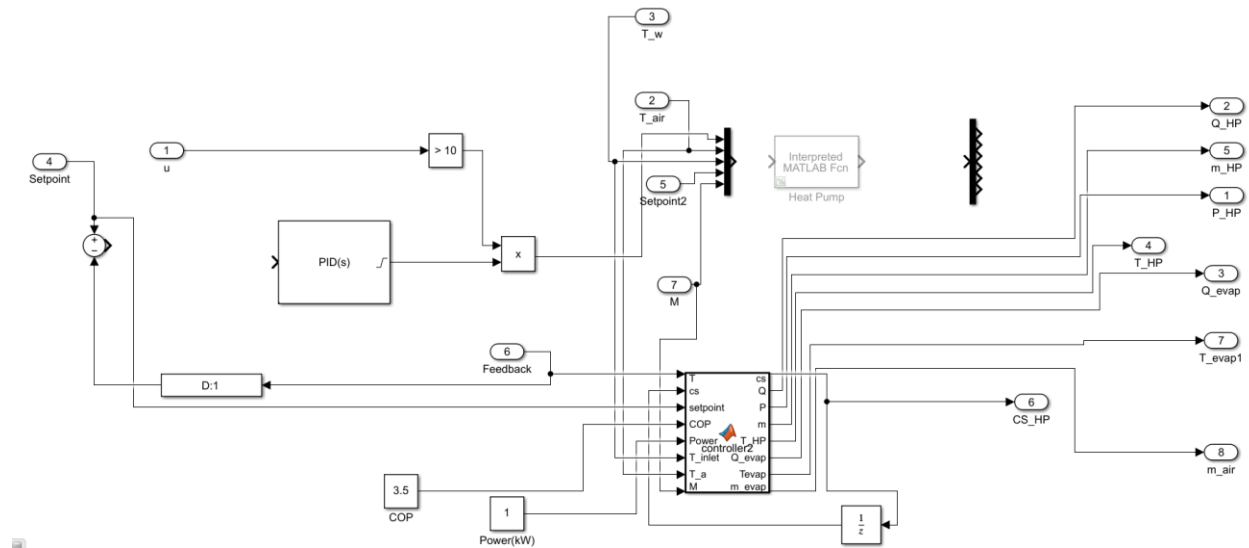
```

    if T_HP>70
        T_HP=70;
    end
    Q_HP=values{3}*M;
    Q_evap=values{4}*M;
    W=values{5}*M;
    %     if Q_evap>30
    %         Q_evap=Q_evap/10000;
    %         T_evap_out=Tair_in-3;
    %     end
    Q_evap=Q_HP-W;
    T_evap_out=Tair_in-Q_evap/m_evap*3600;
else
    m_hp=0;
    T_evap_out=Tair_in;
    T_HP=Tw_in;
    Q_HP=0;
    Q_evap=0;
    W=0;
end

output_array=[Q_HP,m_hp,T_HP,W,Q_evap,T_evap_out];

```

Verification Code



```

function [cs,Q,P,m,T_HP,Q_evap,Tevap,m_evap] =
controller2(T,cs,setpoint,COP,Power,T_inlet,T_a,M)
% T_sp=25;
delta_T=1; %deadband of temperature setpoint
T_high=setpoint+delta_T;
T_low=setpoint-delta_T;

if T>=T_high
    cs=0;

```

```

elseif T<=T_low
    cs=1;
end
W=0.008;
T_inlet=T_inlet*9/5+32;
T_a=T_a*9/5+32;
COP=15.4+2.14*10^(-5)*T_inlet^2+1.42*T_a*W-8.57*10^(-5)*T_a*T_inlet-1.08*W*T_inlet-
2.51*log(T_inlet)+0.76*log(T_a*W);
P=(T_inlet*0.008+0.16)*cs*M;
Q=COP*P*cs*M;

m=150*cs*M;
T_inlet=(T_inlet-32)*5/9;
T_a=(T_a-32)*5/9;

Q_evap=Q-P;
m_evap=210*cs*M;
if cs==0
    T_evap=T_a;
    T_HP=T_inlet;
else
    T_evap=T_a-Q_evap/m_evap/4.19*3600;
    T_HP=T_inlet+Q/m/4.19*3600;
end

```

Python Code: Heat Pump Model

```

def specs(setpoint,freq,T_cond_in,T_evap_in,m_cond,m_evap):
    from CoolProp.CoolProp import PropsSI
    import math
    T_evap_in=T_evap_in+273.15
    T_cond_in=T_cond_in+273.15
    fluid='R134a'
    rated_fan_power=0.07

    cp_cond=4.19
    cp_evap=1

```

```

superheat_hx=1
mode=1
rated_air_flow=193.4
if mode==1 or mode==2 or mode==5:
    fan_power=rated_fan_power*(m_evap/rated_air_flow)**3
else:
    fan_power=rated_fan_power*(m_cond/rated_air_flow)**3

# subcool=0.1
superheat=0.1

#swept volume
vc=0.00002

eff_evap=0.7
eff_cond=0.96
eff_hx=0.8
subcool=2
W_old2=1
Q_old=3.75

# T3=30+273.15

T3=(T_cond_in-273.15)*1.0764+4.444+273.15

w=6000*freq/100
quality_0=1
quality_3=1
quality_8=1
if mode==3 or mode==4:

```

```

    T0=(T_evap_in-273.15)*0.841-6.792+273.15
else:
    T0=(T_evap_in-273.15)*0.841-8.387+273.15
p1=PropsSI('P','T',T0,'Q',quality_0,fluid)

p2=PropsSI('P','T',T3,'Q',quality_3,fluid)
pvap=(p2*p1)**0.5
if pvap<p1*1.6:
    pvap=p1*1.6
elif pvap>2.3*1000*1000:
    pvap=2.3*1000*1000
error=1
h_5=245376.88
T6=T0
cp_r6=PropsSI('C','T',T6,'Q',0,fluid)/1000
density_3=PropsSI('D','P',p2,'Q',quality_3,fluid)
T9=PropsSI('T','P',pvap,'Q',quality_8,fluid)
h_9=PropsSI('H','P',pvap,'Q',quality_8,fluid)
h_0=PropsSI('H','P',p1,'Q',quality_0,fluid)
T1=T0+superheat
count=1
p_ratio=p2/p1
if T_evap_in<=273.15:
    vap=0
else:
    vap=0

while error>0.0001:
# while count<50:
    T1_old=T1

```

```

density_1=PropsSI('D','P',p1,'T',T1,fluid)
cp_r1=PropsSI('C','P',p1,'T',T1,fluid)/1000
h_1=PropsSI('H','P',p1,'T',T1,fluid)
s1=PropsSI('S','P',p1,'T',T1,fluid)

if mode==3 or mode==4:
    eff_v=0.0017*(p_ratio)**2-(0.0005*freq-0.0663)*p_ratio+0.9462
else:
    eff_v=0.0017*(p_ratio)**2-(0.0005*freq-0.0663)*p_ratio+0.8932
m_r=vc*density_1*w*60*eff_v
m_t=m_r/0.9
if vap==1:
    m_vap=0.1*m_t
else:
    m_vap=0
    m_t=m_r
cp_r0=PropsSI('C','P',p1,'Q',quality_0,fluid)/1000

c0=0.9646
c1=0.095
c2=1.387
c3=1.553

if mode==3 or mode==4:
    eff_isen=(c0*np.exp(-c1*(p_ratio-c2)))/(1+np.exp(-c3*(p_ratio-c2)))+0.04
else:
    eff_isen=(c0*np.exp(-c1*(p_ratio-c2)))/(1+np.exp(-c3*(p_ratio-c2)))+0.02

if mode==3 or mode==4:

```

```

cmin1=min((m_t)*cp_r6,m_evap*cp_evap)
Q_evap2=cmin1*eff_evap*(T_evap_in-T6)/3600
Q_evap=(m_t)*(h_1-h_5)/1000/3600
else:
cmin1=min((m_r)*cp_r6,m_evap*cp_evap)
Q_evap2=cmin1*eff_evap*(T_evap_in-T6)/3600
Q_evap=(m_r)*(h_1-h_5)/1000/3600

T_air_out=T_evap_in-Q_evap/(m_evap*cp_evap)*3600-273.15

h_2_isen=PropsSI('H','P',p2,'S',s1,fluid)

W_isen=m_t*(h_2_isen-h_1)/1000/3600

W_old=W_isen/eff_isen
h_dis=W_old/m_t*1000*3600+h_1
T_2temp=PropsSI('T','P',p2,'H',h_dis,fluid)
n=1/(1-math.log(T_2temp/T1)/math.log(p2/p1))

if vap==1:
T2_vap=T1*(pvap/p1)**((n-1)/n)
h_vap=PropsSI('H','P',pvap,'T',T2_vap,fluid)
h_10=(h_vap*(m_r)+h_9*m_vap)/(m_t)
T10=PropsSI('T','H',h_10,'P',pvap,fluid)-5
T2=T10*(p2/pvap)**((n-1)/n)

quality_2=PropsSI('Q','P',pvap,'T',T2,fluid)
cp_r2=PropsSI('C','P',pvap,'T',T2,fluid)/1000
h_2=PropsSI('H','P',pvap,'T',T2,fluid)
else:

```

```

T2=T1*((p2/p1)**((n-1)/n))
density_2=PropsSI('D','P',p2,'T',T2,fluid)

h_2=PropsSI('H','P',p2,'T',T2,fluid)
cp_r2=PropsSI('C','P',p2,'T',T2,fluid)/1000

if vap==1:
    W_comp=((m_r)*(h_vap-h_1)+(m_t)*(h_2-h_vap))/1000/3600
else:
    W_comp=(m_r)*(h_2-h_1)/1000/3600

if mode==1 or mode==3:
    Q_dhw=0;

T3=PropsSI('T','P',p2,'Q',quality_3,fluid)
try:
    cp_r3=PropsSI('C','P',p2,'T',T3,fluid)/1000
    h_3=PropsSI('H','P',p2,'T',T3,fluid)
except:
    cp_r3=PropsSI('C','P',p2,'Q',quality_3,fluid)/1000
    h_3=PropsSI('H','P',p2,'Q',quality_3,fluid)

if mode==5:
    T4=PropsSI('T','P',p2,'Q',0.0,fluid)-subcool
    h_4=PropsSI('H','P',p2,'T',T4,fluid)
elif mode==2 or mode==3:
    cmin3=(min((m_t)*cp_r3,cp_cond*m_cond))
    Q_cond2=cp_cond*m_cond*eff_cond*(T3-T_cond_in)/3600
    h_4_2=h_3-Q_cond2/(m_t)*3600*1000
    T4=PropsSI('T','P',p2,'Q',0.0,fluid)-subcool

```

```

    h_4=PropsSI('H','P',p2,'T',T4,fluid)
#    h_4=PropsSI('H','P',p2,'T',T4,fluid)
else:
    cmin3=(min((m_t)*cp_r2,cp_cond*m_cond))
    Q_cond2=cp_cond*m_cond*eff_cond*(T2-T_cond_in)/3600
    h_4_2=h_3-Q_cond2/(m_t)*3600*1000
    T4=PropsSI('T','P',p2,'Q',0.0,fluid)-subcool
    h_4=PropsSI('H','P',p2,'T',T4,fluid)
q_dhw_r=0;

if vap==1:
    try:
        h_7=PropsSI('H','P',p2,'T',T4,fluid)
    except:
        h_7=PropsSI('H','P',p2,'Q',0,fluid)
        T7=PropsSI('T','P',pvap,'H',h_7,fluid)
        quality_7=PropsSI('Q','P',pvap,'H',h_7,fluid)
        cp_r7=PropsSI('C','P',pvap,'H',h_7,fluid)/1000
        if cp_r7<0 or cp_r7>20:
            cp_r7=PropsSI('C','P',pvap,'Q',quality_7,fluid)/1000

        T8=PropsSI('T','P',pvap,'Q',quality_8,fluid)
        h_8=PropsSI('H','P',pvap,'Q',quality_8,fluid)

        Q_hx=m_vap*(h_8-h_7)
        h_5=h_7-Q_hx/(m_r)

        T5=PropsSI('T','P',p2,'H',h_5,fluid)
else:
    T5=T4

```

```

h_5=h_4

T6=PropsSI('T','P',p1,'H',h_5,fluid)
quality_5=PropsSI('Q','P',p1,'H',h_5,fluid)
cp_r6=PropsSI('C','P',p1,'H',h_5,fluid)/1000
if cp_r6<0 or cp_r6>20:
    cp_r5=PropsSI('C','P',p1,'Q',quality_5,fluid)/1000
if cp_r6<0 or cp_r6>20:
    cp_r5=PropsSI('C','P',p1,'Q',0.0,fluid)/1000
if vap==1:
    T9=T8+superheat_hx
    h_9=PropsSI('H','P',pvap,'T',T9,fluid)

if mode==1 or mode==3:
    Ttemp=PropsSI('T','P',p2,'Q',0.0,fluid)-subcool
    h_temp=PropsSI('H','P',p2,'T',Ttemp,fluid)
    if mode==3:
        Q_cond=(m_r)*(h_2-h_temp)/1000/3600
    else:
        Q_cond=(m_t)*(h_2-h_temp)/1000/3600
    T_cond_out=T_cond_in+Q_cond/(cp_cond*m_cond)*3600-273.15
elif mode==2 or mode==4:
    if mode==4:
        Q_cond=(m_r)*(h_3-h_4)/1000/3600
    else:
        Q_cond=(m_t)*(h_3-h_4)/1000/3600
    T_cond_out=T_cond_in+Q_cond/(cp_cond*m_cond)*3600-273.15
T0=PropsSI('T','P',p1,'Q',quality_0,fluid)
T0=T6+Q_evap/(m_r)/cp_r6
p1_new=PropsSI('P','T',T0,'Q',quality_0,fluid)

```

```

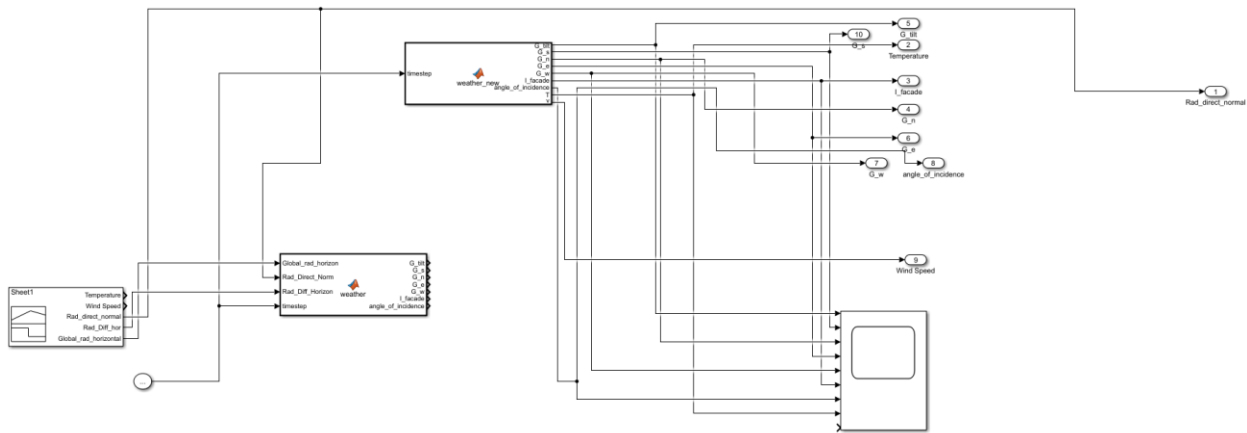
T1=T0+superheat
h_0=PropsSI('H','P',p1,'Q',quality_0,fluid)
error=abs((T1-T1_old)/T1_old)

if mode==3 or mode==4:
    cmin1=min((m_t)*cp_r6,m_evap*cp_evap)
    Q_evap2=cmin1*eff_evap*(T_evap_in-T6)/3600
    Q_evap=(m_t)*(h_1-h_5)/1000/3600
else:
    cmin1=min((m_r)*cp_r6,m_evap*cp_evap)
    Q_evap2=cmin1*eff_evap*(T_evap_in-T6)/3600
    Q_evap=(m_r)*(h_1-h_5)/1000/3600

T_evap_out=T_evap_in-Q_evap/(cp_evap*m_evap)*3600-273.15
count+=1
Q_cond=Q_cond2
p2_new=p2+1000000*((Q_cond-Q_old)/Q_cond-(W_comp-W_old2)/W_comp)
#           p2_new=(10.97995+1.06442*T_cond_out+1.01404*(T_evap_in-273.15)-
0.01216*(T_evap_in-273.15)**2)*100000
error=(abs((p2_new-p2)/p2))/2
p2=p2_new
Q_old=Q_cond
W_old2=W_comp
values=[T_evap_out,T_cond_out,Q_cond,Q_evap,W_comp]
return values

```

MATLAB Code: Weather Model



```
function [G_tilt,G_s,G_n,G_e,G_w,I_facade,angle_of_incidence,T,v]
=weather_new(timestep)
    v=1.5;
    DT=10;
    Tmean=-5;
    w1=2*pi/24;
    Hour=(timestep/3600/24-floor(timestep/3600/24))*24;
    T=Tmean+DT/2*cos(w1*Hour-1.125*pi);

    Lat=45;

    n=floor(timestep/3600/24)+1;
    % row=0.3;
    d=23.45*sind(360*(284+n)/365);
    ts=acosd(-tand(Lat)*tand(d))/15;

    ha=15*(Hour-12);
    zenith_angle=acosd(cosd(Lat)*cosd(d)*cosd(ha)+sind(Lat)*sind(d));
    % alpha=asind(cosd(Lat)-cosd(d)*cosd(ha)+sind(Lat)*sind(d))
    alpha=90-zenith_angle;
    s=(sind(alpha)*sind(Lat)-sind(d))/(cosd(alpha)*cosd(Lat));
    if s<-1
        s=-1;
    elseif s>1
        s=1;
    end
    azimuth=acosd(s)*sign(ha);
    B=90;
    angle_of_incidence=acosd(cosd(alpha)*cosd((azimuth-
0))*sind(B)+sind(alpha)*cosd(B));

    angle_of_incidence_tilt=acosd(cosd(alpha)*cosd((azimuth-
0))*sind(45)+sind(alpha)*cosd(45));
    angle_of_incidence_n=acosd(cosd(alpha)*cosd((azimuth-
180))*sind(B)+sind(alpha)*cosd(B));
```

```

angle_of_incidence_e=acosd(cosd(alpha)*cosd((azimuth+90))*sind(B)+sind(alpha)*cosd(B)
);
    angle_of_incidence_w=acosd(cosd(alpha)*cosd((azimuth-
90))*sind(B)+sind(alpha)*cosd(B));

A=0.5; %altitude (km)
r0=1.03;
r1=1.01;
rK=1.0;

a0=r0*(0.4237-0.00821*(6-A)^2);
a1=r1*(0.5055+(0.00595*(6.5-A)^2));
k=rK*(0.2711+(0.01858*(2.5-A)^2));

tb=a0+a1*exp(-k/sind(alpha));

I_on=1353*(1+0.033*cosd(360*n/365));
G_s=I_on*tb*cosd(angle_of_incidence);
G_tilt=I_on*tb*cosd(angle_of_incidence_tilt);
G_n=I_on*tb*cosd(angle_of_incidence_n);
G_e=I_on*tb*cosd(angle_of_incidence_e);
G_w=I_on*tb*cosd(angle_of_incidence_w);
if Hour<ts+2 || Hour> ts+12
    G_s=0;
    G_tilt=0;
    G_n=0;
    G_e=0;
    G_w=0;
end
if G_s>1500
    G_s=1500;
elseif G_s<0
    G_s=0;
end
if G_tilt>1500
    G_tilt=1500;
elseif G_tilt<0
    G_tilt=0;
end
if G_n>1500
    G_n=1500;
elseif G_n<0
    G_n=0;
end
if G_w>1500
    G_w=1500;
elseif G_w<0
    G_w=0;
end
if G_e>1500

```

```
        G_e=1500;
        elseif G_e<0
            G_e=0;
        end
%     if G_s<0 ||G_tilt<0 || G_n<0 || G_e<0 || G_w<0
%         G_s=0;
%         G_tilt=0;
%         G_n=0;
%         G_e=0;
%         G_w=0;
%     end
I_facade=G_s;
end
```

Appendix B: Example Parametric Analysis Output

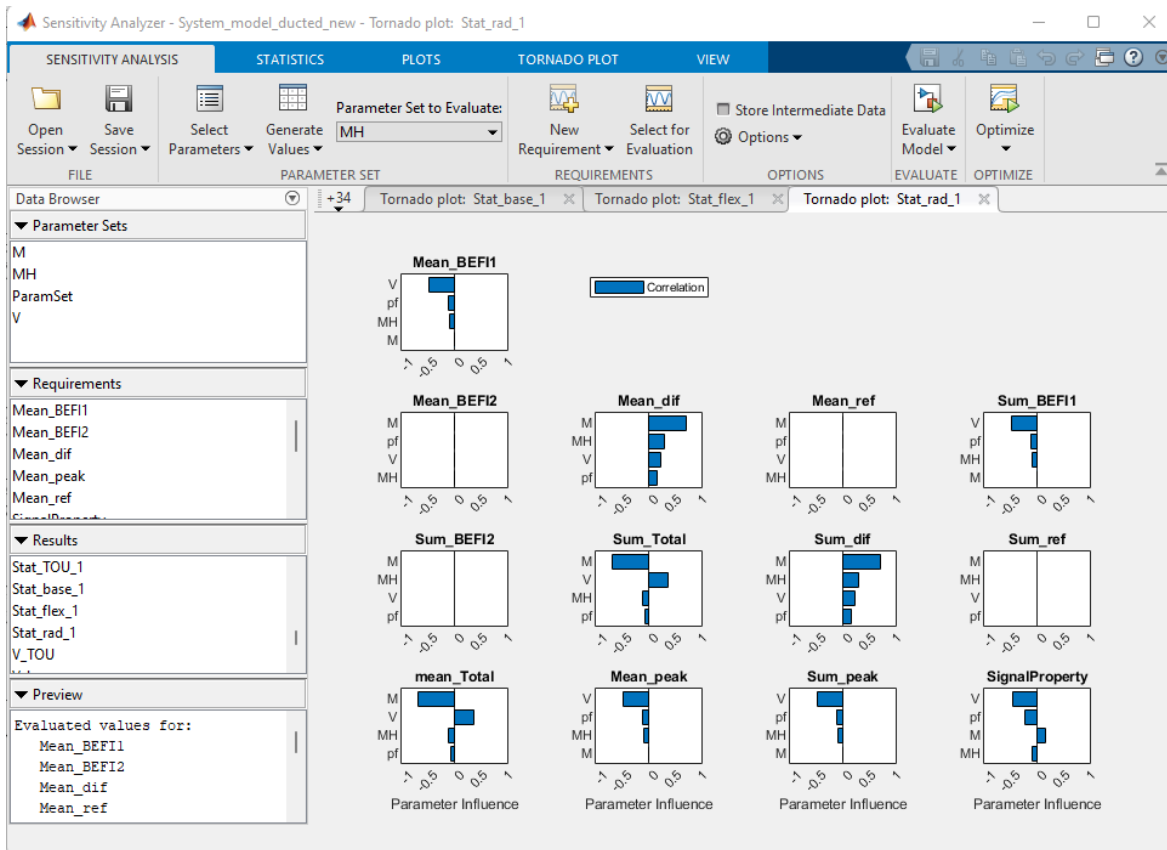


Figure B - 1: Example graphical output of the parametric analysis for daytime charging strategy in a ducted configuration

Figure B - 2 to B - 8 are the outputs received from the parametric analysis in Chapter 3. These results were used to determine the optimal values summarized in Chapter 3.2.2.2.

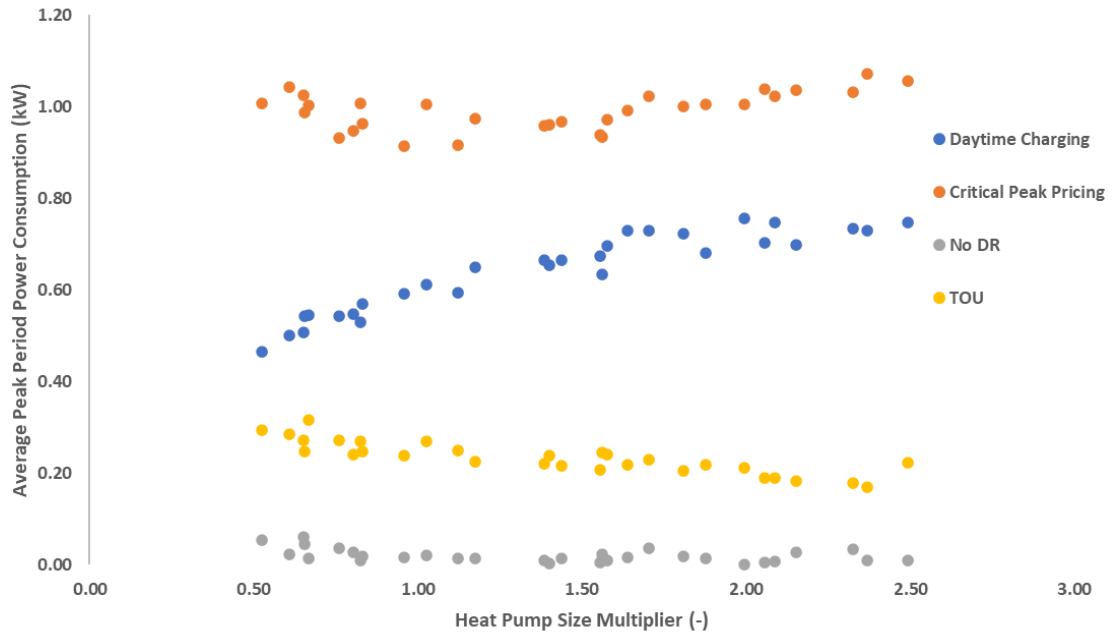


Figure B - 2: Example output from the BIPV-HPWH sensitivity analysis showing the load reduction as a function of DR strategy (described in Chapter 3.1.2.2) and relative heat pump size

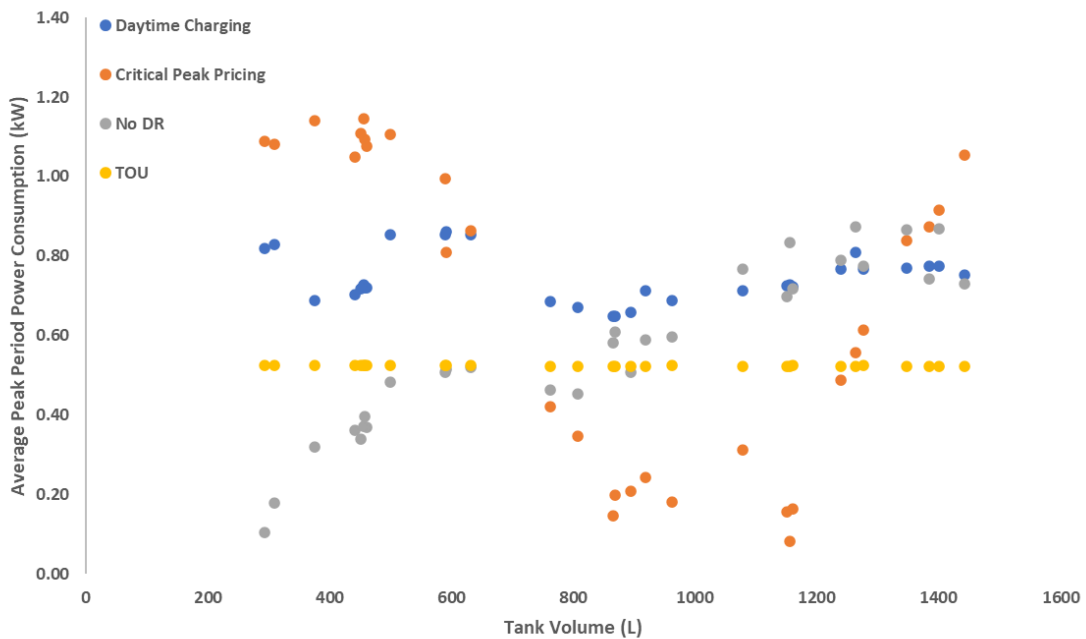


Figure B - 3: Example output from the BIPV-HPWH sensitivity analysis showing the load reduction as a function of DR strategy (described in Chapter 3.1.2.2) and tank volume

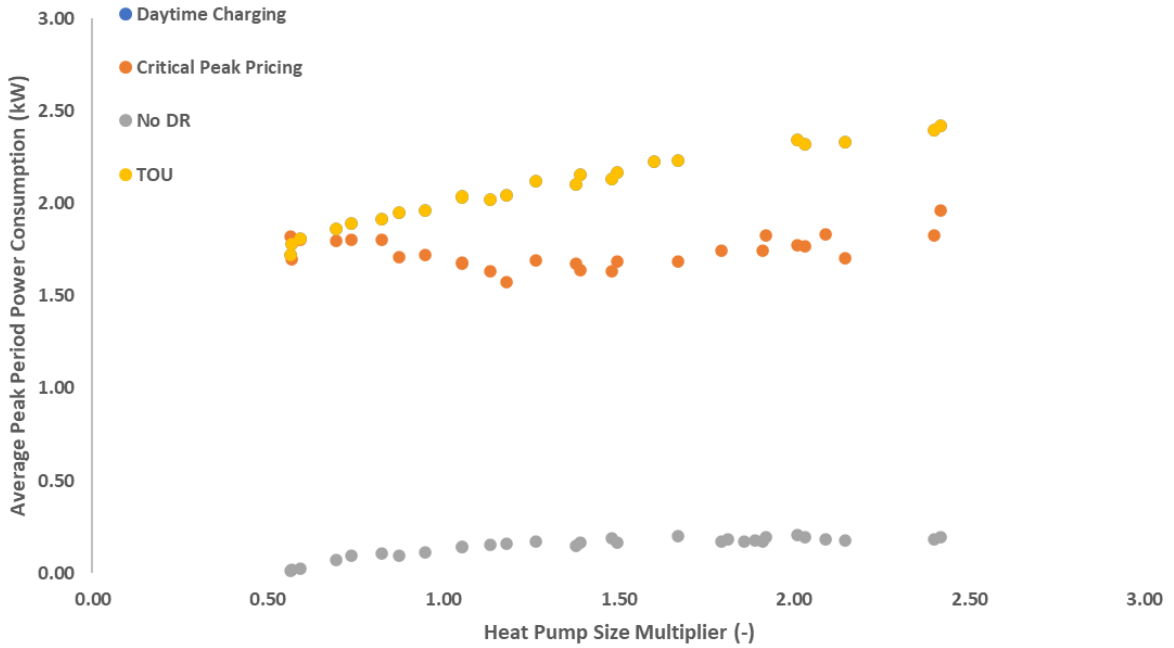


Figure B - 4: Example output from the BIPVT-HPWH sensitivity analysis showing the load reduction as a function of DR strategy (described in Chapter 3.1.2.2) and relative heat pump size

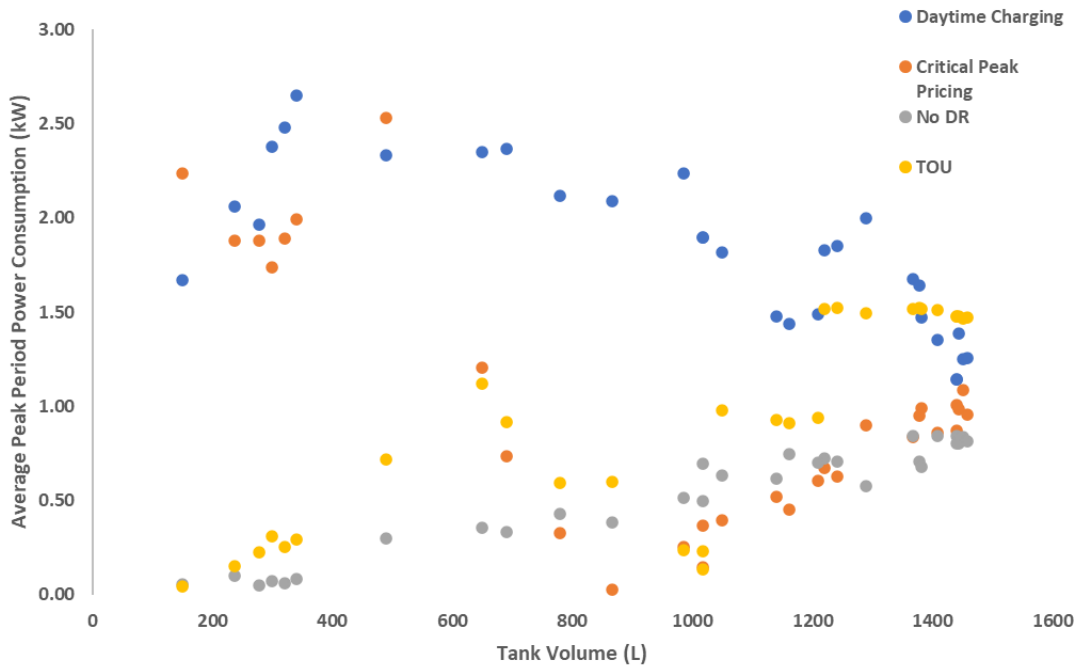


Figure B - 5: Example output from the BIPVT-HPWH sensitivity analysis showing the load reduction as a function of DR strategy (described in Chapter 3.1.2.2) and tank volume

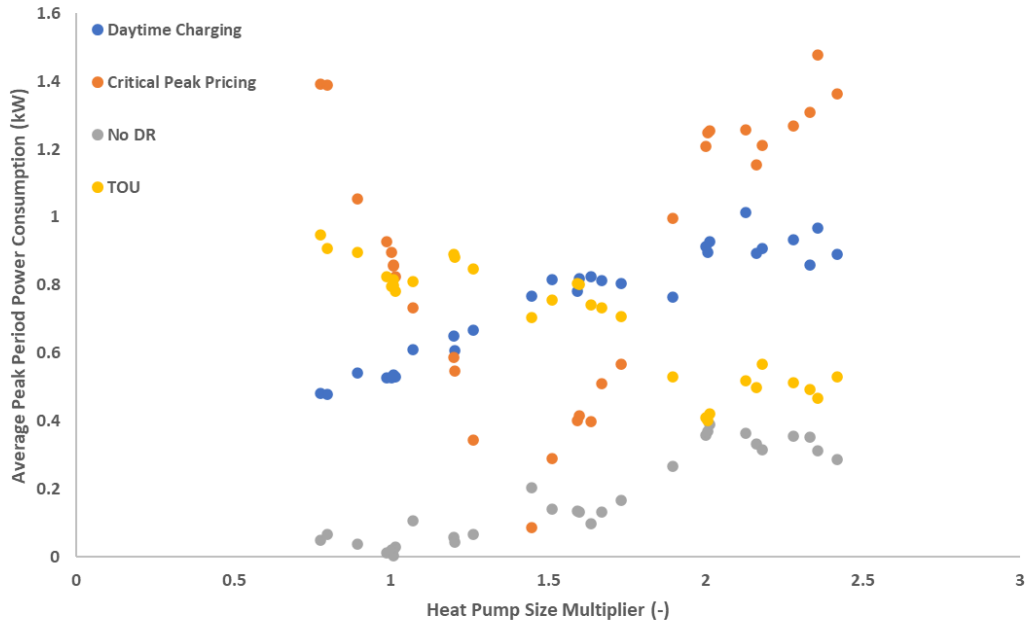


Figure B - 6: Example output from the STPV-HPWH sensitivity analysis showing the load reduction as a function of DR strategy (described in Chapter 3.1.2.2) and relative heat pump size

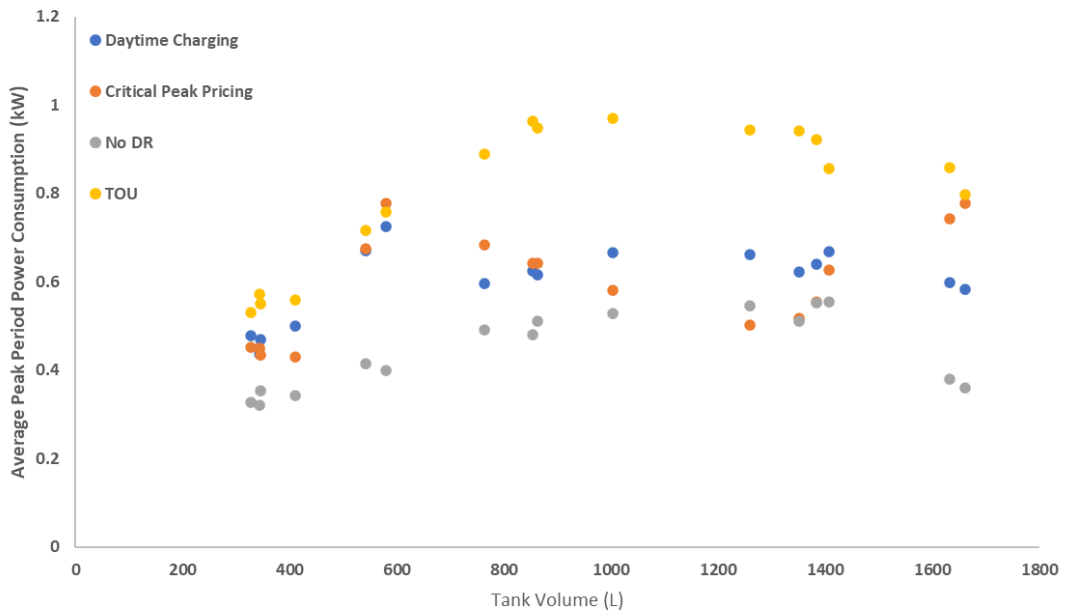


Figure B - 7: Example output from the STPV-HPWH sensitivity analysis showing the load reduction as a function of DR strategy (described in Chapter 3.1.2.2) and tank volume

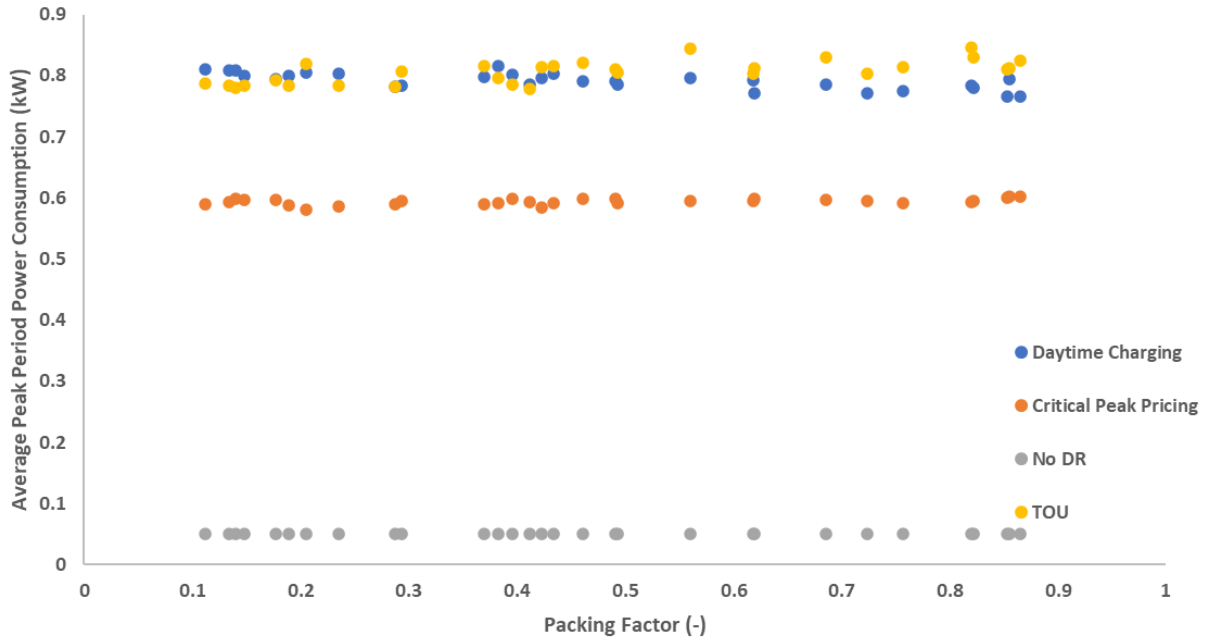


Figure B - 8: Example output from the STPV-HPWH sensitivity analysis showing the load reduction as a function of DR strategy (described in Chapter 3.1.2.2) and STPV packing factor

Appendix C: Additional Calculations Used and Verification

BIPV/T Model

Absorbed Solar Radiation Rate

The net absorbed solar radiation from the PV cells, S_{PV} , is defined as the difference between the absorbed solar radiation and the electricity produced by the PV cells, P_{PV} . It is determined with the following relation:

$$S_{PV} = GF_{cell}\alpha_{PV}\tau_{PV}WL_{CV} - P_{PV} \quad (0.1)$$

Where G is radiation incident to the BIPVT in $\text{kJ}/(\text{h}\cdot\text{m}^2)$, F_{cell} is the cell packing factor, α_{PV} is the PV cells' absorptance, τ_{PV} is the PV cells' transmittance, W is the BIPVT collector's width in m, and L_{CV} is the length of one control volume in m. The PV cells' electrical efficiency, η_{PV} , is calculated based on the simple efficiency model that states the model varies with the cell's temperature based on the temperature modifier given by the BIPV manufacturer. The efficiency is calculated by using the following relation:

$$\eta_{PV} = \eta_{PV,ref} \left(1 + \gamma_{ref}(T_{PV} - T_{PV,ref}) \right) \quad (6.2)$$

Where $\eta_{PV,ref}$ is the electrical efficiency at standard operating conditions typically corresponding to a reference PV temperature, $T_{PV,ref}$, of 25°C and reference radiation of $1000 \text{ w}/\text{m}^2$ and γ_{ref} is the temperature coefficient. The solar radiation absorbed by the PV backsheets, S_{ins} , is defined as the following:

$$S_{ins} = G\alpha_{bk}\tau_{bk}(1 - F_{cell})WL_{CV} \quad (6.3)$$

Where α_{bk} is the backsheets material absorptance and τ_{bk} is the backsheets material transmittance.

Radiative Heat Transfer Coefficients

The radiative heat transfer coefficients for the air channel, including the top, $h_{rad,t}$, and back, $h_{rad,b}$, of the collector as well as through the air channel, $h_{rad,12}$, can be calculated with the following relations.

$$h_{rad,t} = \sigma \varepsilon_1 (T_g^2 + T_{sur}^2) (T_g + T_{sur}) \quad (6.4)$$

$$h_{rad,b} = \sigma \varepsilon_3 (T_b^2 + T_{zone}^2) (T_b + T_{zone}) \quad (6.5)$$

$$h_{rad,12} = \frac{\sigma (T_1^2 + T_2^2) (T_1 + T_2)}{\frac{1}{\varepsilon_2} + \frac{1}{\varepsilon_3} + 1} \quad (6.6)$$

All temperatures are calculated in Kelvin, σ is the Stefan-Boltzmann constant, ε_1 is the PV glazing emissivity, ε_2 and ε_3 are the air channel's top and bottom surface emissivity, T_g is the PV glazing temperature in K, T_b is the back surface temperature in K, T_1 and T_2 are the top and bottom air channel temperatures in K, T_{zone} is the zone temperature in K, and the surrounding temperature, T_{sur} , can be calculated from the following equation:

$$T_{sur} = (F_{gnd} T_{gnd}^4 + F_{sky} T_{sky}^4)^{1/4} \quad (6.7)$$

Where T_{gnd} is the ground temperature in K while the following equation calculates the sky temperature:

$$T_{sky} = (0.68 + 0.0552 T_{amb,K}^{1.5}) + 0.32 T_{amb,K} - 273.15 \quad (6.8)$$

The collector's ground, F_{gnd} , and sky, F_{sky} , view factors can be calculated as a function of the BIPVT slope using the following relations:

$$F_{sky} = \frac{1 + \cos(Slope)}{2} \quad (6.9)$$

$$F_{gnd} = \frac{1 - \cos(\text{Slope})}{2} \quad (6.10)$$

Convective Heat Transfers Coefficients

The Nusselt numbers for the top and bottom of the air channel in the laminar region valid between a Reynolds number of 1190 and 2300 are calculated using the model of (Yang & Athienitis, 2014):

$$Nu_{top} = 0.6883Re^{0.7}Pr^{0.8}e^{\frac{-x^{0.3}}{6.45D_h}} + 0.0124Re^{0.7}Pr^{0.8} \quad (6.11)$$

$$Nu_{bot} = 50Re^{0.5}Pr^{0.2}e^{\frac{-x^{0.3}}{1.37D_h}} + 0.428Re^{0.5}Pr^{0.2} \quad (6.12)$$

Where Re is the Reynolds number and Pr is the Prandtl number. For the turbulent region with a Reynolds number between 2300 and 9500, the Nusselt number for the top and bottom of the air channel are determined by the following equations from Yang (2014):

$$Nu_{top} = 8.188Re^{0.77}Pr^{3.85}e^{\frac{-x^{0.2}}{2.8D_h}} + 0.061Re^{0.77}Pr^{3.85} \quad (6.13)$$

$$Nu_{bot} = 4.02Re^{1.09}Pr^{19.3}e^{\frac{-x^{0.2}}{14D_h}} + 0.005Re^{1.09}Pr^{19.3} \quad (6.14)$$

The fluid heat transfer coefficient can be obtained from the Nusselt numbers using the following equation:

$$h_c = \frac{Nu k}{D_h} \quad (6.15)$$

Where D_h is the hydraulic diameter in m defined as:

$$D_h = \frac{4 W D}{2 W + 2 D} \quad (6.16)$$

The wind-driven top convective heat transfer coefficient is calculated using Duffie & Beckman's model (Duffie, Beckman, & W.M., 2003). This model is generally used for the simulation of glazed collectors.

$$h_o = 3V_{wind} + 2.8 \quad (6.17)$$

Heat Transfer Equations

The rate of thermal and electrical energy produced by the BIPVT system can be calculated with the following relations:

$$Q_{th} = Nb_{cols} \dot{m}_{air} C_{p,air} (T_f - T_{in}) \quad (6.18)$$

$$P_{PV} = G W L \alpha_{PV} \tau_{PV} Nb_{rows} Nb_{cols} \eta_{PV} \quad (6.19)$$

The BIPVT system's thermal and electrical efficiencies are given as:

$$\eta_{th} = \frac{Q_{th}}{G W L Nb_{rows} Nb_{cols}} \quad (6.20)$$

$$\eta_{el} = \frac{P_{PV}}{G W L Nb_{rows} Nb_{cols}} \quad (6.21)$$

BIPV and STPV Models

The STPV and BIPV electrical models were calculated from King's model (ASHRAE, 2019), the equations are as follows:

$$T_{back} = c \cdot G \cdot e^{(a+b \cdot V)} + T_a \quad (6.22)$$

$$T_{cell} = T_{back} + \frac{G}{G_0} \cdot \Delta T \quad (6.23)$$

$$P = \eta_{ref} \cdot (1 + \mu_{mp} \cdot (T_{cell} - T_{ref})) \cdot G \cdot A \quad (6.24)$$

Where T_{back} , T_{cell} , and T_{ref} are the back-surface, PV operation cell, and reference cell temperatures, respectively. T_a is the ambient temperature while ΔT is the temperature difference between the cell and back-surface temperatures. G and G_0 are the incident and reference solar irradiation on the BIPV/STPV modules, respectively. A is the BIPV/STPV module area. V is the wind speed. η_{ref} is the reference electrical efficiency and μ_{mp} is the temperature coefficient at maximum power point. c , b , and a are correction and empirically determined coefficients provided in ASHRAE for different PV technologies. The coefficients used for the STPV windows were for a BIPV window and the coefficients for the BIPV on the rooftop were for BIPV with poor ventilation.

Building Model

Double Glazed Windows

The window areas used are determined based on a fixed window-to-wall ratio (WWR) for each façade. The WWR values are 10% for north and 20% for east and west.

The windows within the house and solarium are double glazed, therefore the amount of solar irradiation transmitted indoors was determined based on the equations outlined in (Athienitis, 1998):

$$\theta' = \text{asin}\left(\frac{\sin(\theta)}{n_g}\right) \quad (6.25)$$

$$r = \frac{1}{2} \left(\left(\frac{\sin(\theta - \theta')}{\sin(\theta + \theta')} \right)^2 + \left(\frac{\tan(\theta - \theta')}{\tan(\theta + \theta')} \right)^2 \right) \quad (6.26)$$

$$a = \exp \left(\left(\left(- \frac{kL}{\sqrt{1 - \left(\frac{\sin(\theta)}{n_g} \right)^2}} \right) \right) \right) \quad (6.27)$$

$$\tau = \frac{(1-r)^2 a}{1-r^2 a^2} \quad (6.28)$$

$$\rho_o = r + \frac{r(1-r)^2 a^2}{1-r^2 a^2} \quad (6.29)$$

$$\alpha_s = 1 - \rho_o - \tau \quad (6.30)$$

$$\tau_{eff} = \frac{\tau^2}{1 - \rho_o^2} \quad (6.31)$$

Shades

Shades are applied within the solarium, the shades (when down) will emit heat into the room, the following equation compares with effect ((Athienitis, 1998), (Bastien & Athienits, 2012), (Bastien & Athienits, 2010)):

$$S = (1 - cs) \cdot \alpha \cdot I \cdot A_w + cs \cdot \alpha \cdot \alpha_{blind} \cdot I \cdot A_{blind} \quad (6.32)$$

Where cs is the control signal for the blinds, α is the absorptance of the windows, α_{blind} is the absorptance of the blinds, I is the solar irradiation incident on the façade in W/m^2 , A_w is the window area in m^2 , and A_{blind} is the area of the blinds in m^2 .

Heat Pump Model

Compressor

The volumetric efficiency is modelled based on a variable speed scroll compressor used by Yang et al. (Yang, Zhao, Zhang, & Gu, 2009). There are currently no compressor curves available in the literature for the specific type of compressor used in this application. In the absence of isentropic curves or relations provided by the compressor manufacturer, the isentropic efficiency is calculated with a relation found in literature for a scroll compressor ((Deschesne, Tello-Oquendo, Gendebien, & Lemort, 2019), (Underwood, Royapoor, & Sturm, 2017)). The isentropic efficiency relation, η_{isen} , and refrigerant flow rate for the compressor inlet, \dot{m}_r , can be calculated using the following equations:

$$\eta_{isen} = \frac{c_0 \exp(-c_1(P_{ratio} - c_2))}{1 + \exp(-c_3(P_{ratio} - c_2))} \quad (6.33)$$

$$\eta_v = 0.0017P_{ratio}^2 - (0.0005f - 0.0663)P_{ratio} + 0.9862 \quad (6.34)$$

$$\dot{m}_r = \frac{V_s \omega \eta_v \rho_1}{60} \quad (6.35)$$

$$\omega = f * 60 \quad (6.36)$$

Where the empirical correlations c_0 , c_1 , c_2 , c_3 used within equation (6.33) were fitted to a compressor tested by Underwood et al. (Underwood, Royapoor, & Sturm, 2017) and found in Table C - 1.

Table C - 1: Fitting parameters for a scroll compressor found in Underwood et al. [3]

Coefficient	0	1	2	3
c_i	0.9646	0.095	1.387	1.553

The isentropic work, W_{isen} , is calculated using the ideal value of the enthalpy exiting the compressor, $h_{2,isen}$. The ideal enthalpy can be calculated by assuming a constant entropy during the compression process. The isentropic power can be used, along with the efficiency, to calculate

the actual power input to the compressor. The polytropic compression index, n , is recalculated and used within equation (6.39).

$$W_{isen} = \dot{m}_r(h_{2,isen} - h_1) \quad (6.37)$$

$$W_{comp} = \frac{W_{isen}}{\eta_{isen}} \quad (6.38)$$

The refrigerant temperature at the compressor outlet, T_2 , as well as the compressor and total power can be calculated as follows:

$$T_2 = T_1 \left(\frac{P_2}{P_1} \right)^{\frac{(n-1)}{n}} \quad (6.39)$$

$$W_{comp} = \dot{m}_r(h_2 - h_1) \quad (6.40)$$

$$\dot{m}_T = \dot{m}_r \quad (6.41)$$

$$W_{total} = W_{comp} + W_{fan} \quad (6.42)$$

The fan power, W_{fan} , is assumed to have a cubic relation with the fan's mass flow rate as seen in equation (6.43) (ASHRAE, 2018).

$$W_{fan} = \left(\frac{\dot{m}_{fan}}{\dot{m}_{fan,rated}} \right)^3 \quad (6.43)$$

Evaporator Heat Exchanger

The evaporator capacity, Q_{evap} , can be found using the following equations.

$$Q_{evap} = C_{min} \varepsilon_{evap} (T_{wi} - T_1) \quad (6.44)$$

$$C_{min} = MIN(\dot{m}_r C_{p,6}, \dot{m}_{evap} C_{p,evap}) \quad (6.45)$$

$$Q_{evap} = \dot{m}_r(h_1 - h_4) \quad (6.46)$$

The refrigerant temperature leaving the evaporator, T_0 , is obtained using CoolProp with the assumption that the quality at this point is 1. The temperature entering the compressor, T_1 , is recalculated using:

$$T_{1,new} = T_0 + \Delta T_{superheat} \quad (6.47)$$

Condenser Heat Exchanger

The condenser capacity can be found using the following equations:

$$Q_{cond} = C_{min}\varepsilon_{cond}(T_3 - T_{cond,in}) \quad (6.48)$$

$$Q_{cond} = \dot{m}_T(h_3 - h_4) \quad (6.49)$$

Where C_{min} is calculated with equation (6.45) with the refrigerant conditions at state 3 and the inlet condenser conditions. Temperature $T_{4'}$ has an assumed quality of 0 and can be retrieved by calling the CoolProp routine. The temperature at the inlet of the expansion valve, T_4 , can be calculated by subtracting the fixed subcool provided by the heat exchanger from $T_{4'}$:

$$T_4 = T_{4'} - \Delta T_{subcool} \quad (6.50)$$

Expansion Valve

The expansion valve is assumed to be isenthalpic. Therefore, for the main expansion valve, the enthalpy at the inlet of the evaporator is equal to the enthalpy at state 4:

$$h_6 = h_4 \quad (6.51)$$

General Equations

From the output of the python code (capacity and power of the heat pump), the model calculates the heat pump's outlet temperature:

$$T_{cond,out} = T_{cond,in} + \frac{Q_{cond}}{\dot{m}_{cond}C_{p,cond}} \quad (6.52)$$

The energy absorbed by the evaporator is calculated as follows:

$$Q_{evap} = Q_{cond} - W_{comp} \quad (6.53)$$

The COP of the heat pump is given as:

$$COP_h = \frac{Q_{cond}}{W_{comp}} \quad (6.54)$$

Solving Method

The thermodynamic model calculates the capacity and power based on the refrigerant cycle. The calculations are structured as follows:

1. The initial values are set (T_0 , T_1 , T_3 , P_1 , and P_2).
2. The evaporator capacity is calculated using equations (6.44) to (6.46). An error is calculated to compare the results from the two capacity equations.

3. The power is calculated using equations (6.33) to (6.43).
4. The condenser capacities are calculated using equations (6.48) to (6.50). An error for both capacities is calculated to compare the two methods of calculating the capacity.
5. The enthalpy leaving the main expansion valve (state 6) is calculated with Equation (6.51).
6. The temperature leaving the evaporator, T_1 , is recalculated using equation (6.47), and an error is calculated for the relative difference between T_1 and $T_{1,new}$.
7. Steps 2 to 8 are repeated until the errors calculated in steps 2, 4, and 8 are below 1%.

Water Tank Model

The immersed coils were modelled based on the methodology used for the tank model in TRNSYS. It models the flow through the heat exchanger pipes, calculating the pipe resistance, R_w , as well as the heat transfer coefficient for the inside and outside of the pipe, h_i and h_o , respectively. In order to calculate the overall heat transfer coefficient, $U_{coil}A_{coil}$. The outside heat transfer coefficient, as well as the resistance, can be calculated using the following equations:

$$R_w = \frac{\ln\left(\frac{r_o}{r_i}\right)}{2\pi L_{pipe}k} \quad (6.55)$$

$$Ra = \frac{g\beta}{\nu\alpha} (T_{coil,i} - T_2) d_{pipe,o}^3 \quad (6.56)$$

$$Nu_o = C \cdot Ra^n \cdot GF^m \quad (6.57)$$

$$h_o = \frac{Nu_o k_w}{d_{pipe,o}} \quad (6.58)$$

Where r_o and r_i are the outer and inner radii of the heat exchanger pipe in m. $d_{pipe,o}$ is the outer diameter of the pipe in m, L_{pipe} is the length of the pipe in m, k is the thermal conductance of the pipe in W/(m·K), g is the gravity in m/s², β is the thermal expansion coefficient assumed to be 0.00026 1/K, GF is the geometry factor and m is the geometry exponential both are assumed to be

1. C is the multiplier for natural convection (assumed to be 0.6) and n is the exponential of natural convection (assumed to be 0.25). Ra is the Rayleigh number, and finally, Nu_o is the Nusselt number on the outside of the heat exchanger coils.

The inner heat transfer coefficient can be calculated by first using calculating the critical Reynold's number, Re_{crit} , to determine when the flow is in the laminar or turbulent regions. Then calculating the fluid's Reynolds number, Re , as well as the Prandtl number, Pr , with the following equations:

$$Re_{crit} = 20000 \left(\frac{d_{pipe,i}}{d_{coil}} \right)^{0.32} \quad (6.59)$$

$$Re = \frac{4\dot{m}_{coil}}{\pi d_{pipe,i} \mu} \quad (6.60)$$

$$Pr = \frac{c_p \mu}{k_w} \quad (6.61)$$

Where $d_{pipe,i}$ is the inner diameter of the pipe in m, d_{coil} is the diameter of the coil in m, \dot{m}_{coil} is the mass flow rate flowing through the pipe in kg/h, and μ is the viscosity in Pa·h.

If the fluid is within the laminar region, the following equations will be used:

$$HE = \frac{Re \left(\frac{d_{pipe,i}}{d_{coil}} \right)^{0.5}}{1 + \left(\frac{pitch}{\pi d_{pipe,i}} \right)^2} \quad (6.62)$$

$$Nu = \left(\left(4.36 + \frac{4.64}{1 + \left(\frac{1342HE^2}{Pr} \right)^2} \right)^3 + 1.816 \left(\frac{HE}{1 + \frac{1.15}{Pr}} \right)^{1.5} \right)^{1/3} \quad (6.63)$$

If the fluid is within the turbulent region, the following equation will be used:

$$Nu = 0.0023Re^{0.85}Pr^{0.4} \left(\frac{d_{pipe,i}}{d_{coil}} \right)^{0.1} \quad (6.64)$$

Finally, the inner heat transfer coefficient and the overall coil heat transfer coefficient can be calculated using the following equations:

$$h_i = \frac{Nuk_w}{d_{pipe,i}} \quad (6.65)$$

$$U_{coil}A_{coil} = \frac{1}{\frac{1}{h_oA_{coil,o}} + R_w + \frac{1}{h_iA_{coil,i}}} \quad (6.66)$$

Utility Rates

Daytime Charging

Daytime charging is a strategy used particularly with storage systems as well as renewables as it requires storing thermal or electrical energy when a renewable source produces it. In the case of this analysis, the water tank will store thermal energy by increasing the water temperature setpoint only when the solar irradiation is above a threshold, 300 W/m² for this analysis. An example of this schedule can be seen in Figure C - 1.

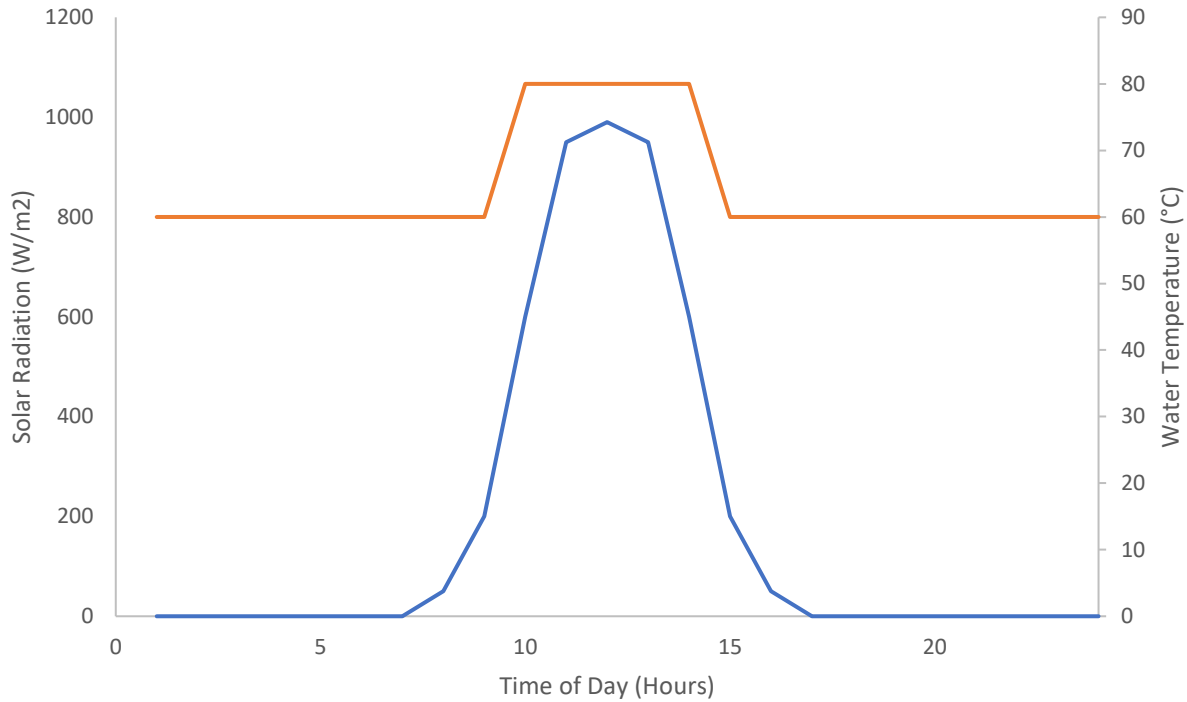


Figure C - 1: Daytime charging water temperature setpoint

Critical Peak Pricing

Critical peak pricing is a real-time pricing strategy that significantly increases the price per kWh during critical events. It occurs for a small number of hours per year and the timing of the peak periods is unknown ahead of time (Federal Energy Regulatory Commission, 2006). In order to simplify this scheduling, the critical event periods are at fixed intervals each day during the winter season. These events occur from 6:00 am to 10:00 am and 4:00 pm to 8:00 pm, as shown in Figure C - 2. The tank is charged 4 hours in advance of the events based on the assumption that the system will receive a 4-hour notice prior to any critical period.

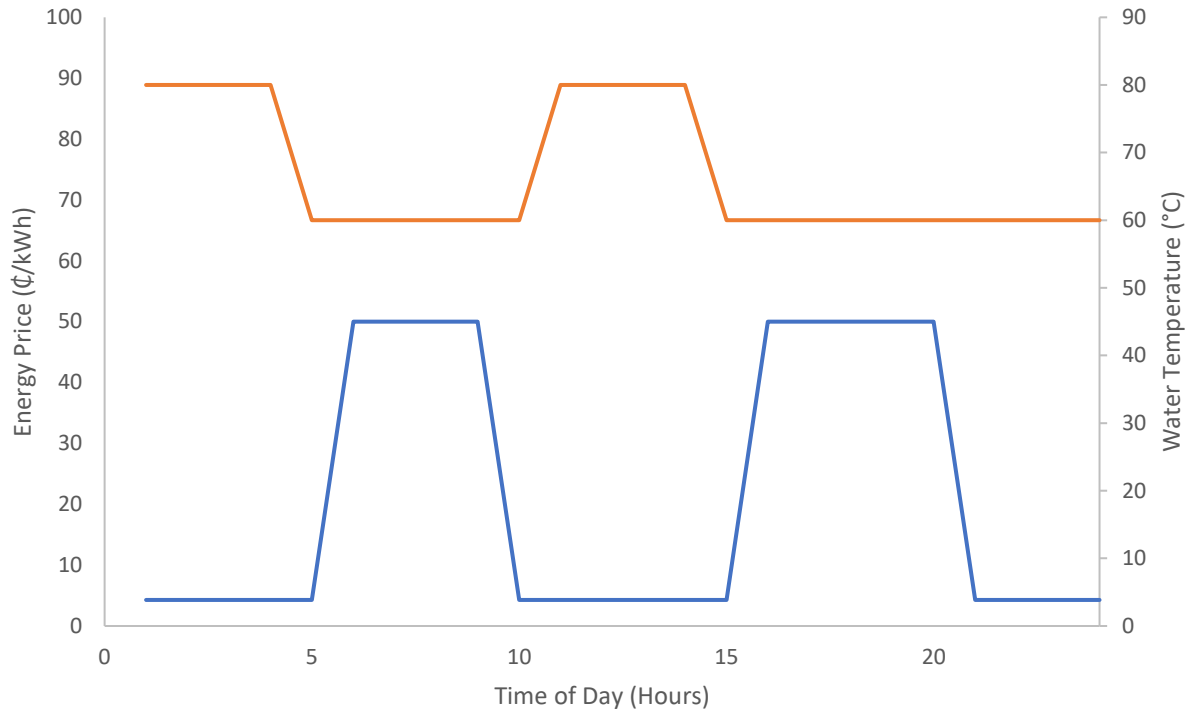


Figure C - 2: Critical event pricing water temperature setpoint

Time-of-Use

As Montreal does not use a Time-of-Use (TOU) pricing structure, the pricing was taken from Hydro Ontario using the pricing effective November 2019 (Ontario Energy Board, 2020). The TOU schedule can be seen in Figure C - 3.

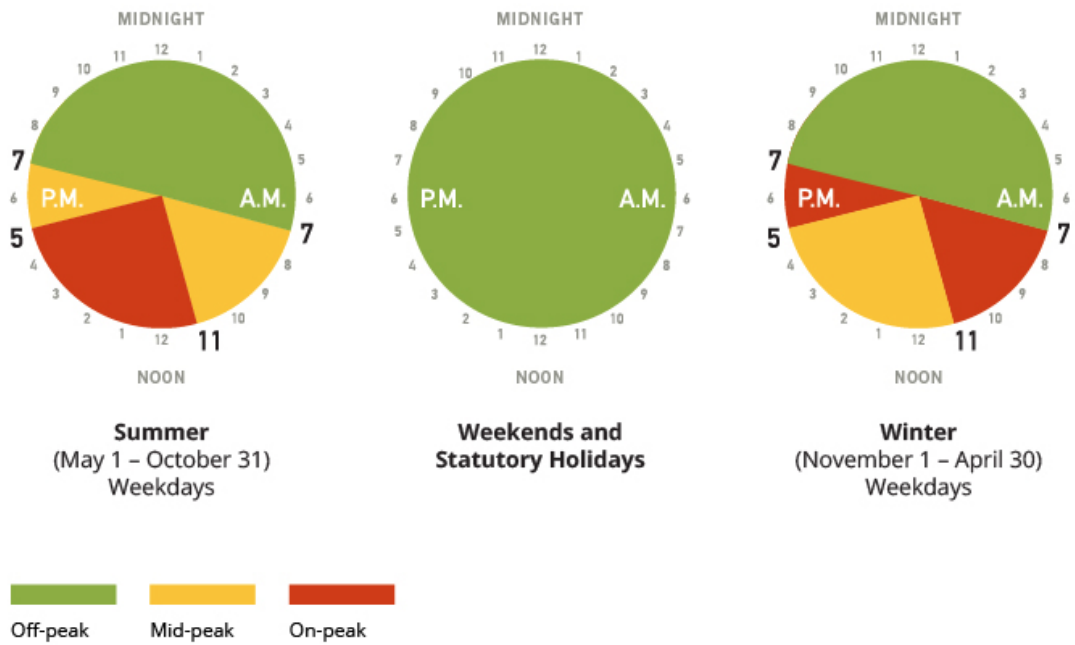


Figure C - 3: Time-of-Use pricing schedule (Ontario Energy Board, 2020)

Appendix D: Additional Experimental Results

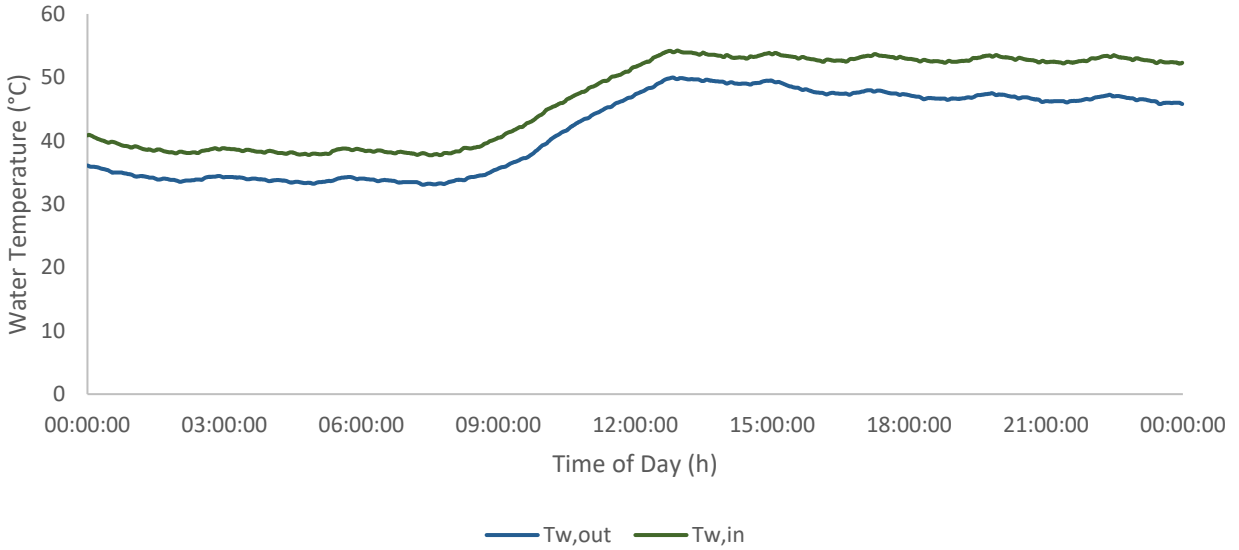


Figure D - 1: Water temperatures on December 14th, 2021 (sunny day)

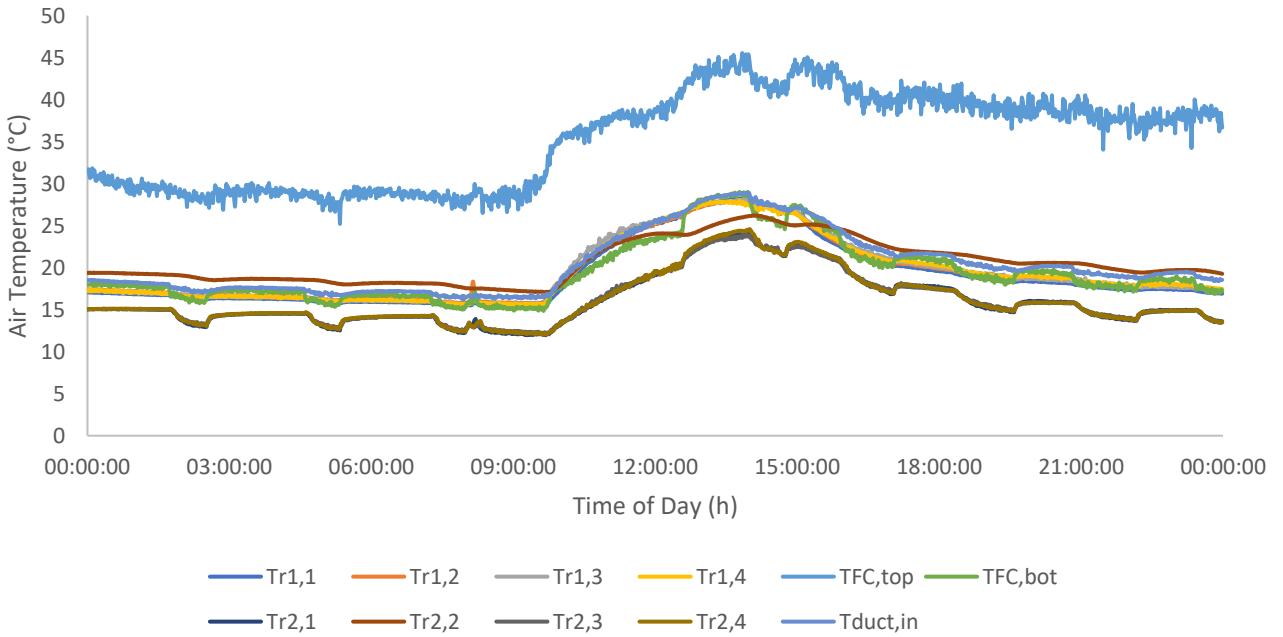


Figure D - 2: Room temperatures in test cells 3 and 4 on December 14th, 2021 (sunny day)

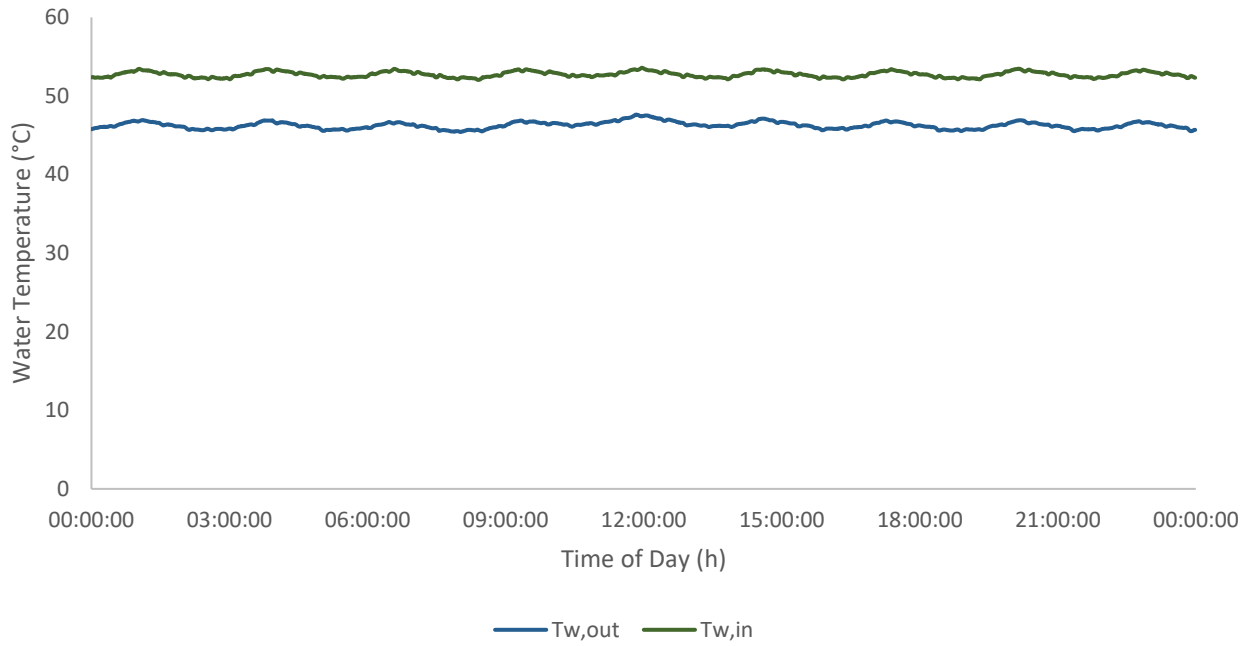


Figure D - 3: Water temperatures on December 15th, 2021 (cloudy day)

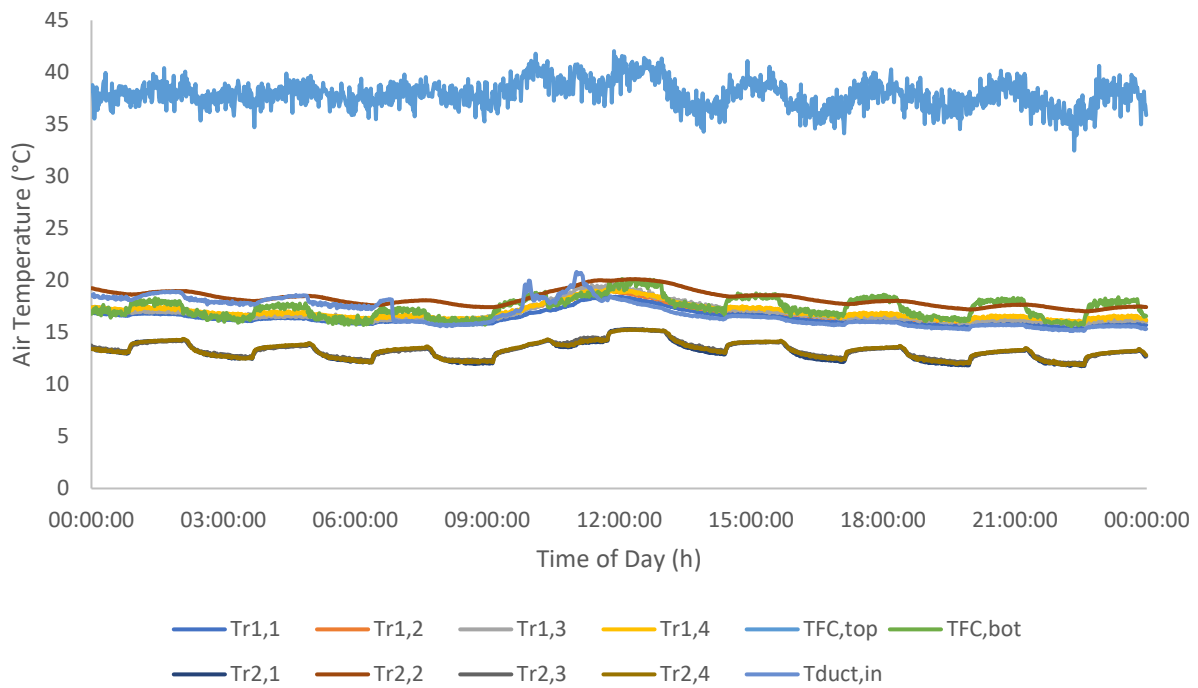


Figure D - 4: Air temperatures in test cells 3 and 4 on December 15th, 2021 (cloudy day)

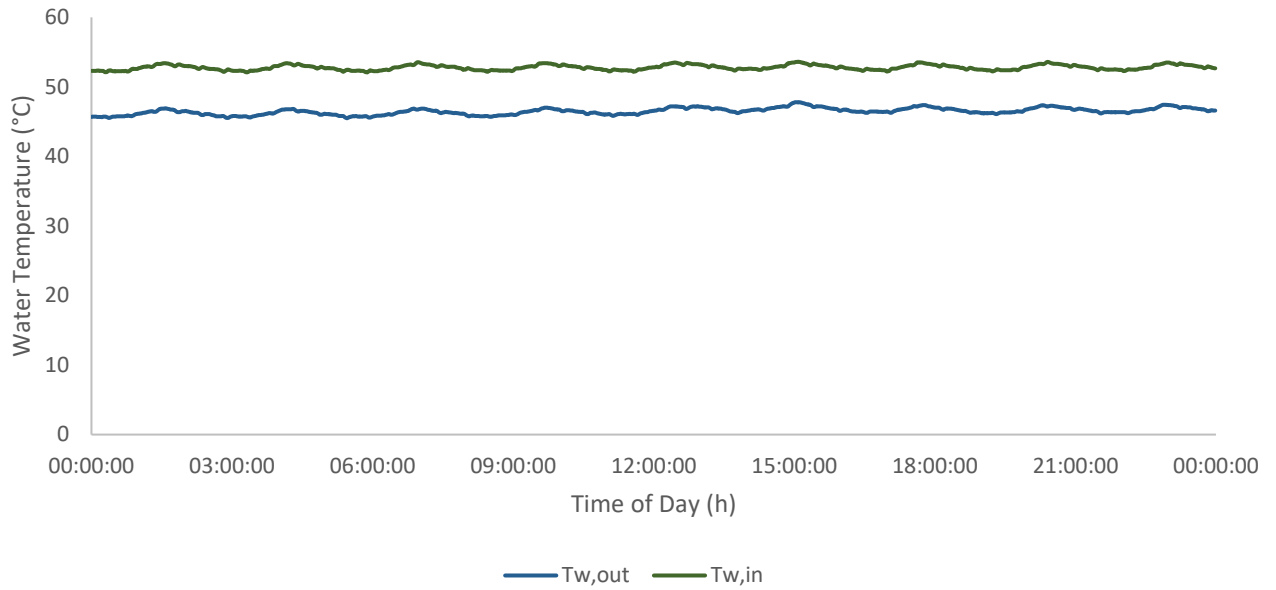


Figure D - 5: Water temperatures on December 16th, 2021 (cloudy day)

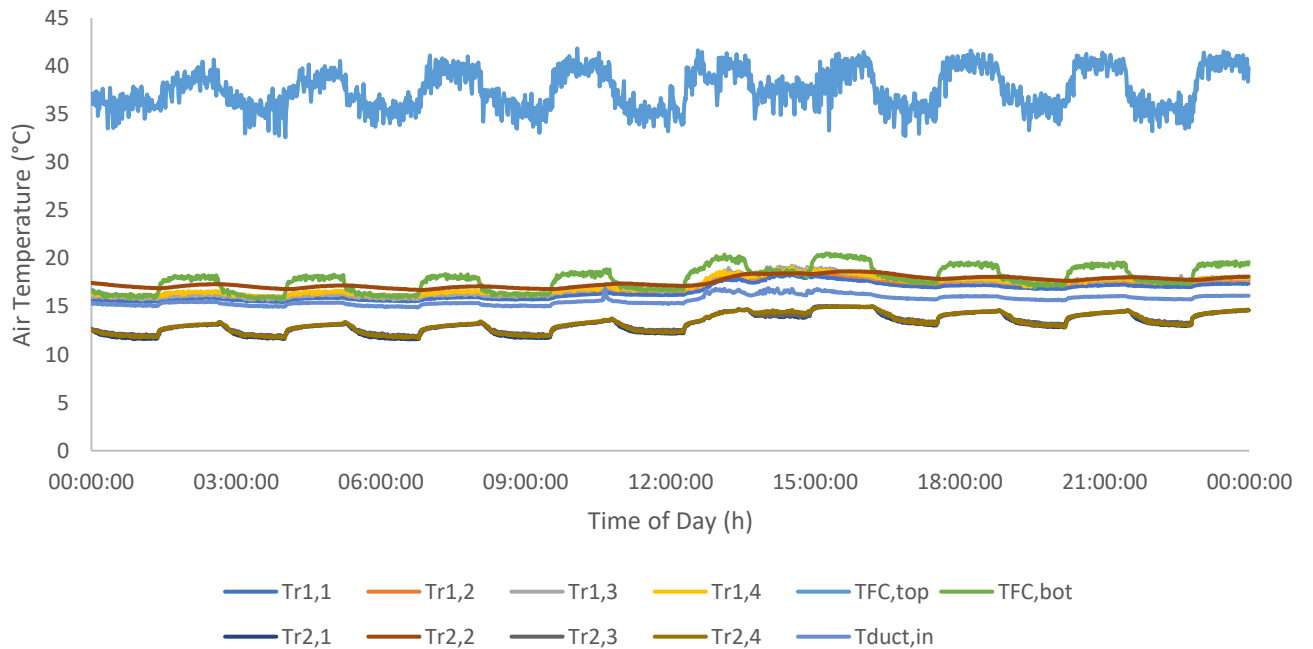


Figure D - 6: Air temperatures in test cells 3 and 4 on December 16th, 2021 (cloudy day)